Future Generation of Structural Health Monitoring: Innovations and Emerging Needs

Lead Guest Editor: Khaled Ghaedi
Guest Editors: Meisam Gordan and Ayman Ahmed Seleemah

Future Generation of Structural Health Monitoring: Innovations and Emerging Needs

Future Generation of Structural Health Monitoring: Innovations and Emerging Needs

Lead Guest Editor: Khaled Ghaedi
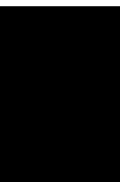Guest Editors: Meisam Gordan and Ayman Ahmed Seleemah

Zhaofei Chu , China
Wonseok Chung , Republic of Korea
Donato Ciampa , Italy
Gian Paolo Cimellaro, Italy
Francesco Colangelo, Italy
Romulus Costache , Romania
Liviu-Adrian Cotfas , Romania
Antonio Maria D'Altri, Italy
Bruno Dal Lago , Italy
Amos Darko , Hong Kong
Arka Jyoti Das , India
Dario De Domenico , Italy
Gianmarco De Felice , Italy
Stefano De Miranda , Italy
Maria T. De Risi , Italy
Tayfun Dede, Turkey
Sadik O. Degertekin , Turkey
Camelia Delcea , Romania
Cristoforo Demartino, China
Giuseppe Di Filippo , Italy
Luigi Di Sarno, Italy
Fabio Di Trapani , Italy
Aboelkasim Diab , Egypt
Thi My Dung Do, Vietnam
Giulio Dondi , Italy
Jiangfeng Dong , China
Chao Dou , China
Mario D'Aniello , Italy
Jingtao Du , China
Ahmed Elghazouli, United Kingdom
Francesco Fabbrocino , Italy
Flora Faleschini , Italy
Dingqiang Fan, Hong Kong
Xueping Fan, China
Qian Fang , China
Salar Farahmand-Tabar , Iran
Ilenia Farina, Italy
Roberto Fedele, Italy
Guang-Liang Feng , China
Luigi Fenu , Italy
Tiago Ferreira , Portugal
Marco Filippo Ferrotto, Italy
Antonio Formisano , Italy
Guoyang Fu, Australia
Stefano Galassi , Italy

Junfeng Gao , China
Meng Gao , China
Giovanni Garcea , Italy
Enrique García-Macías, Spain
Emilio García-Taengua , United Kingdom
DongDong Ge , USA
Khaled Ghaedi, Malaysia
Khaled Ghaedi , Malaysia
Gian Felice Giaccu, Italy
Agathoklis Giaralis , United Kingdom
Ravindran Gobinath, India
Rodrigo Gonçalves, Portugal
Peilin Gong , China
Belén González-Fonteboa , Spain
Salvatore Grasso , Italy
Fan Gu, USA
Erhan Güneyisi , Turkey
Esra Mete Güneyisi, Turkey
Pingye Guo , China
Ankit Gupta , India
Federico Gusella , Italy
Kemal Hacıefendioğlu, Turkey
Jianyong Han , China
Song Han , China
Asad Hanif , Macau
Hadi Hasanzadehshooiili , Canada
Mostafa Fahmi Hassanein, Egypt
Amir Ahmad Hedayat , Iran
Khandaker Hossain , Canada
Zahid Hossain , USA
Chao Hou, China
Biao Hu, China
Jiang Hu , China
Xiaodong Hu, China
Lei Huang , China
Cun Hui , China
Bon-Gang Hwang, Singapore
Jijo James , India
Abbas Fadhil Jasim , Iraq
Ahad Javanmardi , China
Krishnan Prabhakan Jaya, India
Dong-Sheng Jeng , Australia
Han-Yong Jeon, Republic of Korea
Pengjiao Jia, China
Shaohua Jiang , China

MOUSTAFA KASSEM, Malaysia
Mosbeh Kaloop, Egypt
Shankar Karuppannan, Ethiopia
John Kechagias, Greece
Mohammad Khajehzadeh, Iran
Afzal Husain Khan, Saudi Arabia
Mehran Khan, Hong Kong
Manoj Khandelwal, Australia
Jin Kook Kim, Republic of Korea
Woosuk Kim, Republic of Korea
Vaclav Koci, Czech Republic
Loke Kok Foong, Vietnam
Hailing Kong, China
Leonidas Alexandros Kouris, Greece
Kyriakos Kourousis, Ireland
Moacir Kripka, Brazil
Anupam Kumar, The Netherlands
Emma La Malfa Ribolla, Czech Republic
Ali Lakirouhani, Iran
Angus C. C. Lam, China
Thanh Quang Khai Lam, Vietnam
Luciano Lamberti, Italy
Andreas Lampropoulos, United Kingdom
Raffaele Landolfo, Italy
Massimo Latour, Italy
Bang Yeon Lee, Republic of Korea
Eul-Bum Lee, Republic of Korea
Zhen Lei, Canada
Leonardo Leonetti, Italy
Chun-Qing Li, Australia
Dongsheng Li, China
Gen Li, China
Jiale Li, China
Minghui Li, China
Qingchao Li, China
Shuang Yang Li, China
Sunwei Li, Hong Kong
Yajun Li, China
Shun Liang, China
Francesco Liguori, Italy
Jae-Han Lim, Republic of Korea
Jia-Rui Lin, China
Kun Lin, China
Shibin Lin, China

Tzu-Kang Lin, Taiwan
Yu-Cheng Lin, Taiwan
Hexu Liu, USA
Jian Lin Liu, China
Xiaoli Liu, China
Xuemei Liu, Australia
Zaobao Liu, China
Zhuang-Zhuang Liu, China
Diego Lopez-Garcia, Chile
Cristiano Loss, Canada
Lyan-Ywan Lu, Taiwan
Jin Luo, USA
Yanbin Luo, China
Jianjun Ma, China
Junwei Ma, China
Tian-Shou Ma, China
Zhongguo John Ma, USA
Maria Macchiaroli, Italy
Domenico Magisano, Italy
Reza Mahinroosta , Australia
Yann Malecot, France
Prabhat Kumar Mandal, India
John Mander, USA
Iman Mansouri, Iran
André Dias Martins, Portugal
Domagoj Matesan, Croatia
Jose Matos, Portugal
Vasant Matsagar, India
Claudio Mazzotti, Italy
Ahmed Mebarki, France
Gang Mei, China
Kasim Mermerdas, Turkey
Giovanni Minafò, Italy
Masoomeh Mirrashid, Iran
Abbas Mohajerani, Australia
Fadzli Mohamed Nazri, Malaysia
Fabrizio Mollaioli, Italy
Rosario Montuori, Italy
H. Naderpour, Iran
Hassan Nasir, Pakistan
Hossein Nassiraei, Iran
Satheeskumar Navaratnam, Australia
Ignacio J. Navarro, Spain
Ashish Kumar Nayak, India
Behzad Nematollahi, Australia

Chayut Ngamkhanong (iD), Thailand
Trung Ngo, Australia
Tengfei Nian, China
Mehdi Nikoo (iD), Canada
Youjun Ning (iD), China
Olugbenga Timo Oladinrin (iD), United Kingdom
Oladimeji Benedict Olalusi, South Africa
Timothy O. Olawumi (iD), Hong Kong
Alejandro Orfila (iD), Spain
Maurizio Orlando (iD), Italy
Siti Aminah Osman, Malaysia
Walid Oueslati (iD), Tunisia
SUVASH PAUL (iD), Bangladesh
John-Paris Pantouvakis (iD), Greece
Fabrizio Paolacci (iD), Italy
Giuseppina Pappalardo (iD), Italy
Fulvio Parisi (iD), Italy
Dimitrios G. Pavlou (iD), Norway
Daniele Pellegrini (iD), Italy
Gatheeshgar Perampalam (iD), United Kingdom
Daniele Perrone (iD), Italy
Giuseppe Piccardo (iD), Italy
Vagelis Plevris (iD), Qatar
Andrea Pranno (iD), Italy
Adolfo Preciado (iD), Mexico
Chongchong Qi (iD), China
Yu Qian, USA
Ying Qin (iD), China
Giuseppe Quaranta (iD), Italy
Krishanu ROY (iD), New Zealand
Vlastimir Radonjanin, Serbia
Carlo Rainieri (iD), Italy
Rahul V. Ralegaonkar, India
Raizal Saifulnaz Muhammad Rashid, Malaysia
Alessandro Rasulo (iD), Italy
Chonghong Ren (iD), China
Qing-Xin Ren, China
Dimitris Rizos (iD), USA
Geoffrey W. Rodgers (iD), New Zealand
Pier Paolo Rossi, Italy
Nicola Ruggieri (iD), Italy
JUNLONG SHANG, Singapore

Nikhil Saboo, India
Anna Saetta, Italy
Juan Sagaseta (iD), United Kingdom
Timo Saksala, Finland
Mostafa Salari, Canada
Ginevra Salerno (iD), Italy
Evangelos J. Sapountzakis (iD), Greece
Vassilis Sarhosis (iD), United Kingdom
Navaratnarajah Sathiparan (iD), Sri Lanka
Fabrizio Scozzese (iD), Italy
Halil Sezen (iD), USA
Payam Shafigh (iD), Malaysia
M. Shahria Alam, Canada
Yi Shan, China
Hussein Sharaf, Iraq
Mostafa Sharifzadeh, Australia
Sanjay Kumar Shukla, Australia
Amir Si Larbi (iD), France
Okan Sirin (iD), Qatar
Piotr Smarzewski (iD), Poland
Francesca Sollecito (iD), Italy
Rui Song (iD), China
Tian-Yi Song, Australia
Flavio Stochino (iD), Italy
Mayank Sukhija (iD), USA
Piti Sukontasukkul (iD), Thailand
Jianping Sun, Singapore
Xiao Sun (iD), China
T. Tafsirojjaman (iD), Australia
Fujiao Tang (iD), China
Patrick W.C. Tang (iD), Australia
Zhi Cheng Tang (iD), China
Weerachart Tangchirapat (iD), Thailand
Xiaxin Tao, China
Piergiorgio Tataranni (iD), Italy
Elisabete Teixeira (iD), Portugal
Jorge Iván Tobón (iD), Colombia
Jing-Zhong Tong, China
Francesco Trentadue (iD), Italy
Antonello Troncone, Italy
Majbah Uddin (iD), USA
Tariq Umar (iD), United Kingdom
Muahmmad Usman, United Kingdom
Muhammad Usman (iD), Pakistan
Mucteba Uysal (iD), Turkey

Ilaria Venanzi, Italy

Castorina S. Vieira, Portugal

Valeria Vignali, Italy

Claudia Vitone, Italy

Liwei WEN, China

Chunfeng Wan, China

Hua-Ping Wan, China

Roman Wan-Wendner, Austria

Chaohui Wang, China

Hao Wang, USA

Shiming Wang, China

Wayne Yu Wang, United Kingdom

Wen-Da Wang, China

Xing Wang, China

Xiuling Wang, China

Zhenjun Wang, China

Xin-Jiang Wei, China

Tao Wen, China

Weiping Wen, China

Lei Weng, China

Chao Wu, United Kingdom

Jiangyu Wu, China

Wangjie Wu, China

Wenbing Wu, China

Zhixing Xiao, China

Gang Xu, China

Jian Xu, China

Panpan, China

Rongchao Xu, China

HE YONGLIANG, China

Michael Yam, Hong Kong

Hailu Yang, China

Xu-Xu Yang, China

Hui Yao, China

Xinyu Ye, China

Zhoujing Ye , China

Gürol Yildirim, Turkey

Dawei Yin, China

Doo-Yeol Yoo, Republic of Korea

Zhanping You, USA

Afshar A. Yousefi, Iran

Xinbao Yu, USA

Dongdong Yuan, China

Geun Y. Yun, Republic of Korea

Hyun-Do Yun, Republic of Korea

Cemal YİĞİT, Turkey

Paolo Zampieri, Italy

Giulio Zani, Italy

Mariano Angelo Zanini, Italy

Zhixiong Zeng, Hong Kong

Mustafa Zeybek, Turkey

Henglong Zhang, China

Jiupeng Zhang, China

Tingting Zhang, China

Zengping Zhang, China

Zetian Zhang, China

Zhigang Zhang, China

Zhipeng Zhao, Japan

Jun Zhao, China

Annan Zhou, Australia

Jia-wen Zhou, China

Hai-Tao Zhu, China

Peng Zhu, China

QuanJie Zhu, China

Wenjun Zhu, China

Marco Zucca, Italy

Haoran Zuo, Australia

Junqing Zuo, China

Robert Černý, Czech Republic

Süleyman İpek, Turkey

Contents

Research Article

A Damage Detection Approach in the Era of Industry 4.0 Using the Relationship between Circular Economy, Data Mining, and Artificial Intelligence

Meisam Gordan [iD],[1,2] **Saeed-Reza Sabbagh-Yazdi** [iD],[3] **Khaled Ghaedi** [iD],[2] **and Zubaidah Ismail** [iD][4]

[1]*School of Civil Engineering, University College Dublin, Belfield, D04 V1W8 Dublin, Ireland*
[2]*Research and Development Centre, PASOFAL Engineering Group, Kuala Lumpur, Malaysia*
[3]*Department of Civil Engineering, KNTOOSI University of Technology, Tehran, Iran*
[4]*Department of Civil Engineering, University of Malaya, 50603 Kuala Lumpur, Malaysia*

Correspondence should be addressed to Meisam Gordan; meisam.gordan@ucd.ie

Over the last decades, the emergence of new technologies has inspired a paradigm shift for the fourth industrial revolution. For example, circular economy, data mining, and artificial intelligence (AI), which are multidisciplinary topics, have recently attracted industrial and academic interests. Sustainable structural health monitoring (SHM) also concerns the continuous structural assessment of civil, mechanical, aerospace, and industrial structures to upgrade conventional SHM systems. A damage detection approach inspired by the principles of data mining with the adoption of circular-economic thinking is proposed in this study. In addition, vibration characteristics of a composite bridge deck structure are employed as inputs of AI algorithms. Likewise, an artificial neural network (ANN) integrated with a genetic algorithm (GA) was also developed for detecting the damage. GA was applied to define the initial weights of the neural network. To aid the aim, a range of damage scenarios was generated and the achieved outcomes confirm the feasibility of the developed method in the fault diagnosis procedure. Several data mining techniques were also employed to compare the performance of the developed model. It is concluded that the ANN integrated with GA presents a relatively fitting capacity in the detection of damage severity.

1. Introduction

Advanced, large, and expensive engineering assets such as high-rise buildings, long-span bridges, dams, oil platforms, hydraulic structures, wind turbines, offshore structures, railways, and ports were designed to last long [1–7]. However, many of them were more than halfway through their intended service life, and some of them have already reached the end of it [8]. Countries spend billions each year on the maintenance of these assets. For instance, according to ASCE 2021 infrastructure report card [9], there were more than 617,000 bridges across the United States. Currently, 42% of all bridges are at least 50 years old and 46,154 of the bridges are considered structurally deficient, meaning they

are in "poor" condition and in need of repair that requires a $125 billion investment. In another example, road and rail infrastructures across Europe have been degrading because of too little maintenance due to the global economic crisis [10]. Therefore, the monitoring costs associated with the aging engineering assets have become an ongoing concern. Emerging technologies need to overcome such bottlenecks to act more cost-effectively and sustainably in the planning, control, and management of structures. Structural health monitoring (SHM) as a powerful tool was utilized to address the above concerns by changing timetabled maintenance with as-needed repairs [11].

SHM is the process of applying a damage detection approach to evaluate the health condition of mechanical,

civil, and aerospace engineering assets [12]. Damage detection techniques can be considered in two categories due to their detection abilities which include local-based and global-based techniques [13]. Conventional approaches, e.g., visual inspections, ultrasonic, acoustic emissions, and radiography, are local-based damage detection methods with various drawbacks. For instance, the aforesaid costly techniques normally necessitate prior knowledge of the damage location which makes them laborious and inefficient, especially in big and complicated structures [14, 15]. In contrast, global-based methods, e.g., vibration-based techniques are based on global structural response and they have been developed to overcome the aforementioned drawbacks [16, 17]. From another perspective, emerging computer-based technologies require to be operated for achieving SHM data [18]. Hence, mathematical evolutions have upgraded the SHM schemes. For example, data mining methods [19, 20], cloud computing [21], and deep learning [22] have recently been employed in SHM. AI is also one of the developing scientific strategies in the 2020s [23, 24]. Over the past decade, ANN has provided broad solutions for structural system identification problems [25]. Moreover, according to [26], these days a lot of evolutionary techniques exist, e.g., GA [27], ant colony optimization [28], grey wolf optimization [29], particle swarm optimization [30], artificial immune algorithm [31], artificial bee colony algorithm [32], and firefly algorithm [33]. Among all metaheuristic techniques, the GA holds the highest standard aimed at resolving global optimization problems [34, 35].

The fourth industrial revolution, which is known as Industry 4.0, IR 4.0, or 4IR, includes various platforms, e.g., data mining, AI, and circular economy. Data mining has also several models to run [36–43]. Cross-industry standard process for data mining (CRISP-DM) is the most widespread paradigm [44]. This model has a hierarchical and cyclic process in six stages, i.e., business understanding, data understanding, data preparation, modeling, evaluation, and deployment. In the modeling phase of CRISP-DM, three types of techniques such as statistical, machine learning, and AI techniques can be used for different applications [45, 46]. Likewise, the circular economy has several frameworks [47, 48]. According to [49], the most comprehensive circular economy framework in six stages was proposed by Potting et al. [50]. Data mining and AI are considered as one of the main factors for an extensive adoption and enhanced modification to the circular economy.

Based on the literature review, it is felt to improve the smartification of global-based structural damage identification systems using Industry 4.0 technologies due to the demanding needs of developing the fault diagnosis of structures. Therefore, by taking advantage of the described relationship between circular economy, data mining, and AI, a generalized fault diagnosis workflow is proposed in this study. This is also associated with the fact that for the implementation of computational techniques in SHM, a systematic procedure along with relevant algorithms is essential. Consequently, in this article, a brief background of Industry 4.0, circular economy, and data mining are highlighted in Section 2. The architecture of the proposed circular model is presented in Section 3. Experimental modal analysis of a composite bridge deck structure is also detailed in this section. Here, a range of damage scenarios is introduced to generate the vibration characteristics of single-type and multiple-type damage cases as the input database for training the developed ANN integrated with the GA pattern. In Section 4, finite element modeling of the test structure is carried out to verify the experimental work. The outcomes of the introduced hybrid network are also presented in this section. Then, the performance of the pattern is compared with predeveloped ANN, support vector machine (SVM), and classification and regression trees (CART) using mean absolute error (MAE). Finally, Section 5 highlights the conclusions.

2. Fourth Industrial Revolution (Industry 4.0)

The term "industry" refers to the creation of products, services, and facilities within an economy. Our world has experienced four steps of industrialization. Table 1 presents the most important contributions of the fourth industrial revolution, adopted from [51–57]. Circular economy, data mining, and AI aligned with the fourth industrial revolution (Industry 4.0) promote smart tasks and diagnostics in research and analytics to industries and organizations in predictive policing. Data mining and AI platforms are also considered as one of the main factors for an extensive adoption and enhanced modification to the circular economy [58, 59].

The linear economy operates as if there are infinite resources in the world. In the same line, linear thinking as a traditional value chain has been started after the third industrial revolution [60]. A linear economy is based on a "Take, Make, and Dispose" model [61]. In the beginning, the implementation of this model was successful. However, it misused the resources in an unsustainable way. For example, the United Nations has estimated that by 2030, the world will need to double the existing resources to become equal with the rate of global production, consumption, and population growth [62]. Therefore, to become more sustainable, it is required to move to a circular system that is based on a closed-loop "Make, Use, and Return" model [63, 64]. In other words, the idea of a circular economy has been established from different aspects, i.e., finite resource stabilization, cost efficiency, pollution reduction, risk management, adoption of better retrofit practices, sharing economy, reusability, and recyclability of materials [65]. Therefore, this technology-focused system can be defined as a condition for sustainability. This is due to the fact that its concept moves towards the final aim of sustainability [66, 67].

With the rapid growth of database technology, more data were collected. Obviously, there is a lot of hidden important information behind the collected data. In this context, one of the popular strategies for knowledge discovery is the typical data processing approach. However, its assumption is difficult to converge with the actual work [68]. In addition, whenever there is a huge data collected, further drawbacks can appear. As a result, conventional strategies, i.e., classical

TABLE 1: Industry 4.0 contributions.

Key contributions of IR 4.0	(i) Internet of things (IoT) (ii) Smart factories/smart manufacturing/robotics (iii) Circular economy/product-lifecycle-management (PLM) (iv) Data mining/big data analytics/deep learning (v) AI/machine learning (vi) Smart sensors/remote sensing/wireless sensor network/online monitoring (vii) Cloud computing/cognitive computing/mobile computing (viii) Cybersecurity/blockchain (x) Digital twin/smart tasks and diagnostics/smartification (xi) Virtual reality/augmented reality/building information modeling (BIM) (xii) Unmanned aerial vehicles (UAVs)/internet of drone/smart cities (xiii) Smart environment/sustainable development/renewable energy

mathematical techniques perform rather inefficiently. Therefore, the analysis of information should be performed at a better level to better make use of the databases [69]. To overcome the mentioned drawbacks, sophisticated computing tools such as data mining can play a significant role in the extraction of valuable information from different databases [70, 71]. Data mining is an emerging procedure that is used to obtain knowledge from raw data. In fact, it can handle the qualitative analysis of complex and time-consuming real-world problems that cannot be solved with typical statistical techniques [72].

3. Methodology

By taking advantage of the described relationship between circular economy, data mining, and AI, a generalized fault diagnosis workflow is proposed in this study, as shown in Figure 1. This systematic model is based on the combination of CRISP-DM and circular economy closed-loop concepts for the health monitoring of engineering assets using inverse analysis. As can be observed from Figure 1, assessing the damage level is the initial part of the circular fault diagnosis model to collect data. The subsequent phase is focusing on data processing through a number of duties, i.e., data cleaning, data integration, data construction, and data transformation. Generally speaking, the data preparation step is one of the most problematic parts of the procedure. It is because several problems such as incomplete data, missing values, out-of-range records, wrong data type, and unavailable details should be solved in this step to construct a database. Then, the processed data are considered as inputs for the next step. In the modeling step, applicable algorithms such as ANN, fuzzy, support vector machine (SVM), principle component analysis (PCA), GA, ant colony optimization (ACO), Bayesian, and particle swarm optimization (PSO) can be applied for different purposes, i.e., classification, optimization, or perdition. The accomplished results are utilized for damage assessment of structural elements. Once the models are assessed, the deployment of the proposed circular model can be performed through the implementation of strengthening and retrofitting actions to expand the health state of structures. In this regard, the reliability of structures can be also estimated through

a number of suggested treatments, e.g., repairing or upgrading the structural members, major/minor maintenance, or replacement of the damaged components, as indicated in Figure 1.

3.1. Experimental Modal Analysis. Modal parameter estimation relies on methods of excitation as well as the accuracy of data acquisition tools. Mode identification methods can be divided into operational and experimental modal analysis. Operational modal analysis regularly refers to output-only measurements whereas experimental modal analysis uses input excitation and output response measurements to estimate the modal parameters [73–76]. In this study, a series of experimental modal analysis of a bridge deck structure were conducted to generate the data. The common span length, as well as girder spacing of a common composite girder bridge, is 25 m to 30 m and 3.5 m to 4 m, respectively. A 1 : 10-scaled form of this girder deck was cast and tested in the heavy structure laboratory of the Department of Civil Engineering, University of Malaya. The model consists of three universal steel beams joined to a concrete slab using shear stud connectors (see Figure 2). The length of the tested model is 3200 mm including 100 mm at both support ends. The materials used in this work were cement, fine aggregates, silica fume, water, and superplasticizer. The reinforcement of the concrete slab is welded wire mesh. Its diameter is 5 mm with 100 mm by 100 mm spacing. The concrete cover for the mesh is 30 mm. According to [77], mechanical connectors (e.g., shear studs) are needed to succeed the composite action. Therefore, full composite action between the concrete slab and steel I-beams is modeled using sixteen shear stud connectors which are installed on each I-beam. To do so, the nuts are welded on top of the beam flange. Then, the bolts are firmly tightened to the nuts. The schematic view, physical preparation, and experimental setup of the specimen are presented in Figures 2 and 3.

Figure 4 presents the schematic illustration of the conducted experimental modal analysis. In the first step, the composite bridge deck structure was tested in its intact condition to obtain the vibration features of the model as the reference or benchmark model. To aid the aim, the specimen
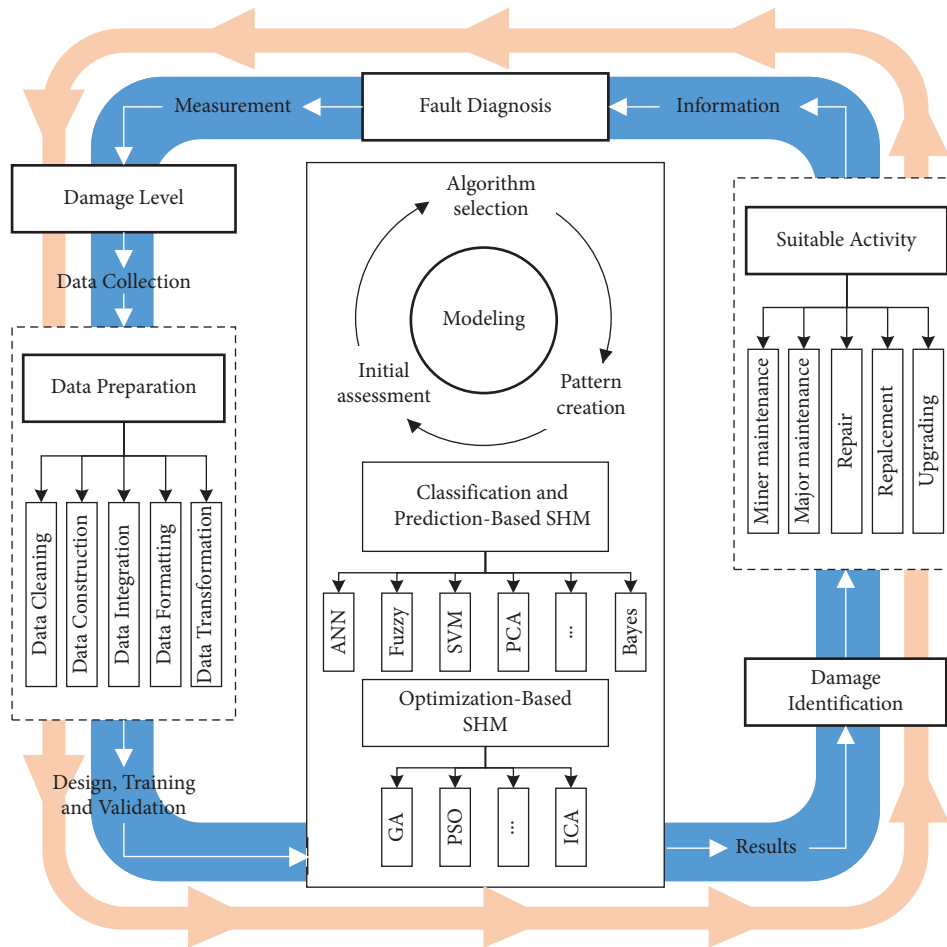
FIGURE 1: The proposed closed-loop model inspired by circular economy.

was excited using analogue signals of Wilcoxon accelerometers with the sensitivity of 100 mV/g through IMV VE-50 electrodynamic shaker which were amplified by VA-ST-03 power amplifier. Sixteen accelerometers were employed in each beam to record the time-domain responses of the model. OROS analyzer along with its platform, NVGate, recorded the measurements [78]. This signal analyzer transformed the input analogue signals to digital format with the sampling rate of 5.12 kS/s and the frequency bandwidth and resolution of 2500 Hz and 0.39 Hz, respectively. To do so, NVGate converted the time-domain data to the frequency domain utilizing fast Fourier transform. In the next step, the academic license of ICATS, which is the modal analyzer software, was used to extract the structural dynamic parameters, i.e., the first four flexural modes from measured modal test data [79].

Several damage cases (i.e., single and multiple) were induced to the test specimen through notching different locations in several members by saw cuts as well as a disk grinder. To aid the aim, twenty-five magnitudes of controlled damage from 3 mm to 75 mm depth with the increment of 3 mm and correspondingly the prescribed locations were generated for each damage case, as shown in Figure 5. The modal testing was carried out for each case, individually. As it can be seen from Figures 5(b) and 5(c), the mid-span of

beam 1 was considered as the location of damage for a single-type damage scenario, though the one-quarter span of beam 1 and three-quarter span of beam 3 were selected as damage location for the multiple-type damage scenario. It should be noted that in this study, different parts of the undamaged structure were incised to generate the damaged state. Then, the loss of stiffness was recovered by welding back the members to create another undamaged state. In this regard, the process of controlled cutting and welding was repeated in different damage scenarios. Then, the findings of the experimental modal analysis were employed in the role of inputs for the circular data mining-based process.

Vibration characteristics of the first four flexural modes, i.e., F_i, $i = 1, 2, 3, 4$ in healthy and damaged cases for single- and multiple-type scenarios were obtained, as shown in Figure 6. The horizontal axis of each figure signifies the twenty-six damage cases including the intact state in addition to twenty-five damaged states. The vertical axis of each figure indicates the natural frequency measurements. As it can be seen from the figure, in general, the trend of modal parameters in both scenarios reduced with damage expansions. However, several damaged states experienced slight fluctuations in particular modes. For example, the maximum reductions of natural frequency values were 3.71% in F_2-multiple damage state, 3.68% in F_3-single

(a)

(b)

(c)

(d)

(e)

(f)

(g)
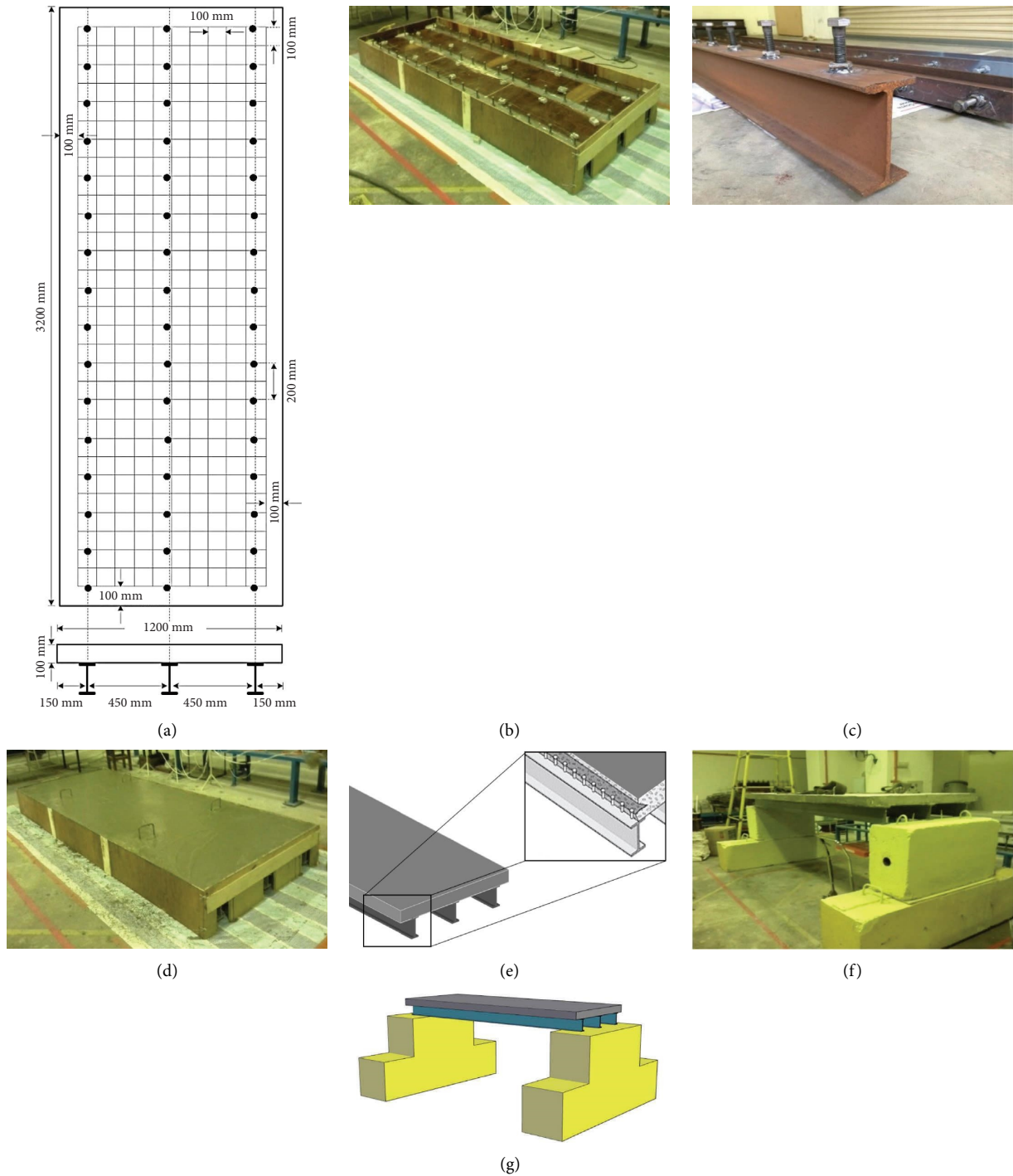
FIGURE 2: (a) Layout plan and dimensions, (b) construction of the specimen, (c) shear stud connectors, (d) casted model, (e) schematic view, (f) laboratory test setup, and (g) schematic setup of the specimen.

damage state, and 4.16% in F_3-multiple damage state. Conversely, the minimum reductions of natural frequencies belonged to mode 4 with 1.17% and 0.95% in single and multiple damage states, respectively. This is due to the node points aimed at certain mode shapes (see Figure 7). In addition, the results indicated that minor fluctuations of the natural frequencies affected by environmental uncertainties and noise were detected in some damage states, e.g., 36 mm damage state in modes 2 and 4 of single- and multiple-damage scenarios.
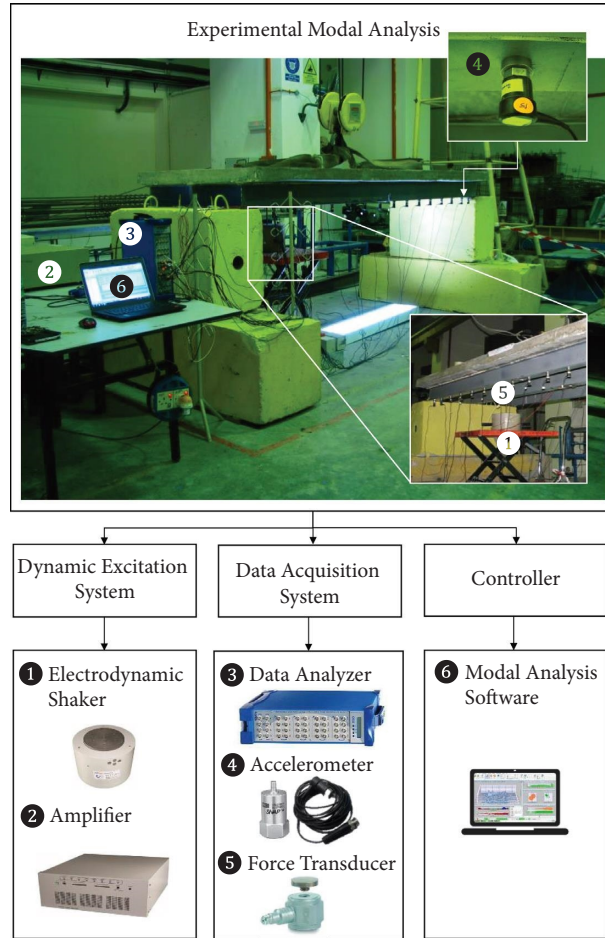
FIGURE 3: Experiment setup of the tested structure.
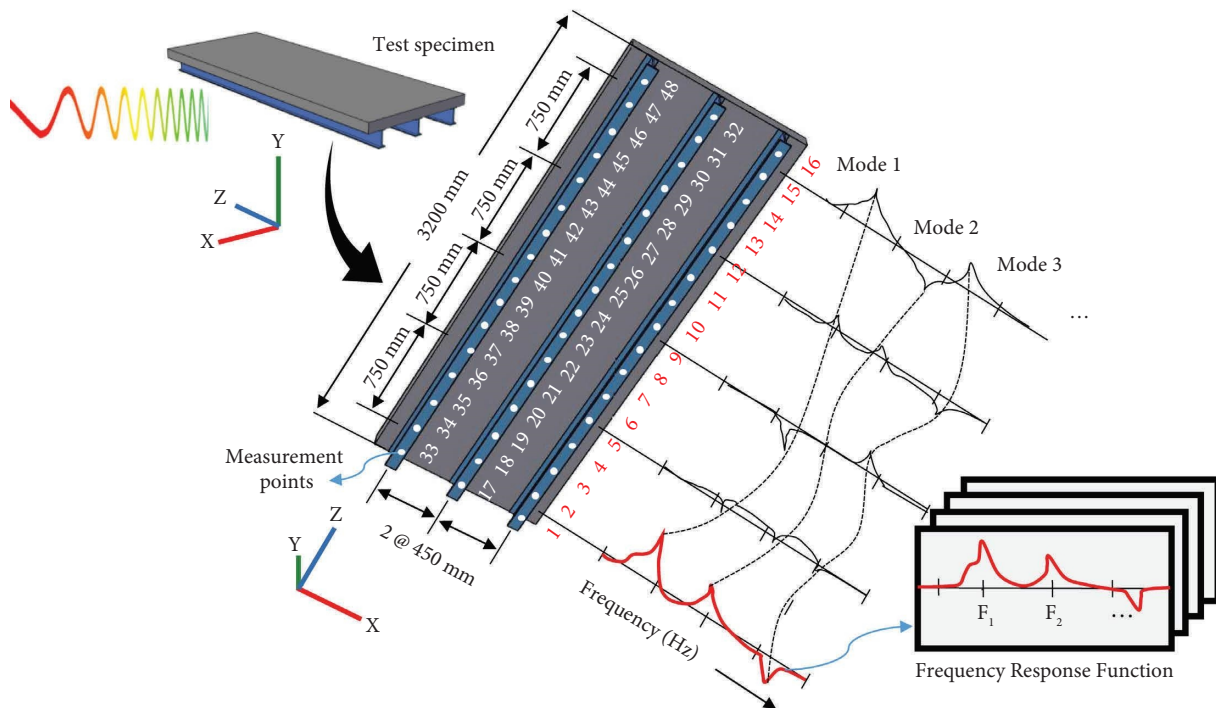
FIGURE 4: Schematic illustration of the conducted experimental modal analysis.
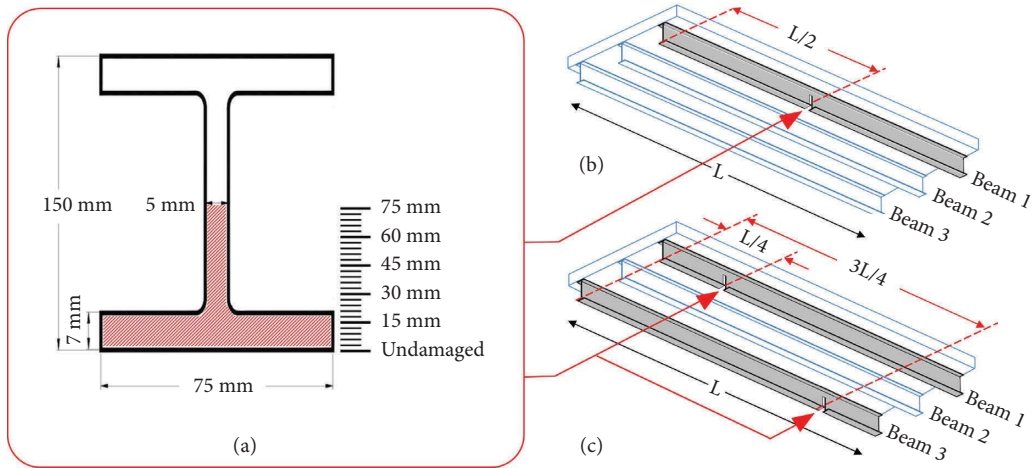
FIGURE 5: Damage simulation in the test specimen: (a) induced damage levels, (b) single-type damage location, and (c) multiple-type damage location.
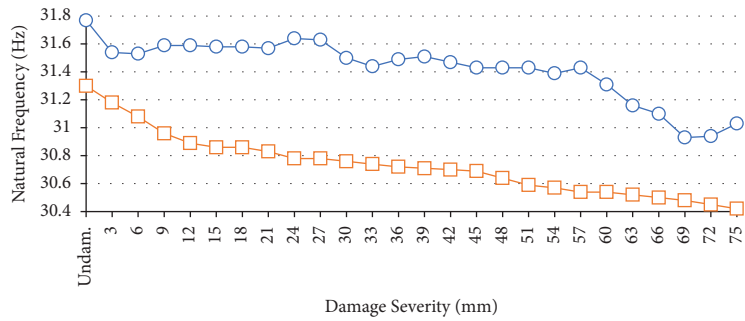
(a)
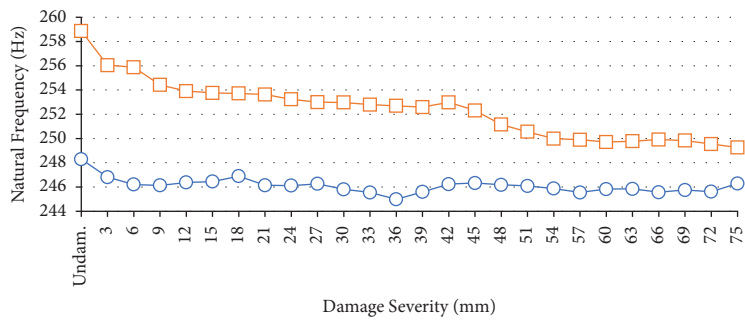
(b)

FIGURE 6: Continued.

(c)

(d)
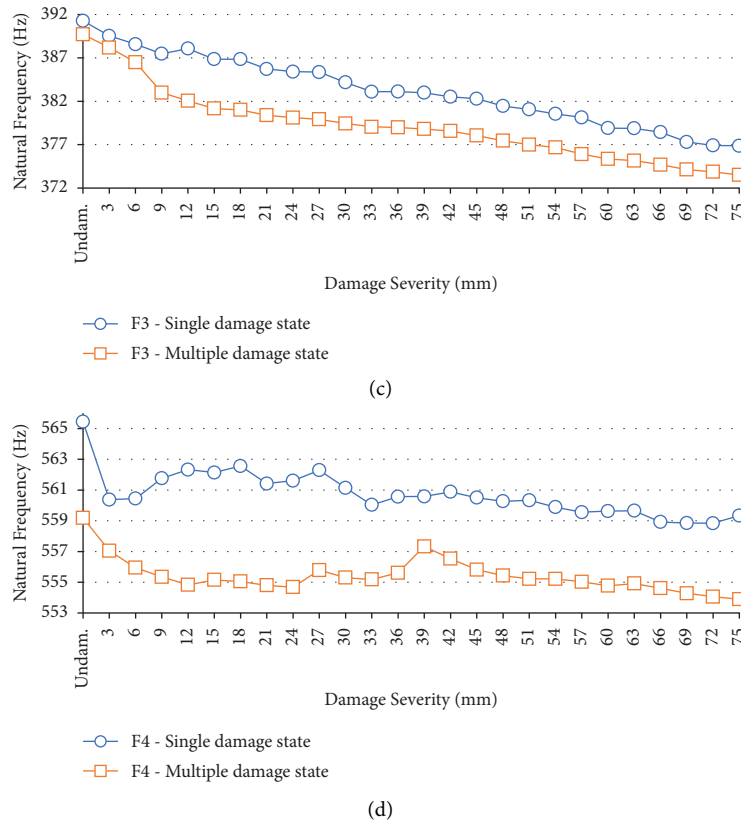
FIGURE 6: The experimental outputs of single- and multiple-type undamaged and damaged states. (a) Mode 1. (b) Mode 2. (c) Mode 3. (d) Mode 4.
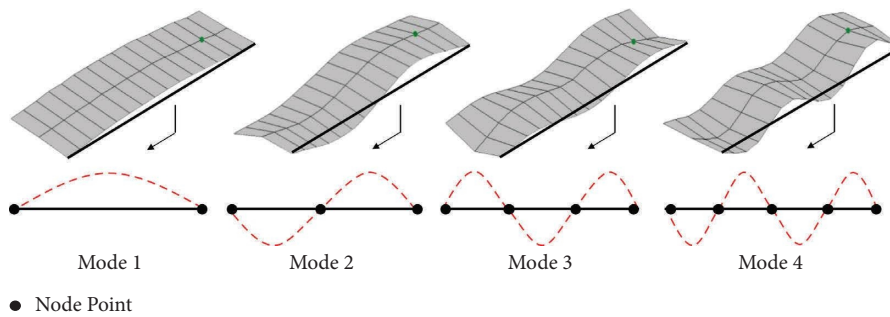
FIGURE 7: Node points of fluctuation modes.

3.2. Artificial Neural Network (ANN) Integrated with Genetic Algorithm (GA).
ANN is one of the greatest powerful AI algorithms inspired by biological neurons [80]. ANNs are categorized using their topology. For instance, a neural network can be feedback or feed-forward. In recent years, ANNs have been employed for solving civil engineering problems encountered in different structures from basic structural members (e.g., truss structures [81], reinforced concrete beams [82], and steel plates [83]) to complex systems (e.g., dams [84], buildings [85–87], and bridges [88, 89]). In spite of this, according to [90, 91], ANNs are affected by a lack of reliance on allocating the weights to networks between layers. As a result, it can increase the error

in the results of the network. In order to prevent such problems, an optimization-based algorithm can be applied in the training procedure of the network. GA holds the highest standard aimed at resolving global optimization problems [92]. This algorithm can enhance the generalization performance of artificial models. In addition, the technical advantages of GA are high parallelism, initial values independence, and outstanding robustness in the calculation of extreme values [93]. Figures 8 and 9 show the fundamental concepts and structures of ANN and GA, respectively. Based on the mentioned description, an ANN integrated with a genetic algorithm (GA) is developed in this study.

(a)

(b)
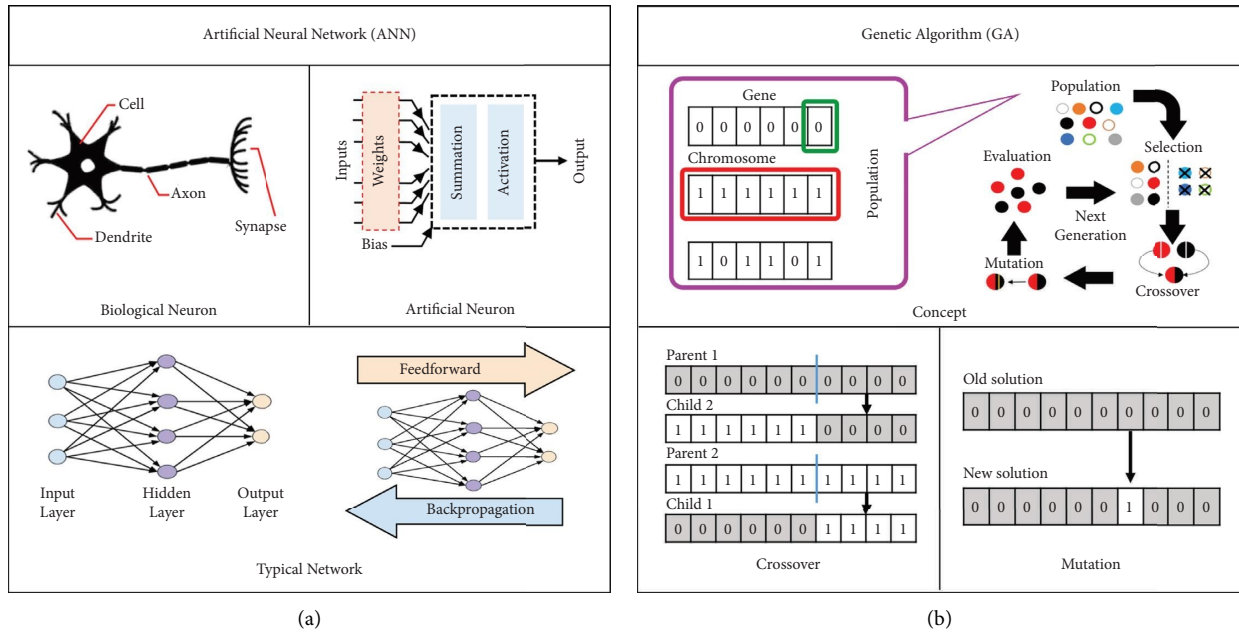
FIGURE 8: (a) ANN and (b) GA overview.

(a)

(b)
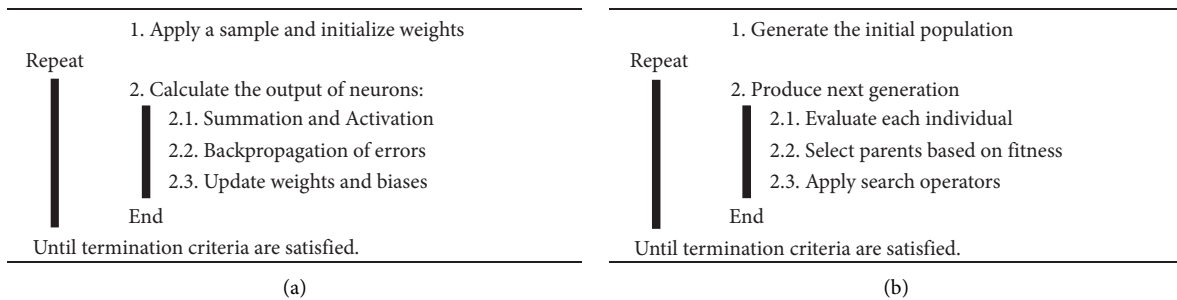
FIGURE 9: The general structure of ANN and GA. (a) Framework of backpropagation ANN. (b) Framework of GA.

4. Results and Discussion

Finite element modeling of the test structure was carried out using ABAQUS to verify the laboratory outcomes using modal frequencies. The element type for the numerical model of the I-beam was Shell homogeneous S4R, which was a 4-node doubly curved thin or thick shell, reduced integration, hourglass control, and finite membrane strains. The element type for the finite element model of the girder deck was Solid homogeneous C3D8R, which was an 8-node linear brick, reduced integration, and hourglass control. The finite element model of the I-beam and girder deck consisted of 432 and 7533 nodes and 371 and 4800 elements, respectively. After a variety of trials, the boundary condition of the model on both sides was considered as simply supported, pinned-roller with spring elements. For pinned support, rotations along the X, Y, and Z directions and translation of the Y-axis were zero. For roller support, rotation along the X and Y directions and translation of the Y-axis were zero. To associate the rigidity of the beam and supports, two springs have been modeled at the locality of the top flange of the I-

beam in the horizontal direction at roller supported side with a stiffness of 0.08 GN/m and in both supports in the vertical direction with a stiffness of 0.06 GN/m. For better understanding, the first four mode shapes in multiple-type damage scenario with 75 mm damage depth are detailed in Figure 10.

Figure 11 demonstrates the correlation between the numerical and experimental works based on finding their results. In this line, the difference between the numerical and experimental modal frequencies was around 5% in modes 1 and 2 and 2% in modes 3 and 4. Therefore, the outcomes of experimental and numerical analysis approved the validity of the findings.

As mentioned before, the ANN integrated with GA was trained using the first four experimental natural frequencies of undamaged and damaged states, i.e., F_i, $i = 1, 2, 3, 4$ as inputs and the acquired damage severities as outputs of the network. It should be noted that the database was separated into two partitions, comprising 80% for the training and 20% for the testing groups. This step was conducted by the modeling of two feed-forward neural networks for single-
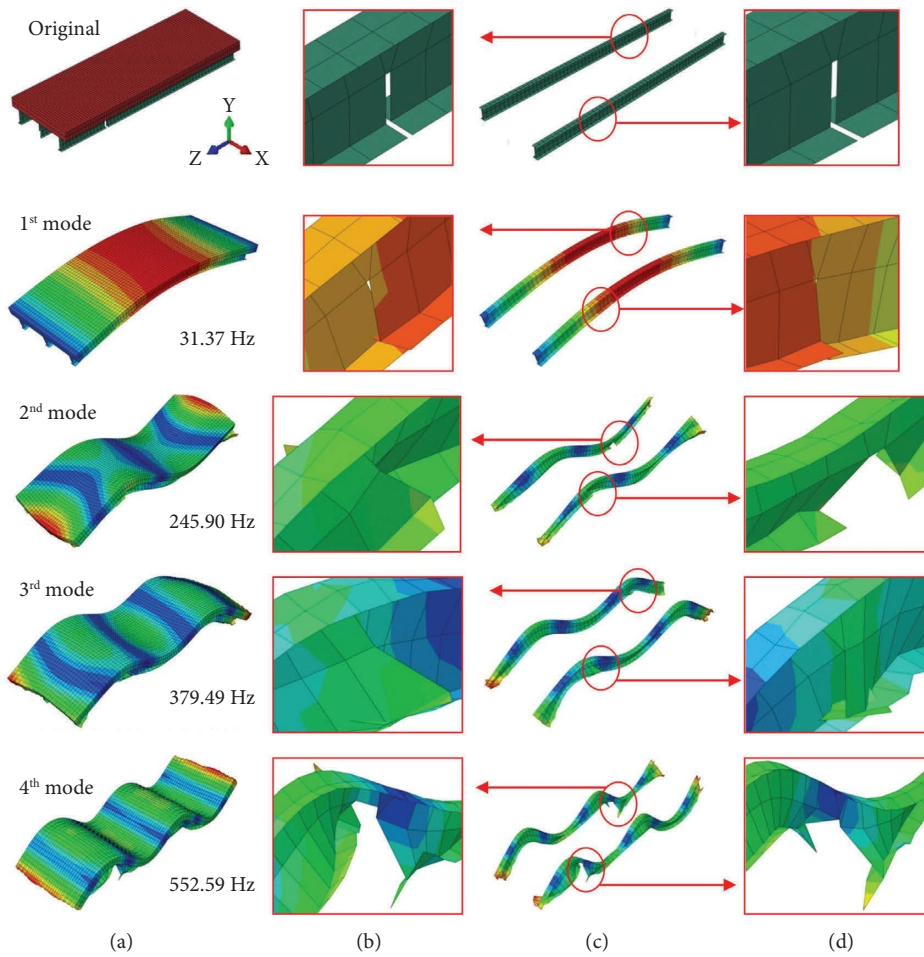
FIGURE 10: Numerical modeling of the test structure for 75 mm damage in multiple-type damage scenario. (a). Numerical model, (b) beam 1 (zoom-in), (c) beams 1 and 3, and (d) beam 3 (zoom-in).

(a)

(b)
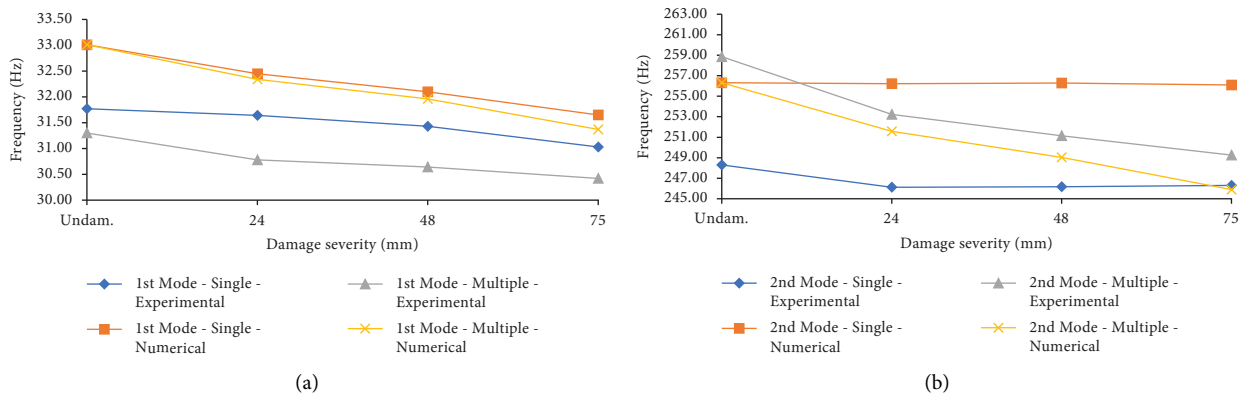
FIGURE 11: Continued.

(c)

(d)
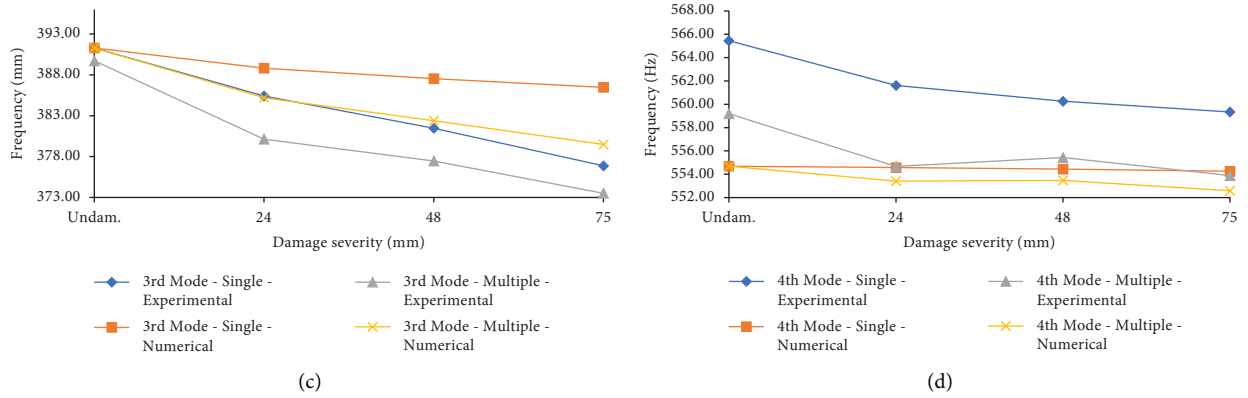
Figure 11: The difference between simulation analysis and laboratory work. (a) 1st mode. (b) 2nd mode. (c) 3rd mode. (d) 4th mode.

(a)

(b)

(c)
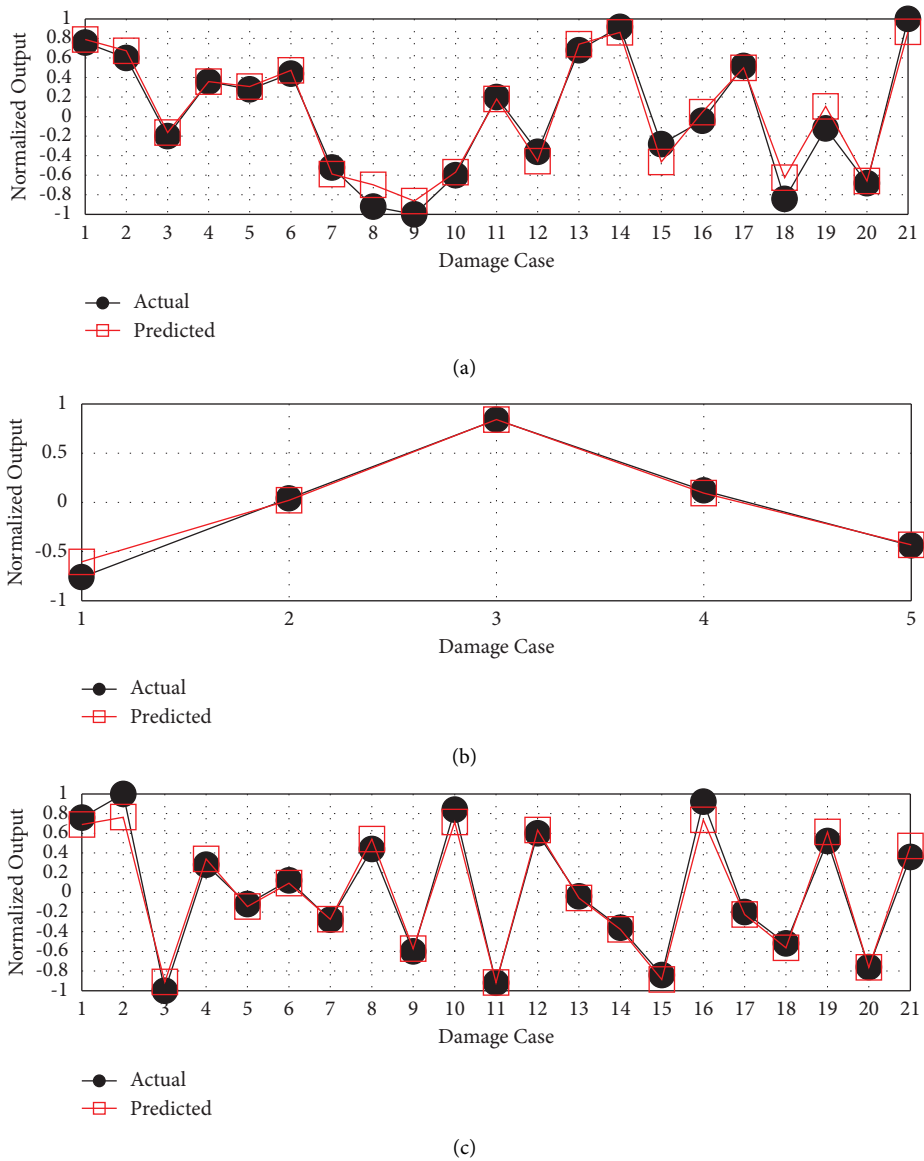
Figure 12: Continued.
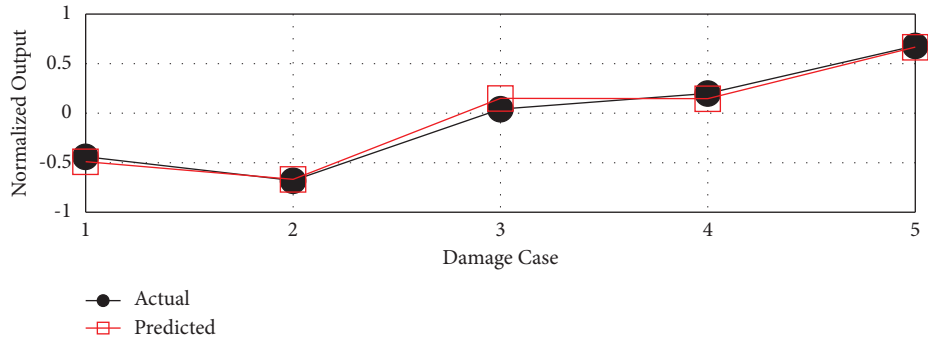
(d)

FIGURE 12: Comparison of results: (a) training section of single-type damage state, (b) testing section of single-type damage state, (c) training section of multiple damage state, and (d) testing section of multiple damage state.

TABLE 2: Comparison between the performance of patterns.

Model	Mean absolute error (MAE)	
	Training	Testing
CART	4.706	7.200
SVM	5.056	4.925
Predeveloped ANN	1.355	2.097
ANN-GA	0.070	0.084
ANN-ICA	0.057	0.075
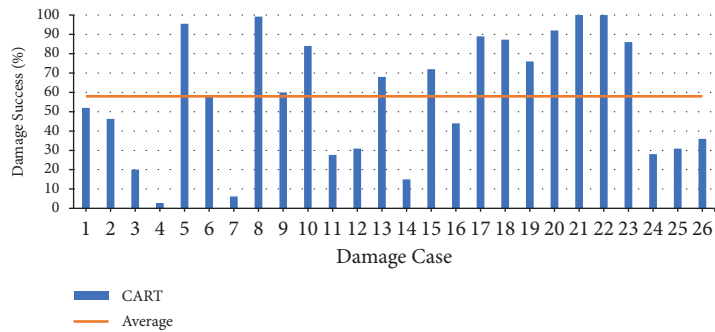
(a)
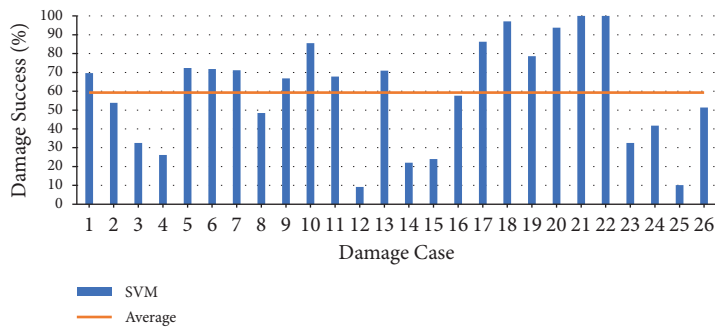
(b)

FIGURE 13: Continued.

(c)

(d)

(e)
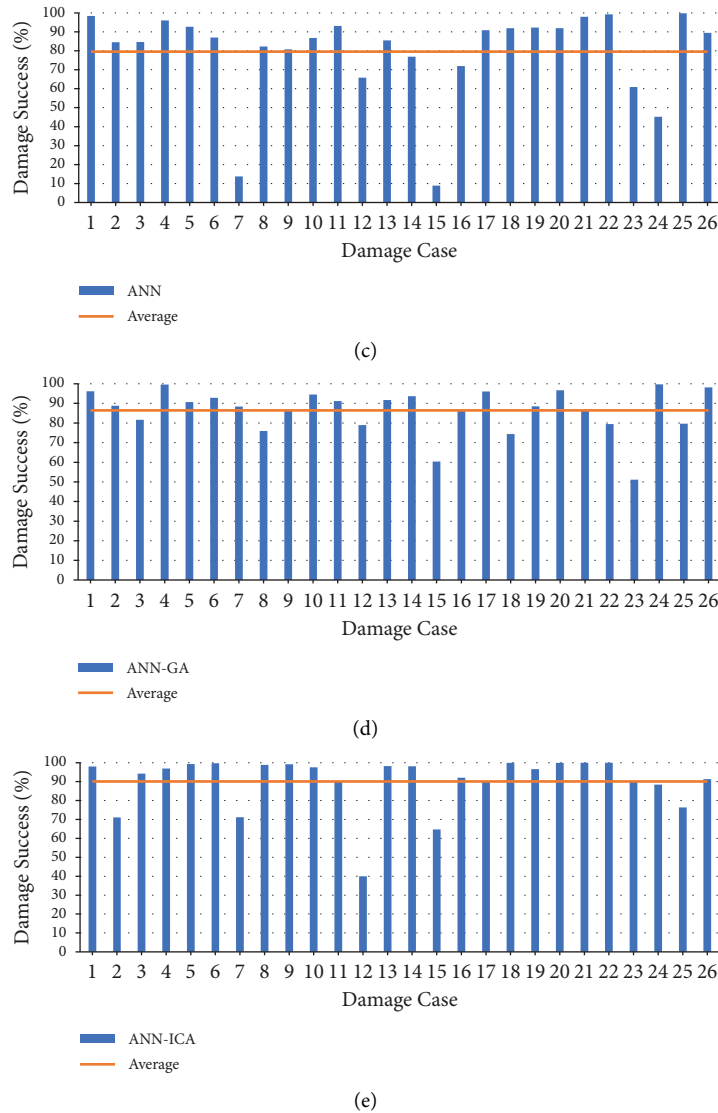
FIGURE 13: Accuracy of outputs in (a) CART, (b) SVM, (c) ANN, (d) ANN-GA, and (e) ANN-ICA.

type and multiple-type damage cases. Then, GA has been applied in the training procedure of the networks in order to reduce the cost function and improve the weights of the networks using its setting factors, i.e., population size = 150, mutation = 0.35, crossover = 0.5, and maximum generations = 50. Figures 12(a)–12(d) present the results of the developed hybrid network for single-type and multiple-type damage cases in training and testing segments, respectively. As shown in the figure, the normalized predicted damage severities were closely fitted to the actual measurements. However, the capability of individual models was not the same. For example, in the training segment of the multiple-type damage state, the calculated outcomes fitted to the actual recorded data with the matching pattern. In spite of this, the training segment of the single-type damage state gave lower fitness between forecasted and real data.

Recently, the performance of artificial intelligence, machine learning, and statistical algorithms aimed at the damage detection of the composite bridge deck structure has been reported through predeveloped ANN [94], support vector machine (SVM) [95], classification and regression trees (CART) [96], and hybrid ANN-imperial competitive algorithm (ICA) [97]. In the current work, a comparison between the aforesaid algorithms and the proposed model was made to show the performance of the developed algorithm, as shown in Table 2. Although the most appropriate robustness was succeeded by hybrid algorithms due to enhancing the learning procedure of the ANN utilizing metaheuristic algorithms, after ANN-ICA, the best MAE rates still belonged to the developed ANN integrated with GA, which were 0.070 and 0.084 for the training and testing, respectively. As shown in Table 2, the efficiency of other

methods, from best to worst succeeded by the predeveloped ANN, SVM, and CART, respectively. It is mainly attributed to the fact that the ability and complexity of artificial intelligence techniques are beyond the capacity of statistical methods.

It is also required to investigate the damage success of the patterns. In this regard, Figure 13 illustrates the accuracy of all patterns. The detection success percentage is the ratio of predicted to the actual values. According to the figure, the average percentage success is 57.95%, 59.29%, 79.58%, 86.44%, and 90.11% for CART, SVM, predeveloped ANN, ANN-GA, and ANN-ICA, respectively.

5. Conclusions

Conventional approaches in SHM and nondestructive damage detection methods are common tools for the damage assessment of civil structures. However, they are mostly time-consuming, expensive, require damage location baseline data, and limited in capacity to assess the health condition of structures, particularly for deep unobservable damages as well as large and complex structures. However, they are not beneficial to continuous monitoring, real-time, and online assessment for solving real-world problems. To overcome the mentioned drawbacks, advanced vibration-based techniques using Industry 4.0 technologies can be developed to upgrade conventional SHM, achieve sustainable-based SHM, and implement reliable and economical SHM systems. Similarly, the concept of circular economy is a strategy to promote sustainable development. By taking advantage of the relationship between circular economy, data mining, and AI, a generalized systematic fault diagnosis approach has been proposed in this study using ANN-GA. After model creation, its performance was evaluated by comparing the MAE of different computing algorithms, i.e., CART, SVM, ANN, and ANN-ICA. The results confirmed the feasibility of the proposed damage detection approach for sustainable-based damage detection of composite bridges aimed at enhancing their smartification. The damage identification is not the last phase of the proposed circular model. After pattern assessment, the implementation of strengthening and retrofitting plans is required to ensure the reliability of the structure.

Data Availability

The data used to support the findings of this study are available from the corresponding author upon request.

Conflicts of Interest

The authors declare that they have no conflicts of interest.

Acknowledgments

References

[1] A. N. Hoshyar, B. Samali, R. Liyanapathirana, A. N. Houshyar, and Y. Yu, "Structural damage detection and localization using a hybrid method and artificial intelligence techniques," *Structural Health Monitoring*, vol. 19, no. 5, pp. 1507–1523, 2019.

[2] W. Ostachowicz, R. Soman, and P. Malinowski, "Optimization of sensor placement for structural health monitoring: a review," *Structural Health Monitoring*, vol. 18, no. 3, pp. 963–988, 2019.

[3] M. Gordan, "Experimental investigation of passive tuned mass damper and fluid viscous damper on A slender two dimension steel frame," M.Sc. thesis, University Technology of Malaysia (UTM), Kuala Lumpur, Malaysia, 2014.

[4] M. Gordan, S.-R. Sabbagh-Yazdi, K. Ghaedi, D. P. Thambiratnam, and Z. Ismail, "Introduction to optimized monitoring of bridge infrastructure using soft computing techniques," in *Applied Methods in Bridge Design Optimization - Theory and Practice*IntechOpen Limited, London, UK, 2022.

[5] M. Gordan, P. Y. Siow, A. F. Deifalla, Z. C. Ong, Z. Ismail, and K. S. Yee, "Implementation of a secure storage using blockchain for PCA-FRF sensor data of plate-like structures," *IEEE Access*, vol. 10, Article ID 84837, 2022.

[6] Y. X. Qin, B. L. Li, X. Li et al., "Vibration analysis and control of nuclear power crane with MRFD," *International Journal of Applied Mechanics*, vol. 10, no. 8, Article ID 1850093, 2018.

[7] Y. Qin, Z. Q. Zhang, J. P. Gu et al., "Customized non-uniform discrete variables coordinated optimization coupling nonlinear mechanical analysis on complex truss structure," *Iran. J. Sci. Technol. Trans. Mech. Eng.*vol. 46, no. 3, pp. 617–631, 2022.

[8] M. H. Daneshvar, A. Gharighoran, S. A. Zareei, and A. Karamodin, "Structural health monitoring using high-dimensional features from time series modeling by innovative hybrid distance-based methods," *Journal of Civil Structural Health Monitoring*, vol. 11, no. 2, pp. 537–557, 2021.

[9] ASCE, "Structurally Deficient Bridges," ASCE 2021 Infrastructure Report Card, ASCE, Reston, Virginia, 2021.

[10] European Commission, *Transport in the European Union - Current Trends and Issues*, European Commission, Brussels, Belgium, 2019.

[11] M. Gordan, K. Ghaedi, Z. Ismail, H. Benisi, H. Hashim, and H. H. Ghayeb, "From conventional to sustainable SHM: implementation of artificial intelligence in the department of civil engineering," in *Proceedings of the 3rd IEEE International Conference on Artificial Intelligence in Engineering and Technology (IICAIET2021)*, pp. 1–6, University of Malaya, Kota Kinabalu, Malaysia, September 2021.

[12] M. Gordan, S.-R. Sabbagh-Yazdi, Z. Ismail et al., "State-of-the-art review on advancements of data mining in structural health monitoring," *Measurement*, vol. 193, Article ID 110939, 2022.

[13] W. Fan and P. Qiao, "Vibration-based damage identification methods: a review and comparative study," *Structural Health Monitoring*, vol. 10, no. 1, pp. 83–111, 2011.

[14] C. Z. Dong and F. N. Catbas, "A review of computer vision–based structural health monitoring at local and global levels," *Structural Health Monitoring*, vol. 20, no. 2, pp. 692–743, 2021.

[15] M. Gordan, O. Z. Chao, S.-R. Sabbagh-Yazdi, L. K. Wee, K. Ghaedi, and Z. Ismail, "From cognitive bias toward advanced computational intelligence for smart infrastructure monitoring," *Frontiers in Psychology*, vol. 13, Article ID 846610, 2022.

[16] M. Makki Alamdari, J. Li, and B. Samali, "Damage identification using 2-D discrete wavelet transform on extended operational mode shapes," *Archives of Civil and Mechanical Engineering*, vol. 15, no. 3, pp. 698–710, 2015.

[17] Y. Diao, D. Jia, G. Liu, Z. Sun, and J. Xu, "Structural damage identification using modified Hilbert–Huang transform and support vector machine," *Journal of Civil Structural Health Monitoring*, vol. 11, no. 4, pp. 1155–1174, 2021.

[18] M. Gordan, Z. Ismail, K. Ghaedi et al., "A brief overview and future perspective of unmanned aerial systems for in-service structural health monitoring," *Engineering Advances*, vol. 1, no. 1, pp. 9–15, 2021.

[19] M. Gordan, *Data mining for structural damage identification using hybrid artificial neural network based algorithm for beam and slab girder*, University of Malaya, Ph.D. thesis, 2020.

[20] M. Gordan, H. A. Razak, Z. Ismail, and K. Ghaedi, "Data mining based damage identification using imperialist competitive algorithm and artificial neural network," *Latin American Journal of Solids and Structures*, vol. 15, no. 8, pp. 1–14, 2018.

[21] M. Abdulkarem, K. Samsudin, F. Z. Rokhani, and M. F. A Rasid, "Wireless sensor network for structural health monitoring: a contemporary review of technologies, challenges, and future direction," *Structural Health Monitoring*, vol. 19, no. 3, pp. 693–735, 2020.

[22] S. Wang, S. A. Zargar, and F. G. Yuan, "Augmented reality for enhanced visual inspection through knowledge-based deep learning," *Structural Health Monitoring*, vol. 20, no. 1, pp. 426–442, 2021.

[23] P. H. Diamandis, *20 Technology Metatrends that Will Define the Next Decade*, Singularity University, Santa Clara, CA, USA, 2020.

[24] PricewaterhouseCoopers, "The essential eight technologies: how to prepare for their impact," 2016, https://www.pwc.com/us/en/tech-effect/emerging-tech/essential-eight-technologies.html.

[25] R. A. Saeed, A. N. Galybin, and V. Popov, "Crack identification in curvilinear beams by using ANN and ANFIS based on natural frequencies and frequency response functions," *Neural Computing and Applications*, vol. 21, no. 7, pp. 1629–1645, 2011.

[26] M. Gordan, Z. B. Ismail, H. Abdul Razak, K. Ghaedi, and H. H. Ghayeb, "Optimization-based evolutionary data mining techniques for structural health monitoring," *J. Civ. Eng. Constr*, vol. 9, no. 1, pp. 14–23, 2020.

[27] M. Mitchell, *An Introduction to Genetic Algorithms*, MIT Press, Cambridge, MA, USA, 1998.

[28] Y. Zhou, X. Lai, Y. Li, and W. Dong, "Ant colony optimization with combining Gaussian eliminations for matrix multiplication," *IEEE Transactions on Cybernetics*, vol. 43, no. 1, pp. 347–357, 2013.

[29] A. Noshadi, J. Shi, W. S. Lee, P. Shi, and A. Kalam, "Optimal PID-type fuzzy logic controller for a multi-input multi-output active magnetic bearing system," *Neural Computing and Applications*, vol. 27, no. 7, pp. 2031–2046, 2015.

[30] B. Xue, M. J. Zhang, and W. N. Browne, "Particle swarm optimization for feature selection in classification: a multi-objective approach," *IEEE Transactions on Cybernetics*, vol. 43, no. 6, pp. 1656–1671, 2013.

[31] A. Poteralski, M. Szczepanik, G. Dziatkiewicz, W. Kus, and T. Burczynski, "Comparison between PSO and AIS on the basis of identification of material constants in piezoelectrics," *Artif. Intell. Soft Comput. Pt Ii*, vol. 7895, pp. 569–581, 2013.

[32] P. Civicioglu and E. Besdok, "A conceptual comparison of the Cuckoo-search, particle swarm optimization, differential evolution and artificial bee colony algorithms," *Artificial Intelligence Review*, vol. 39, no. 4, pp. 315–346, 2013.

[33] G. Zhou, T. Yi, and H. Li, "Sensor placement optimization in structural health monitoring using cluster-in-cluster firefly algorithm," *Advances in Structural Engineering*, vol. 17, no. 8, pp. 1103–1115, 2014.

[34] B. Miller and L. Ziemiański, "Optimization of dynamic behavior of thin-walled laminated cylindrical shells by genetic algorithms and deep neural networks supported by modal shape identification," *Advances in Engineering Software*, vol. 147, Article ID 102830, 2020.

[35] K. Elbaz, S. L. Shen, A. Zhou, Z. Y. Yin, and H. M. Lyu, "Prediction of disc cutter life during shield tunneling with AI via the incorporation of a genetic algorithm into a GMDH-type neural network," *Engineering*, vol. 7, no. 2, pp. 238–251, 2021.

[36] U. Fayyad, G. Piatetsky-Shapiro, and P. Smyth, "Knowledge discovery and data mining: towards a unifying framework," *KDD*, vol. 96, pp. 82–88, 1996.

[37] X. Zhu, "Agile Mining: A novel data mining process for industry practice based on agile methods and visualization," Master Dissertation, University of Technology Sydney, Ultimo, Australia, 2017.

[38] P. Chapman, *CRISP-DM 1.0 Step-by-step Data Mininng Guide*, SPSS, Chicago, IL, USA, 2000.

[39] D. Stevens, *The leveraging effects of knowledge management concepts in the deployment of six sigma in a health care company*, Ph.D. thesis, Walden University, Minneapolis, MN, USA, 2006.

[40] A. Azevedo and M. F. Santos, "KDD, semma and CRISP-DM: A parallel overview," in *Proceedings of the IADIS European Conference Data Mining*, pp. 182–185, Amsterdam, The Netherlands, July 2008.

[41] S. S. Anand and A. G. Büchner, *Decision Support Using Data Mining*, Financial Times Management, London, UK, 1998.

[42] L. A. Kurgan and P. Musilek, "A survey of knowledge discovery and data mining process models," *The Knowledge Engineering Review*, vol. 21, no. 1, pp. 1–24, 2006.

[43] S. C. Chen and M. Y. Huang, "Constructing credit auditing and control & management model with data mining technique," *Expert Systems with Applications*, vol. 38, no. 5, pp. 5359–5365, May 2011.

[44] M. Gordan, Z. Ismail, H. A. Razak, and Z. Ibrahim, "Vibration-based structural damage identification using data mining," in *Proceedings of the 24th International Congress on Sound and Vibration (ICSV24)*, London, UK, 2017.

[45] M. Gordan, Z. Ismail, Z. Ibrahim, and H. Hashim, "Data mining technology for structural control systems: concept, development, and comparison," in *Recent Trends in Artificial Neural Networks*IntechOpen Limited, London, UK, 2019.

[46] M. Gordan, H. A. Razak, Z. Ismail, and K. Ghaedi, "Recent developments in damage identification of structures using data mining," *Latin American Journal of Solids and Structures*, vol. 14, no. 13, pp. 2373–2401, 2017.

[47] J. Kirchherr, D. Reike, and M. Hekkert, "Conceptualizing the circular economy: an analysis of 114 definitions," *Resources, Conservation and Recycling*, vol. 127, pp. 221–232, 2017.

[48] K. Anastasiades, J. Blom, M. Buyle, and A. Audenaert, "Translating the circular economy to bridge construction: lessons learnt from a critical literature review," *Renewable and Sustainable Energy Reviews*, vol. 117, Article ID 109522, 2020.

[49] P. Morseletto, "Targets for a circular economy," *Resources, Conservation and Recycling*, vol. 153, Article ID 104553, 2020.

[50] J. Potting, M. Hekkert, E. Worrell, and A. Hanemaaijer, *Circular Economy: Measuring Innovation in the Policy Report*, PBL Publications, Sydney, Australia, 2017.

[51] A. Nayyar and A. Kumar, *A Roadmap to Industry 4.0: Smart Production*, Sharp Business and Sustainable Development, Switzerland, Europe, 2020.

[52] A. Chauhan, S. K. Jakhar, and C. Chauhan, "The interplay of circular economy with industry 4.0 enabled smart city drivers of healthcare waste disposal," *Journal of Cleaner Production*, vol. 279, Article ID 123854, 2021.

[53] C. Kuo, J. Z. Shyu, and K. Ding, "Industrial revitalization via industry 4.0 - a comparative policy analysis among China, Germany and the USA," *Global Transitions*, vol. 1, pp. 3–14, 2019.

[54] H. Oliff and Y. Liu, "Towards industry 4.0 utilizing data-mining techniques: a case study on quality improvement," *Procedia CIRP*, vol. 63, pp. 167–172, 2017.

[55] K. Douaioui, M. Fri, C. Mabroukki, and E. L. A. Semma, "The interaction between industry 4.0 and smart logistics: concepts and perspectives," in *Proceedings of the 2018 International Colloquium on Logistics and Supply Chain Management (LOGISTIQUA)*, pp. 128–132, Tangier, Morocco, April 2018.

[56] M. Talebkhah, A. Sali, M. Marjani, M. Gordan, S. J. Hashim, and F. Z. Rokhani, "IoT and big data applications in smart cities: recent advances, challenges, and critical issues," *IEEE Access*, vol. 9, Article ID 55465, 2021.

[57] M. Gordan, Z. Ismail, F. A. M. Rahim et al., "Defining A conceptual framework for vibration-based damage detection platforms using blockchain," *J. Civ. Eng. Mater. Appl.*, vol. 5, no. 1, pp. 25–33, 2021.

[58] Ellen Macarthur Foundation, *Artificial Intelligence and the Circular Economy*, Ellen Macarthur Foundation, Cowes, UK, 2019.

[59] Ellen MacArthur Foundation, *Intelligent Assets: Unlocking the Circular Economy Potential*, Cowes, UK, 2016.

[60] S. Jørgensen and L. J. T. Pedersen, "The circular rather than the linear economy," pp. 103–120, Palgrave Macmillan, London, UK, 2018.

[61] G. L. F. Benachio, M. D. C. D. Freitas, and S. F. Tavares, "Circular economy in the construction industry: a systematic literature review," *Journal of Cleaner Production*, vol. 260, Article ID 121046, 2020.

[62] J. S. Mboli, D. K. Thakker, and J. L. Mishra, "An Internet of Things-enabled decision support system for circular economy business model," *Software: Practice and Experience*, vol. 52, no. 3, pp. 772–787, 2020.

[63] M. Borrello, S. Pascucci, and L. Cembalo, "Three propositions to unify circular economy research: a review," *Sustainability*, vol. 12, no. 10, p. 4069, 2020.

[64] J. Gillabe, F. Gross, H. Wilts, and R. Zoboli, *Circular Economy in Europe - Developing the Knowledge Base*, EEA, Denmark, Europe, 2016.

[65] J. Gallagher, B. Basu, M. Browne et al., "Adapting stand-alone renewable energy technologies for the circular economy through eco-design and recycling," *Journal of Industrial Ecology*, vol. 23, no. 1, pp. 133–140, 2019.

[66] I. D. Adamo, "Adopting a circular economy: current perspectives and future perspectives," *Social Sciences*, vol. 8, no. 328, 2019.

[67] A. P. M. Velenturf and P. Purnell, "Principles for a sustainable circular economy," *Sustainable Production and Consumption*, vol. 27, pp. 1437–1457, 2021.

[68] W.-W. Wu, Y.-T. Lee, M.-L. Tseng, and Y.-H. Chiang, "Data mining for exploring hidden patterns between KM and its performance," *Knowledge-Based Systems*, vol. 23, no. 5, pp. 397–401, 2010.

[69] J. Lingxia, *Research on Distributed Data Mining System and Algorithm Based on Multi-Agent*, University of Quebec, Quebec, Canada, 2009.

[70] J. Tinoco, A. Gomes Correia, and P. Cortez, "Support vector machines applied to uniaxial compressive strength prediction of jet grouting columns," *Computers and Geotechnics*, vol. 55, pp. 132–140, 2014.

[71] S. Saitta, B. Raphael, and I. F. C. Smith, *Data Mining: Applications in Civil Engineering*, VDM, Saarbrücken, Germany, 2009.

[72] D. W. M. Hofmann and J. Apostolakis, "Crystal structure prediction by data mining," *Journal of Molecular Structure*, vol. 647, no. 1–3, pp. 17–39, 2003.

[73] C. Qu, T. Yi, and H. Li, "Mode identification by eigensystem realization algorithm through virtual frequency response function," *Structural Control and Health Monitoring*, vol. 26, no. 10, 2019.

[74] C.-X. Qu, T.-H. Yi, and H.-N. Li, "Modal identification for superstructure using virtual impulse response," *Advances in Structural Engineering*, vol. 22, no. 16, pp. 3503–3511, 2019.

[75] H. Monajemi, *Model updating and damage detection of frame structures using output-only measurements*, Ph.D. thesis, University of Malaya, Kuala Lumpur, Malaysia, 2018.

[76] Q. Jiao, Y. Qin, Y. Han, and J. Gu, "Modeling and optimization of pulling point position of luffing jib on portal crane," *Mathematical Problems in Engineering*, vol. 2021, no. 2, pp. 21–8, 2021.

[77] C. G. Chiorean and S. M. Buru, "Practical nonlinear inelastic analysis method of composite steel-concrete beams with partial composite action," *Engineering Structures*, vol. 134, pp. 74–106, 2017.

[78] Oros, "NVGate, the teamwork instruments interface," 2015, https://www.oros.com/solutions/data-acquisition-and-signal-processing/.

[79] Modent, *"Icats" Imperial College of Analysis, Testing, and Software*, Modent, London, UK, 1998.

[80] T. H. Kwon, S. H. Park, S. I. Park, and S. H. Lee, "Building information modeling-based bridge health monitoring for anomaly detection under complex loading conditions using artificial neural networks," *Journal of Civil Structural Health Monitoring*, vol. 11, no. 5, pp. 1301–1319, 2021.

[81] B. Xu, G. Chen, and Z. S. Wu, "Parametric identification for a truss structure using axial strain," *Computer-Aided Civil and Infrastructure Engineering*, vol. 22, no. 3, pp. 210–222, 2007.

[82] C. A. Jeyasehar and K. Sumangala, "Nondestructive evaluation of prestressed concrete beams using an artificial neural

network (ANN) approach," *Structural Health Monitoring*, vol. 5, no. 4, pp. 313–323, Dec. 2006.

[83] S. Goswami and P. Bhattacharya, "A scalable neural-network modular-array architecture for real-time multi-parameter damage detection in plate structures using single sensor output," *International Journal of Computational Intelligence and Applications*, vol. 11, no. 4, Article ID 1250024, 2012.

[84] J. Li, U. Dackermann, Y. Xu, and B. Samali, "Damage identification in civil engineering structures utilizing PCA-compressed residual frequency response functions and neural network ensembles," *Structural Control and Health Monitoring*, vol. 18, no. 2, pp. 207–226, 2011.

[85] S. Hung, C. S. Huang, C. M. Wen, and Y. C. Hsu, "Non-parametric identification of a building structure from experimental data using wavelet neural network," *Computer-Aided Civil and Infrastructure Engineering*, vol. 18, no. 5, pp. 356–368, 2003.

[86] V. Kanwar, N. Kwatra, and P. Aggarwal, "Damage detection for framed RCC buildings using ANN modeling," *International Journal of Damage Mechanics*, vol. 16, no. 4, pp. 457–472, Jul. 2007.

[87] X. Jiang and S. Mahadevan, "Bayesian probabilistic inference for nonparametric damage detection of structures," *Journal of Engineering Mechanics*, vol. 134, no. 10, pp. 820–831, 2008.

[88] S. Kabir, P. Rivard, and G. Ballivy, "Neural-network-based damage classification of bridge infrastructure using texture analysis," *Canadian Journal of Civil Engineering*, vol. 35, no. 3, pp. 258–267, Mar. 2008.

[89] V. Mosquera, A. W. Smyth, and R. Betti, "Rapid evaluation and damage assessment of instrumented highway bridges," *Earthquake Engineering & Structural Dynamics*, vol. 41, no. 4, pp. 755–774, 2012.

[90] L. S. Lee and S. Charles, "Investigation of integrity and effectiveness of RC bridge deck rehabilitation with CFRP composites," *Structural Systems Research Project*, University of California, San Diego, CA, USA, 2004.

[91] R. P. Bandara, *Damage identification and condition assessment of building structures using frequency response functions and neural networks*, Ph.D. thesis, Queensland University of Technology, Brisbane, Australia, 2013.

[92] M. Whelan, N. Salas Zamudio, and T. Kernicky, "Structural identification of a tied arch bridge using parallel genetic algorithms and ambient vibration monitoring with a wireless sensor network," *Journal of Civil Structural Health Monitoring*, vol. 8, no. 2, pp. 315–330, 2018.

[93] H. Gao, Y. Qin, L. Zhao, J. Gu, and F. Wang, "Competitor benchmarking by structure reliability analysis with improved response surface method," *Arabian Journal for Science and Engineering*, vol. 47, no. 12, Article ID 16331, 2022.

[94] Z. X. Tan, D. P. Thambiratnam, T. H. T. Chan, M. Gordan, and H. Abdul Razak, "Damage detection in steel-concrete composite bridge using vibration characteristics and artificial neural network," *Structure and Infrastructure Engineering*, vol. 16, no. 9, pp. 1247–1261, 2020.

[95] M. Gordan, S.-R. Sabbagh-Yazdi, Z. Ismail, K. Ghaedi, and H. H. Ghayeb, "Data mining-based structural damage identification of composite bridge using support vector machine," *J. Artif. Intell. Data Min.* vol. 9, no. 4, pp. 415–423, 2021.

[96] M. Gordan, H. A. Razak, Z. Ismail, K. Ghaedi, Z. X. Tan, and H. H. Ghayeb, "A hybrid ANN-based imperial competitive algorithm methodology for structural damage identification of slab-on-girder bridge using data mining," *Applied Soft Computing*, vol. 88, Article ID 106013, 2020.

[97] M. Gordan, Z. Ismail, H. Abdul Razak et al., "Data mining-based damage identification of a slab-on-girder bridge using inverse analysis," *Measurement*, vol. 151, Article ID 107175, 2020.

Research Article

Potential Structural Damage Characterization through Remote Sensing Data: A Nondestructive Experimental Case Study

Marta Terrados-Cristos [ID]**, Francisco Ortega-Fernández** [ID]**, Marina Díaz-Piloneta** [ID]**, Vicente Rodríguez Montequín, and Javier García González** [ID]

Project Engineering Department, University of Oviedo, Oviedo 33004, Spain

Correspondence should be addressed to Marta Terrados-Cristos; marta.terrados@api.uniovi.es

Atmospheric corrosion, especially in coastal environments, is a major structural problem affecting metallic structures in various sectors. Structural health monitoring systems based on satellite information can help to ensure the proper behavior of civil structures and are an interesting alternative for remote locations. The aim of this case study is to relate remote sensing information to the results of experimental studies for potential structural damage characterization. The ultimate idea is to characterize any environment without long testing periods or sampling costs. Comparative nondestructive experimental tests involving different locations, sampling techniques, and study periods are performed. The results obtained are analyzed and compared with meteorological satellite data characterization at each site. The experimental test results show sufficient statistical significance ($p < 0.05$), confirming that the areas potentially most susceptible to corrosion can be identified using information from remote sensing satellites based on orientation, wind conditions, and wind origin. This can be used to facilitate the remote design and monitoring of structures more accurately with a stability guarantee.

1. Introduction

Civil structures deteriorate in various ways [1]. The principal causes of damage, failure, or even collapse of a civil structure are aging, climate conditions, deterioration of some components, deficient designs, and natural disasters [2, 3]. Although some of these issues can cause rapid failure [4], damage due to corrosion or fatigue tends to occur over extended periods of time. Nevertheless, these damages can be prevented if corrective actions are taken timely [5]. Therefore, it is of the utmost importance to monitor civil structures continuously to assess their structural conditions and provide early warning against structural damage [6].

Corrosion is one of the major structural defects in metallic structures [7], particularly in coastal environments [8]. Moreover, the fact that this problem can occur in any area [9] complicates its visual assessment, which is already an expensive, imprecise, and time-consuming task [10]. Traditional approaches for damage diagnosis of civil

structures are mainly based on visual inspection. However, the size and conditions of the structures make this process increasingly difficult. Globalization has led to the design and development of many remote projects, which complicates routine monitoring and highlights the importance of using satellite remote sensing data to study environmental problems on a global scale [11].

Structural health monitoring (SHM) is an important process for assessing the health and integrity of civil structures to prevent structural damage [12]. SHM systems are widely used to achieve adequate performance in civil structures [13] and proper maintenance management [14]. Progress in technology and sensors has led to the transformation of SHM into a new form of monitoring [4, 15]. SHM systems generally include damage detection, location, and quantification [16], and damage detection is precisely the most critical one [1].

SHM is a broad and highly interdisciplinary field of research involving experimental testing, system

identification, data acquisition and management, and long-term measurement of the environmental and specific operational conditions [17, 18]. Numerous damage detection applications can be found in almost every field.

Owing to recent advances in sensing and data acquisition systems, the use of these techniques in engineering applications has become an interesting development. There are multiple examples of different applications, such as modeling structural resistance and response [19, 20], studies based on vibration control [1, 12, 21], using machine learning techniques in SHM [16, 17, 22–24], and new approaches, such as smartphone-centric multisensory solutions [4].

All of them are trying to monitor, predict, or prevent damage from occurring, as early damage detection is an important concern for the scientific civil community [25]. However, a more efficient approach is to design or redesign structures based on these potential problems.

Most civil engineering projects involve metallic structures, generally made of bare or coated steel [26], which suffer from atmospheric corrosion [27]. Structural degradation in coastal areas is a particularly important problem because of its significance to society [28]. Approximately 40% of the world's population lives within 100 km of the coast [29] and it is precisely in these areas where industries are often located. Many studies have corroborated that the deposition rate of chloride is a critical factor that affects the atmospheric corrosion of metals [30] and the influence of chloride-contaminated environments on durability [31].

Thus, experimentally studying the deposition mechanisms of this atmospheric pollutant and relating the results to remote satellite data can help to predict and prevent potential structural damage. Hence, with prior knowledge of the most susceptible locations, it may not be necessary to allocate resources to monitor large, complex civil structures and the problem of SHM monitoring may be limited to certain areas.

Therefore, the main objective of this study was to propose a novel method for preliminary analysis of potential structural damage. The aim of this case study was to relate remote sensing information to the results of nondestructive experimental studies for potential structural damage characterization. This approach provides valuable information in a simple manner. Consequently, it makes it possible to design and monitor structures remotely and more accurately.

2. Materials and Methods

An outline of the methodology used in this study is shown in Figure 1. The first stage consisted of characterizing each site and studying its meteorological variables (temperature, relative humidity, wind speed, wind direction, and precipitation). Climatic information was obtained from remote-sensing satellites. This information was downloaded and processed to create a global database using Web servers. The next step in structuring and homogenizing the study data began by identifying and cleaning anomalous values. In addition, basic statistical analyses (means, deviations, maxima, minima, etc.) were performed. To ensure representativeness, these variables and their relationships were analyzed both during the study period and in the previous year. The possible relationships between the variables were studied, and the results were represented graphically for their correct interpretation.

The second stage included experimental studies. Sample preparation, using one of the three techniques further explained in Section 3.1, was performed according to what is indicated in the ISO 9225 : 2012 standard "Corrosion of metals and alloys. Corrosivity of atmospheres. Measurement of environmental parameters affecting the corrosivity of atmospheres" [32]. The samples were then exposed. Control samples were added in all cases. Subsequently, once the test period was completed, the samples were removed, processed as indicated in the standards, and analyzed by ion chromatography (METROHM 883 Basic IC plus).

In the third and last stage, the results of the tests were analyzed together with the results of the meteorological characterization of satellite data, which allowed drawing joint conclusions.

2.1. Sample Preparation.
Three techniques were used to determine the chloride deposition. The ISO 9225 : 2012 standard sets the procedures for sample preparation using the wet candle and dry plate methods. As the previous methods were found to have limitations, it was necessary to develop a more accurate method to differentiate the impact of wind and rain, so the third option used in this experimental study was a new method based on the wet candle method (hereinafter referred to as "Covered candle").

2.1.1. Dry Plate.
This technique is based on exposing a known area of double-layered gauze protected from rain and measuring by chemical analysis the amount of captured chlorides coming from one direction and deposited on the surface of the gauze. Chloride deposition is expressed in milligrams per square meter per day [$mg \cdot m^{-2} \, day^{-1}$]. Sample preparation, test duration, management of the final solution, and calculation of results are defined in Annex E of ISO 9225 : 2012 [32].

2.1.2. Wet Candle.
The technique consists of a wet textile surface wrapped in the form of a cylinder and a water reservoir to maintain the wet condition of the gauze. This method allows the collection of aerosols from all directions. The amount of chloride deposited is determined by chemical analysis, and subsequently, the chloride deposition rate [$mg \cdot m^{-2} \, day^{-1}$] is calculated.

The sampling devices and solution used and the collection of the samples and the final calculation of the deposition are described in Annex D of ISO 9225 : 2012 [32].

2.1.3. Covered Candle.
This is an altered version of the wet candle method, which provides an option for monitoring the effect of precipitation on the final chloride ion deposition. The main limitation of the wet candle method is that it does
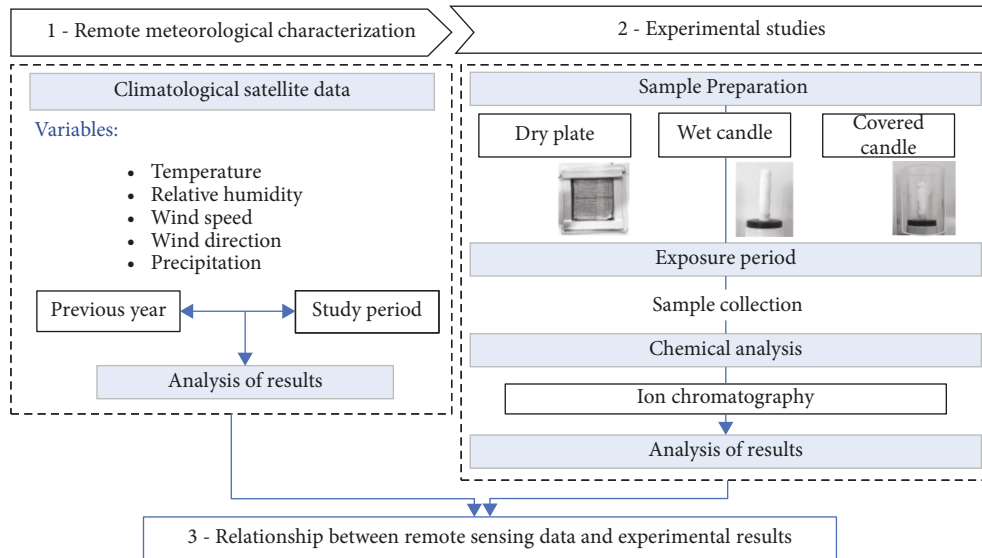
FIGURE 1: Outline of the common methodology for all tests.
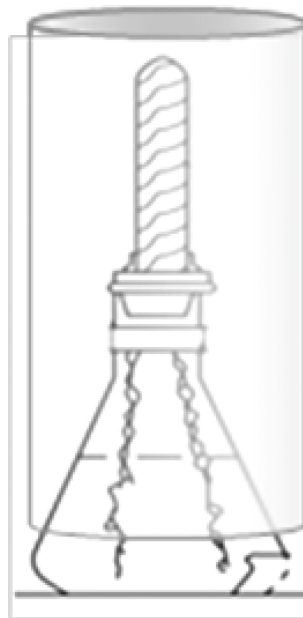
FIGURE 2: Proposed scheme for sample's collection in the covered candle method.

not allow differentiation between pollutant deposition by wind and pollutants deposited by rain. Cases where structures are located protected from wind but perfectly exposed to rain (e.g., in squares surrounded by skyscrapers) are suitable for this approach. This method includes a cover of plastic or similar material to isolate the sample from wind action (see the scheme in Figure 2).

2.2. Test Description. Three different experimental tests were conducted throughout the investigation. Each of them attempts to analyze and clarify a different hypothesis and study the influence of one or multiple climatic variables on the final pollutant deposition.

2.2.1. Test I: Influence of Wind Direction and Wind Origin on Chloride Deposition. Previous chloride deposition models only consider the distance to the sea, but this generates errors. The aim of this test was to analyze the influence of the relative wind position, together with the importance of the origin of the wind (wind from the sea or from land), in an
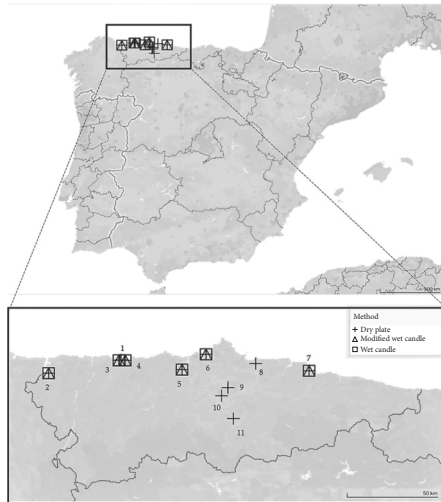
FIGURE 3: Location of samples in northern Spain distributed for all three different tests.

FIGURE 4: Distribution of all three tests and their locations over time.

attempt to clarify why there are differences between deposition for the same distance and atmospheric conditions.

Samples in the same location were set in four different positions: upwind + wind coming and not coming from the sea, and downwind + wind coming and not coming from the sea. To achieve the objective described for Test I, tests were carried out at two successive time intervals. Thus, given the characteristics of the local wind and the possible positions of the samples in the four cardinal orientations, it was possible to obtain the range of events to be studied using the above-described dry plate technique.

2.2.2. Test II: Influence of Location, Orientation, and Atmospheric Conditions on Chloride Deposition. The aim of this test was to analyze the influence of the distance from the sample to the pollutant emitting source together with some other atmospheric variables (temperature, precipitation, wind, and relative humidity) and to consider the relative position between the structure and prevailing wind direction at each site.

The aim was to determine which wind speed thresholds appear in chloride deposition and transportation under such circumstances. In addition, the role of wind direction with respect to precipitation was studied. All samples were distributed at different distances from the sea at the locations shown in Figure 3, and the dry plate technique was employed.

2.2.3. Test III: Influence of Precipitations and Wind on Chloride Deposition. This third test studied the influence of precipitation on pollutant deposition and the role of precipitation in the presence and absence of wind.

The results obtained by the two different techniques were compared: the wet candle technique and its new version. Thus, one method involved total exposure to atmospheric variables and the other was isolated from the wind. The samples were collected at different points in the region. The final sample distributions at different test points are shown in Figure 3. The experimental sites include one-, two-, or three-sample techniques.
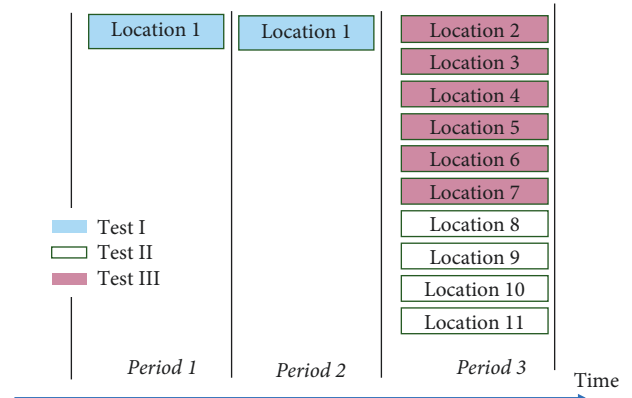
The time planning for the three tests is presented in Figure 4. The combinations of the different tests and locations are indicated by the colors of the bar and outline. It can be observed how some locations participated in Tests I and II, others only in Test II, and the third selection of locations in Tests II and III, based on climatological conditions and availability.

Table 1 summarizes the methods, locations, and study periods for each of the three tests.

2.3. Statistical Analysis. Data obtained from the experimental tests were statistically analyzed using SPSS 22.0 software. Student's t-test for independent samples was used to assess whether there were significant statistical differences between the means at a confidence level of $p < 0.05$.

3. Results and Discussion

3.1. Results of Meteorological Characterization

3.1.1. Precipitations. Figure 5(a) shows the accumulated precipitation for each location during the study period, represented by vertical bars. As test I was performed over two different periods. In Figure 5, location 1 was divided into 1a and 1b, referring to these two study periods. At location 1, hardly any rainfall occurred during the first test interval (1a). In the second test interval (1b) at the same location, the rainfall increased considerably. For the rest of the locations, similar results were observed, with abundant precipitation, except for one specific location (number 8).

Figure 5(b) presents the distribution of precipitation data over time. Each line represents the location. Although the number of lines is large and visualization may be difficult, it is clearly observed that the weather was rather dry at the beginning, with a large amount of rainfall at the end for all sites.

TABLE 1: Summary of the different techniques, locations, and study periods involved in the three tests.

	Technique			Location		Study period	
	Dry plate	Wet candle	Covered candle	One location	Multiple locations	One period	Two periods
Test I	x			X			x
Test II	x				x	x	
Test III		x	x		x	x	

(a)   (b)
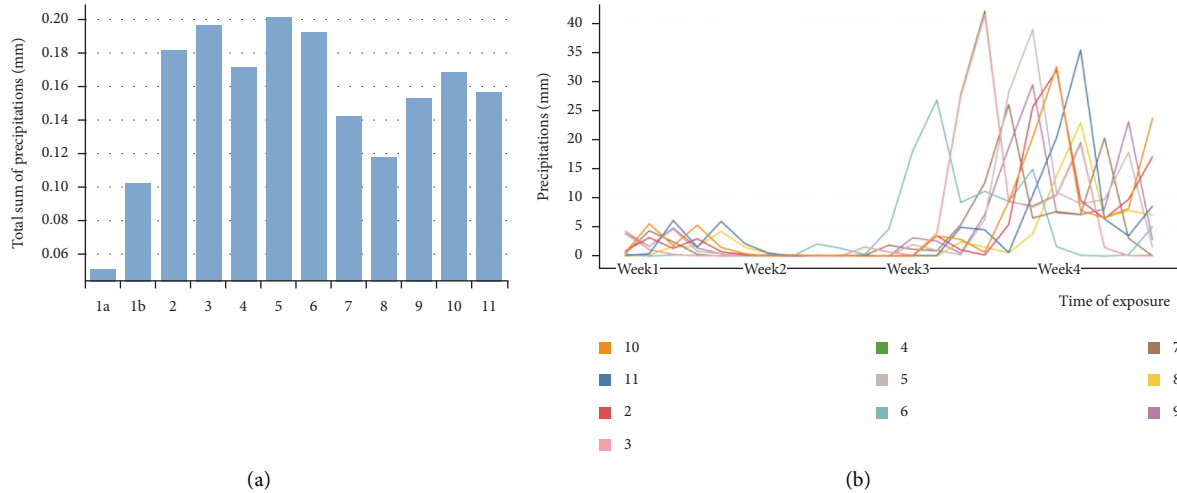
FIGURE 5: (a) Cumulative rainfall during the study periods at each location. (b) Distribution of rainfall by location over time.

3.1.2. Relative Humidity and Temperature.

As stated in the literature, both relative humidity [33, 34] and temperature [35] may be parameters influencing atmospheric corrosion. Nevertheless, the average relative humidity during the sampling period and the average temperature at each location did not vary sufficiently during that period to be considered influential.

3.1.3. Wind Speed.

Wind analysis is more complex because, in addition to wind speed, wind gusts and direction are also important [36–38]. Some authors agree that the influence of wind speed becomes clearer above a certain threshold; however, there is no single reference value [39, 40]. At none of the locations were very high wind speeds recorded; however, it is true that the closer to the sea, the higher the average wind speeds.

However, the maximum wind gusts measured during the study period showed winds of up to 12 m/s at some points along the coast. In the central areas and farther away from the coast, the highest measured speeds did not exceed 6 m/s.

3.1.4. Wind Direction.

Finally, in addition to wind speed, wind direction plays a relevant role. Analyzing the prevailing winds at a given location can help identify the most dangerous areas [41]. To study the possibility of relating monthly wind directions to annual wind directions, predominant wind directions over the study period were compared to wind directions considering annual data (year 2020). After analyzing this parameter, the results provided relevant conclusions from several perspectives (Figure 6). First, when

comparing the prevailing winds of the study period in the year 2021 (green arrow), it was observed that they remained perfectly consistent with the prevailing directions obtained during the same period in the previous year (yellow arrow), as no yellow arrows could be seen. However, the prevailing directions for a specific period do not necessarily correspond with the annual directions (blue arrow).

Another important factor was the sensitivity of the prevailing wind direction at each point. As stated above and as many authors agree [39, 40, 42], there are minimum wind speeds (threshold speeds) for the transport of pollutants over long distances. Below this threshold, the wind is not sufficiently strong. However, determining this threshold is complex. For the same study period, considering a certain minimum wind speed condition, the results of the predominant wind direction may also change. Prior to these calculations of the predominant directions, the results are filtered so that only values greater than a certain threshold speed (3 m/s (red arrow) and 2 m/s (orange arrow)) are considered, and the directions may vary. The values of the predominant directions could be changed only by varying the threshold velocity by 1 m/s, which shows the complexity of this parameter.

3.2. Results of Experimental Studies

3.2.1. Test I.

The results of the localized test are presented in Figure 7. The upper part of the figure shows the chloride deposition results during the first time interval (left) and the second time interval (right). Below, the wind rose during each study period is included. The blue dots represent the
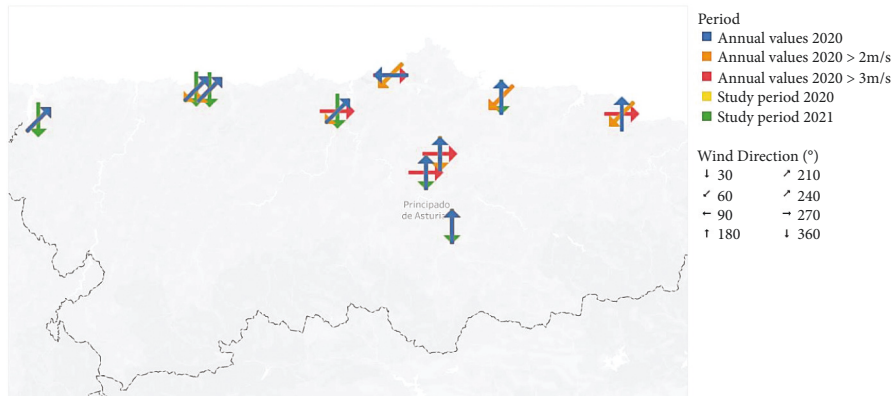
Figure 6: Prevailing wind directions at different sampling sites and periods.

north-facing samples (facing the sea) and the orange dots represent the south-facing samples (not facing the sea). In addition, the triangular shape represents the height of the samples; where the triangles with the tip upward, the samples are at the highest altitude.

Analyzing all this together, we observe the first period with a predominantly north-easterly wind of marine origin. The windward samples showed higher depositions at both heights, and the difference from the south-facing samples was very clear. In contrast, during the second study period, the prevailing winds were from the SW, and although the capacity of the wind to transport particles was approximately the same in both periods (similar wind speeds and frequencies), the final result was not similar. Therefore, the origin of the wind (marine or nonmarine) was the most important and relevant difference between the two studies.

Other studies have analyzed the importance of the orientation of the structure for pollutant deposition [41] but not whether the wind comes from an emitting source or from another direction.

Comparing the differences in pollutant deposition between the north and south faces during the first study period, a highly significant difference was observed ($p < 0.00028$). In contrast, if the same comparison was made during the second study period, no significant difference ($p > 0.16$) in the deposition of marine pollutants was observed between the samples that received more wind but had a nonmarine origin and those with little exposure to the wind but whose wind came from the sea.

The clearest differences were observed when comparisons were made between the two study periods. In the samples exposed to the north and, therefore, directly exposed to the sea, there was a large difference ($p < 4.11\,\mathrm{E}^{-05}$) between the two periods.

If the wind energies were compared as proposed by Meira et al. [39] to detect if they were equivalent, it was observed that the energy of pollutant transport was practically the same, as the difference was not very significant ($p > 0.1$), but the deposition results again showed clear differences ($p < 0.03$).

However, this is undoubtedly not the only influential factor. In the analysis of the precipitation results mentioned above (Figure 6), during the first study period, the accumulated precipitation was up to four times lower than that in the second period, where, although it did not rain excessively, it did rain much more than in the previous period. Thus, the chloride ions were not in the air ready to be transported but on the surface.

Comparing the results, even if there was a difference in precipitation between periods, which decreased the pollutant content of the atmosphere [35], there was no difference in deposition ($p < 0.03$); therefore, the relationship between wind orientation and origin was the most relevant factor.

This could confirm two points:

(i) In addition to the importance of the relative position between the orientation of the prevailing wind and the structure, the origin of these wind gusts is also important because if the wind is very strong but does not come from the sea but from inland, it may bring fewer chloride ions.

(ii) The role of the wind cannot be understood as an isolated variable, and precipitation (periodicity, quantity, etc.) seems to be important too, not so much for its action as a transport mechanism but for its interaction with the environment, cleaning the structures or reducing the chloride content in the atmosphere, Wash-out effect [43].

Finally, regarding this first test, when comparing the results of the deposition differences relative to elevation, as proposed in [44, 45], we agreed that for this case study, at a distance of only 4 m as in the present situation, no clear differences ($p > 0.31$) were observed between the two scenarios.
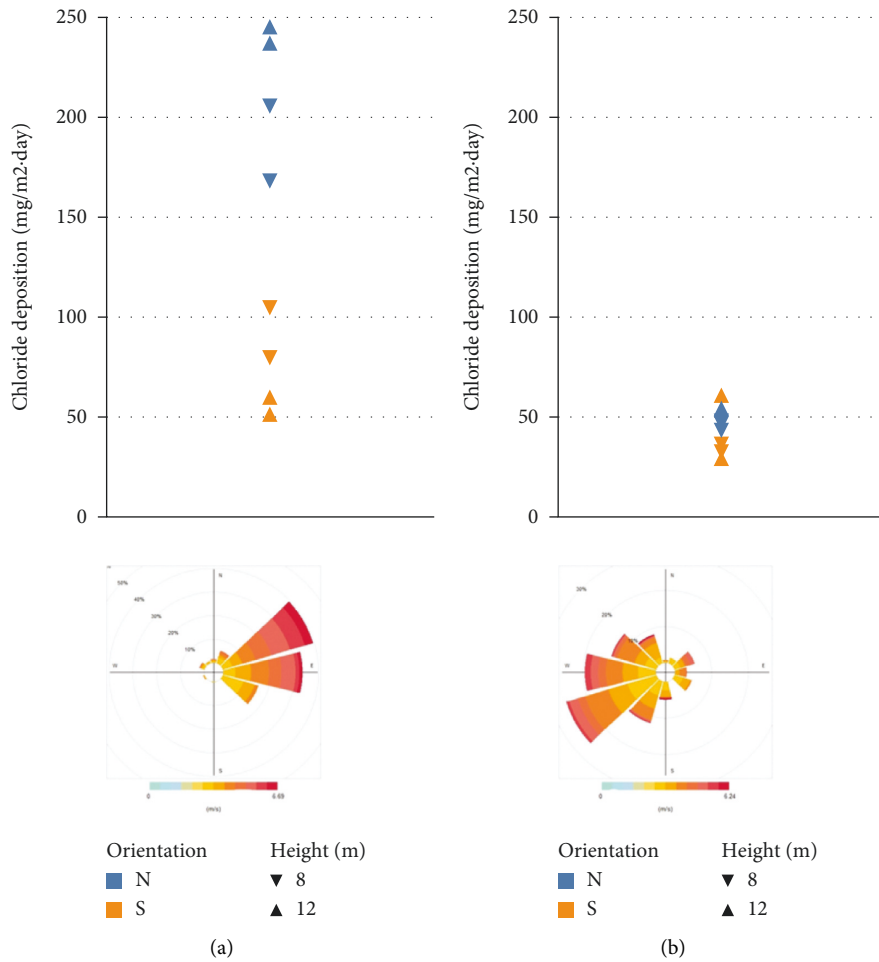
FIGURE 7: Results of the localized tests: first study period (a). Second study period (b).

FIGURE 8: Results of test II, representation of deposition at each study location.

3.2.2. Test II. Figure 8 presents a summary of the results from Test II. The size of the circle indicates the amount of sea salt deposited. The values obtained as a function of geographical location were logical. The closer to the coast, the higher the deposition [44, 46, 47]. In agreement with other studies, the deposited salt concentration decreased as it moved away from the ocean [48, 49] when there were no additional sources to replace these losses. However, there was a southern point that stood out owing to its value in addition to its remoteness from the sea. It should be noted that other less influential sources can generate chloride, e.g., biomass combustion [50], coal burning [35], or industrial fumes [51].

It would be interesting to analyze these data by considering the orientation of each sample at each site
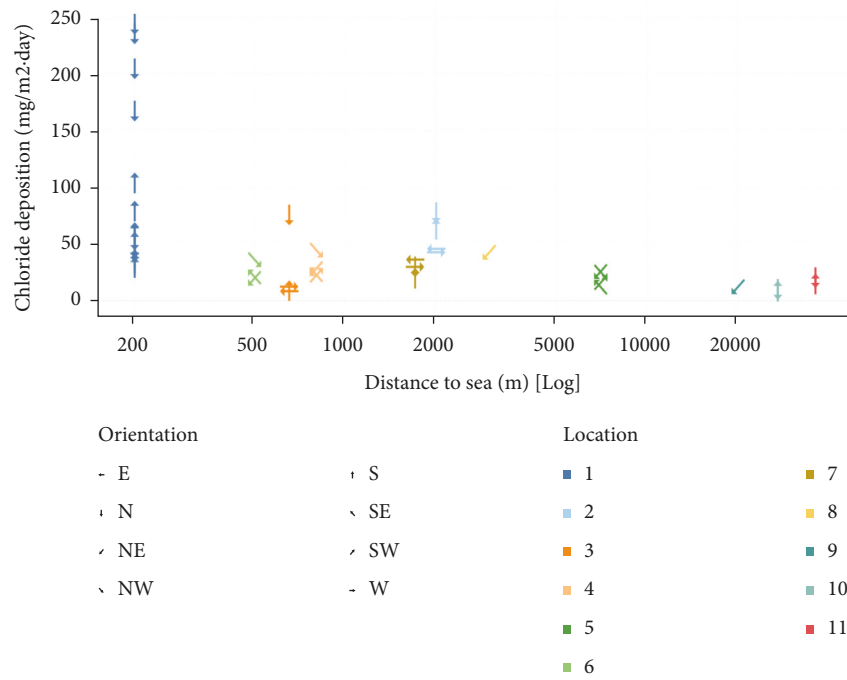
FIGURE 9: Chloride deposition as a function of distance from the sea in meters (logarithmic scale).
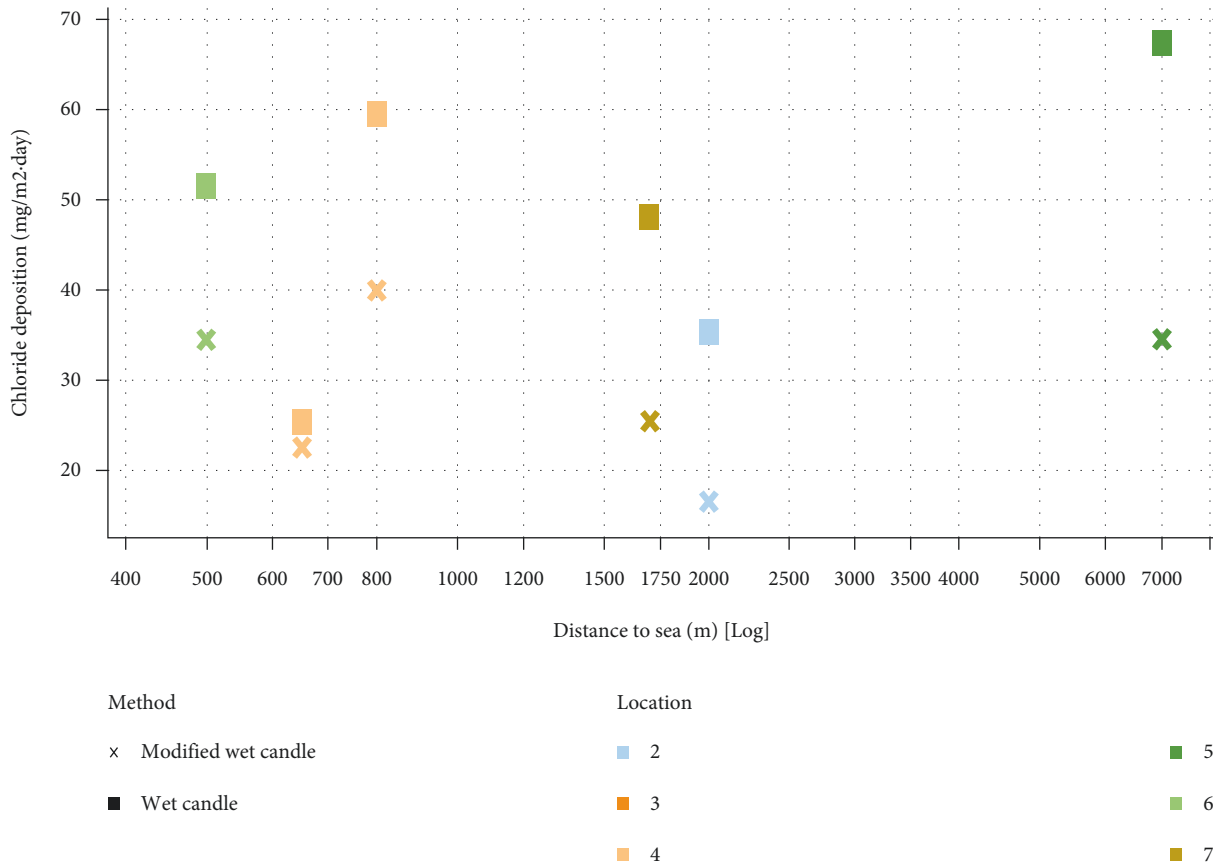
FIGURE 10: Representation of chloride deposition versus distance to coast in test III.

(Figure 9). All 11 locations were identified by both their color and equal distance to the sea. The results from test I (location 1) are also included in the graphic to gain a perspective. Thus, it is clear that the chloride content generally decreases as the distance increases. However, as each arrow indicates, there were significant differences between the orientations.

Relevant results were obtained when the values obtained during the second test were analyzed. First, it can be observed that chloride depositions are generally lower than those in test I, even considering the distance, probably because it was a period of much more rainfall than the previous one. This is in agreement with what Binyehmed et al. [35] found after analyzing the results of their experimental studies, which corroborated the increased chloride deposition rate in dry seasons compared to that in wet seasons. Besides, it can be observed that results can differ significantly depending on the orientation and origin of the wind, as demonstrated in test I. These differences in deposition became more remarkable with increasing proximity to the coast. More specifically, all the samples exposed to sea wind (coming from the north) had higher depositions than those from the other directions ($p < 0.01$), although these depositions progressively decreased in all cases as they moved away from the coast. Certainly, as the distance to the sea increased, the sensitivity of the orientation decreased.

3.2.3. Test III. The results of the final experiment are presented in Figure 10. This figure shows the deposition values versus distance from the shore. Each location is represented by a color; therefore, samples of the same color were subjected to the same meteorological conditions during the study period. However, the shape of the figure indicates the sampling techniques it represents.

The values obtained using the standard wet candle method were significantly higher than those of the modified counterpart ($p < 0.01$). These are the same study and meteorological conditions, except for the fact that the wet candle method is exposed to the wind and the covered candle method is not. Thus, the important role played by this variable is once again reflected, as stated in [36, 38], among other reports. It is risky to simplify the relationship between pollutant deposition and distance to the sea because the effectiveness of transportation or the existence of alternative sources may be important, as the results of location 5 demonstrated. The effect of blocking conditions on the final deposition result was studied in [41, 52, 53] but referred to as land cover.

The main source of these chloride ions is the ocean [41]. However, the distance to the ocean does not reflect exclusively the efficiency of chloride transport or the rate at which it falls or precipitates, among other effects; therefore, its parameterization varies from place to place [54]. Thus, this alternative technique may be used in cases such as those here studied, in which precipitation but no wind is present.

Atmospheric corrosion is a complex electrochemical process that involves many factors and variables [55]. The degradation suffered by the structures due to the action of chloride ions is clear [43, 56, 57] and it could be directly related to the protectiveness of the rust layers [58].

Therefore, to ensure sufficiently safe and useful life conditions, studying climatic variables, such as those proposed herein, can help identify potential damages [59]. The efficiency and complexity of airborne transportation are crucial for such processes [60]. In addition, it may be applicable and relevant to other important contaminants [61, 62].

4. Conclusions

Atmospheric corrosion in coastal environments has serious economic and environmental consequences owing to the degradation of structures, which forces the implementation of measures that have an impact on solution sustainability. SHM systems based on satellite information are an interesting alternative for monitoring remote locations. Studying and analyzing the most vulnerable zones of a structure prior to applying an SHM method may reduce the monitoring and modeling time and cost. This investigation focused on studying the deposition process of chloride contaminants as the most relevant factor for corrosion in coastal environments. Traditional approaches estimate chloride content only after direct measurement or by distance to the sea. Direct measurement is affected by the limitations of the current methods, which do not consider the effect of rainfall and relating it exclusively to distance to the sea involves serious errors. The results of the performed experimental tests based on meteorological sensor data, both localized and distributed, supported these ideas and allowed drawing the following main conclusions:

(i) The relative position between the orientation of the structure and the prevailing wind direction is a very important factor.

(ii) In addition to prevailing winds, it is of the utmost importance to consider the origin of that wind because when it comes from nonmarine areas, the transport and, therefore, the deposition of marine pollutants will be much lower.

(iii) Neither temperature nor relative humidity shows sufficiently large variations in the period and place of study to clarify its role in this phenomenon, although it is not possible to rule out their involvement.

(iv) The role of precipitation is also important, not only because it produces a washing effect and cleans the surfaces of contaminants, but also because, even when it does not act directly on the surface, it can reduce the chloride content in the environment, thus avoiding its transport and deposition by the wind. Precipitation periodicity is an important

variable. However, one of the main limitations observed during the tests was the difficulty in forecasting precipitation.

(v) The new covered candle deposition measurement method can separate the contributions made by the wind from those made by rain, which allows modeling the phenomenon in a much deeper way. Even with the new method, there are many limitations in the use of real data, as it lacks representativeness for having been collected over short periods of time.

(vi) The experimental test results show with sufficient statistical significance that the areas potentially most susceptible to corrosion can be identified using information from remote sensing satellites based on orientation, wind conditions, and wind origin.

In future research, it is proposed to quantify numerically the values of wind power or energy for each orientation and location studied. Thus, it will be possible to obtain the minimum wind threshold for the case study.

It is necessary to develop models that consider the orientation, velocity, and percentage distribution of the wind source to make a deposition model. With all these conditions, a model can be built that provides, without needing sensors, an accurate estimation of the corrosion at a given location. This can be used both for the diagnosis of existing structures and for the optimized design of new structures. This better prediction will improve the estimation of corrosion of structures exposed to weathering and, eventually, enable an optimization of structural design from the economic and environmental sustainability point of view.

Data Availability

The data used to support the findings of this study are available from the corresponding author upon request.

Conflicts of Interest

The authors declare no conflicts of interest regarding the publication of this paper.

Acknowledgments

References

[1] O. Avci, O. Abdeljaber, S. Kiranyaz, M. Hussein, M. Gabbouj, and D. J. Inman, "A review of vibration-based damage detection in civil structures: from traditional methods to Machine Learning and Deep Learning applications," *Mechanical Systems and Signal Processing*, vol. 147, Article ID 107077, 2021.

[2] F. Seguel and V. Meruane, "Damage assessment in a sandwich panel based on full-field vibration measurements," *Journal of Sound and Vibration*, vol. 417, pp. 1–18, 2018.

[3] "Deep learning and its applications to machine health monitoring," *Mechanical Systems and Signal Processing*, vol. 115, pp. 213–237, 2019.

[4] E. Ozer and M. Q. Feng, "Structural health monitoring," in *Start-Up Creation*, F. Pacheco-Torgal, E. Rasmussen, C.-G. Granqvist, V. Ivanov, A. Kaklauskas, and S. Makonin, Eds., pp. 345–367, Woodhead Publishing, Second Edition, 2020.

[5] R.-T. Wu and M. R. Jahanshahi, "Data fusion approaches for structural health monitoring and system identification: past, present, and future," *Structural Health Monitoring*, vol. 19, no. 2, pp. 552–586, 2020.

[6] M. Mishra, P. B. Lourenço, and G. V. Ramana, "Structural health monitoring of civil engineering structures by using the internet of things: a review," *Journal of Building Engineering*, vol. 48, Article ID 103954, 2022.

[7] C. H. Tan, F. R. Mahamd Adikan, Y. G. Shee, and B. K. Yap, "Nondestructive fiber Bragg grating based sensing system: early corrosion detection for structural health monitoring," *Sensors and Actuators A: Physical*, vol. 268, pp. 61–67, 2017.

[8] M. Abbas and M. Shafiee, "An overview of maintenance management strategies for corroded steel structures in extreme marine environments," *Marine Structures*, vol. 71, Article ID 102718, 2020.

[9] M. Wasim and M. B. Djukic, "External corrosion of oil and gas pipelines: a review of failure mechanisms and predictive preventions," *Journal of Natural Gas Science and Engineering*, vol. 100, Article ID 104467, 2022.

[10] D. Ziaja and P. Nazarko, "SHM system for anomaly detection of bolted joints in engineering structures," *Structures*, vol. 33, pp. 3877–3884, 2021.

[11] M. Gong, D. Ruth, M. Claire et al., "Adaptive smoothing to identify spatial structure in global lake ecological processes using satellite remote sensing data," *Spat. Stat.*, Article ID 100615, 2022.

[12] S. Das, P. Saha, and S. K. Patro, "Vibration-based damage detection techniques used for health monitoring of structures: a review," *Journal of Civil Structural Health Monitoring*, vol. 6, no. 3, pp. 477–507, 2016.

[13] M. Gordan, S. R. Sabbagh-Yazdi, Z. Ismail et al., "State-of-the-art review on advancements of data mining in structural health monitoring," *Measurement*, vol. 193, Article ID 110939, 2022.

[14] M. Meribout, S. Mekid, N. Kharoua, and L. Khezzar, "Online monitoring of structural materials integrity in process industry for I4.0: a focus on material loss through erosion and corrosion sensing," *Measurement*, vol. 176, Article ID 109110, 2021.

[15] F. J. Pallarés, M. Betti, G. Bartoli, and L. Pallarés, "Structural health monitoring (SHM) and Nondestructive testing (NDT) of slender masonry structures: a practical review," *Construction and Building Materials*, vol. 297, Article ID 123768, 2021.

[16] M. Hassan Daneshvar and H. Sarmadi, "Unsupervised learning-based damage assessment of full-scale civil structures under long-term and short-term monitoring," *Engineering Structures*, vol. 256, Article ID 114059, 2022.

[17] O. Avci, O. Abdeljaber, S. Kiranyaz, M. Hussein, and D. J. Inman, "Wireless and real-time structural damage detection: a novel decentralized method for wireless sensor networks," *Journal of Sound and Vibration*, vol. 424, pp. 158–172, 2018.

[18] F. N. Catbas, O. Celik, O. Avci, O. Abdeljaber, M. Gul, and N. T. Do, "Sensing and monitoring for stadium structures: a

review of recent advances and a forward look," *Front. Built Environ.*vol. 3, 2017.

[19] S. Lee and C. Lee, "Prediction of shear strength of FRP-reinforced concrete flexural members without stirrups using artificial neural networks," *Engineering Structures*, vol. 61, pp. 99–112, 2014.

[20] H. Salehi and R. Burgueño, "Emerging artificial intelligence methods in structural engineering," *Engineering Structures*, vol. 171, pp. 170–189, 2018.

[21] F. Shadan, F. Khoshnoudian, and A. Esfandiari, "A frequency response-based structural damage identification using model updating method," *Structural Control and Health Monitoring*, vol. 23, no. 2, pp. 286–302, 2016.

[22] M. H. Daneshvar, A. Gharighoran, S. A. Zareei, and A. Karamodin, "Early damage detection under massive data via innovative hybrid methods: application to a large-scale cable-stayed bridge," *Structure and Infrastructure Engineering*, vol. 17, no. 7, pp. 902–920, 2021.

[23] H. Sarmadi, A. Entezami, B. Saeedi Razavi, and K.-V. Yuen, "Ensemble learning-based structural health monitoring by Mahalanobis distance metrics," *Structural Control and Health Monitoring*, vol. 28, no. 2, Article ID e2663, 2021.

[24] A. Entezami, H. Shariatmadar, and S. Mariani, "Early damage assessment in large-scale structures by innovative statistical pattern recognition methods based on time series modeling and novelty detection," *Advances in Engineering Software*, vol. 150, Article ID 102923, 2020.

[25] M. H. Rafiei and H. Adeli, "A novel machine learning-based algorithm to detect damage in high-rise building structures," *The Structural Design of Tall and Special Buildings*, vol. 26, no. 18, Article ID e1400, 2017.

[26] L. Yan, Y. Diao, Z. Lang, and K. Gao, "Corrosion rate prediction and influencing factors evaluation of low-alloy steels in marine atmosphere using machine learning approach," *Science and Technology of Advanced Materials*, vol. 21, no. 1, pp. 359–370, 2020.

[27] E. Diler, F. Peltier, J. Becker, and D. Thierry, "Real-time corrosion monitoring of aluminium alloys under chloride-contaminated atmospheric conditions," *Materials and Corrosion*, vol. 72, no. 8, pp. 1377–1387, 2021.

[28] B. Santosh Kumar, S. A. Sannasiraj, and K. Murali, "Effect of climate change in the deterioration of a berthing structure in a tropical environment," *J. Inst. Eng. India Ser. A*, vol. 102, no. 3, pp. 697–703, 2021.

[29] N. Brett, "Why we should care about vulnerable coastal communities," 2019, https://ani.seafdec.org.ph/handle/20.500.12174/5473.

[30] W. Choi, D. Lee, and C. B. Bahn, "Quantitative analysis methods of chloride deposition on silver for atmospheric corrosion monitoring in South Korea," *Corrosion*, vol. 77, no. 1, pp. 53–61, 2021.

[31] N. Russo, M. Gastaldi, L. Schiavi, A. Strini, R. Zanoni, and F. Lollini, "78_Effect of cracks on the service life of RC structures exposed to chlorides," *Acta Polytech. CTU Proc.*vol. 33, pp. 511–517, 2022.

[32] ISO, "ISO/TC 156 Corrosion of metals and alloys, 'ISO 9225:2012 Corrosion of metals and alloys — corrosivity of atmospheres — measurement of environmental parameters affecting corrosivity of atmospheres," 2012, https://www.iso.org/.

[33] P. Haberecht, "Pollution Deposition Rates on Insulator (HV) Surfaces for Use in Atmospheric Corrosivity Estimation," University of Newcastle, Callaghan, Australia, Doctor of Philosophy, 2008.

[34] G. R. Meira, M. C. Andrade, I. J. Padaratz, M. C. Alonso, and J. C. Borba, "Measurements and modelling of marine salt transportation and deposition in a tropical region in Brazil," *Atmospheric Environment*, vol. 40, no. 29, pp. 5596–5607, 2006.

[35] F. M. Binyehmed, A. M. Abdullah, R. M. Zawawi, R. E. Elawad, and K. Youssef, "Deposition Rate of Chloride DRC as a Corrosive Agent in Several Locations in the Klang Valley, Malaysia," *Sci.Int.*vol. 29, no. 2, 2017.

[36] I. Díaz, H. Cano, P. Lopesino et al., "Five-year atmospheric corrosion of Cu, Cr and Ni weathering steels in a wide range of environments," *Corrosion Science*, vol. 141, pp. 146–157, 2018.

[37] A. W. Momber, S. Buchbach, P. Plagemann, and T. Marquardt, "Edge coverage of organic coatings and corrosion protection over edges under simulated ballast water tank conditions," *Progress in Organic Coatings*, vol. 108, pp. 90–92, 2017.

[38] T. Duan, W. Peng, K. Ding et al., "Long-term field exposure corrosion behavior investigation of 316L stainless steel in the deep sea environment," *Ocean Engineering*, vol. 189, Article ID 106405, 2019.

[39] G. R. Meira, W. T. A. Pinto, E. E. P. Lima, and C. Andrade, "Vertical distribution of marine aerosol salinity in a Brazilian coastal area – the influence of wind speed and the impact on chloride accumulation into concrete," *Construction and Building Materials*, vol. 135, pp. 287–296, 2017.

[40] J. Piazzola and S. Despiau, "Contribution of marine aerosols in the particle size distributions observed in Mediterranean coastal zone," *Atmospheric Environment*, vol. 31, no. 18, pp. 2991–3009, 1997.

[41] J. Liu, G. Ou, Q. Qiu, F. Xing, K. Tang, and J. Zeng, "Atmospheric chloride deposition in field concrete at coastal region," *Construction and Building Materials*, vol. 190, pp. 1015–1022, 2018.

[42] J. C. Guerra, A. Castañeda, F. Corvo, J. J. Howland, and J. Rodríguez, "Atmospheric corrosion of low carbon steel in a coastal zone of Ecuador: anomalous behavior of chloride deposition versus distance from the sea," *Materials and Corrosion*, vol. 70, no. 3, pp. 444–460, 2019.

[43] R. Wattanapornprom and T. Ishida, "Modeling of chloride penetration into concrete under airborne chloride environmental conditions combined with washout effects," *Journal of Advanced Concrete Technology*, vol. 15, no. 3, pp. 126–142, 2017.

[44] B. Liu, X. Mu, Y. Yang et al., "Effect of tin addition on corrosion behavior of a low-alloy steel in simulated costal-industrial atmosphere," *Journal of Materials Science & Technology*, vol. 35, no. 7, pp. 1228–1239, 2019.

[45] G. R. Meira, C. Andrade, I. J. Padaratz, C. Alonso, and J. C. Borba Jr., "Chloride penetration into concrete structures in the marine atmosphere zone - relationship between deposition of chlorides on the wet candle and chlorides accumulated into concrete," *Cement and Concrete Composites*, vol. 29, no. 9, pp. 667–676, 2007.

[46] D. de la Fuente, I. Díaz, J. Simancas, B. Chico, and M. Morcillo, "Long-term atmospheric corrosion of mild steel," *Corrosion Science*, vol. 53, no. 2, pp. 604–617, 2011.

[47] J. Alcántara, B. Chico, J. Simancas, I. Díaz, D. de la Fuente, and M. Morcillo, "An attempt to classify the morphologies presented by different rust phases formed during the exposure of carbon steel to marine atmospheres," *Materials Characterization*, vol. 118, pp. 65–78, 2016.

[48] M. E. R. Gustafsson and L. G. Franzén, "Dry deposition and concentration of marine aerosols in a coastal area, SW Sweden," *Atmospheric Environment*, vol. 30, no. 6, pp. 977–989, 1996.

[49] P. J. Davies and R. S. Crosbie, "Mapping the spatial distribution of chloride deposition across Australia," *Journal of Hydrology*, vol. 561, pp. 76–88, 2018.

[50] K. A. Pratt, S. M. Murphy, R. Subramanian et al., "Flight-based chemical characterization of biomass burning aerosols within two prescribed burn smoke plumes," *Atmospheric Chemistry and Physics*, vol. 11, no. 24, Article ID 12549, 2011.

[51] R. C. Moffet, B. de Foy, L. T. Molina, M. J. Molina, and K. A. Prather, "Measurement of ambient aerosols in northern Mexico City by single particle mass spectrometry," *Atmospheric Chemistry and Physics*, vol. 8, no. 16, pp. 4499–4516, 2008.

[52] K. Slamova, "Mapping Atmospheric Corrosion in Coastal Regions: Methods and Results," *Journal of Photonics for Energy*, vol. 2, no. 1, Article ID 022003, 2012.

[53] A. Castañeda, F. Corvo, J. J. Howland, and R. Marrero, "Penetration of marine aerosol in a tropical coastal city: Havana," *Atmósfera*, vol. 31, no. 1, pp. 87–104, 2018.

[54] H. Guan, A. J. Love, C. T. Simmons, O. Makhnin, and A. S. Kayaalp, "Factors influencing chloride deposition in a coastal hilly area and application to chloride deposition mapping," *Hydrology and Earth System Sciences*, vol. 14, no. 5, pp. 801–813, 2010.

[55] M. Kubzova, V. Krivy, and K. Kreislova, "Influence of chloride deposition on corrosion products," *Procedia Engineering*, vol. 192, pp. 504–509, 2017.

[56] S. Hu, Z. Wang, Y. Guo, and G. Xiao, "Life-cycle seismic fragility assessment of existing RC bridges subject to chloride-induced corrosion in marine environment," *Advances in Civil Engineering*, vol. 2021, Article ID e9640521, 18 pages, 2021.

[57] Y. Gu, A. Yu, and X. Zhang, "Seismic performance of offshore piers under wave impact and chloride ion corrosion environment," *Shock and Vibration*, vol. 2021, pp. 1–19, 2021.

[58] H. Chen, H. Cui, Z. He, L. Lu, and Y. Huang, "Influence of chloride deposition rate on rust layer protectiveness and corrosion severity of mild steel in tropical coastal atmosphere," *Materials Chemistry and Physics*, vol. 259, Article ID 123971, 2021.

[59] M. Ormellese, S. Beretta, T. Bellezze, and F. Bolzoni, "Atmospheric Corrosion Behavior of Zinc and Zinc Alloys: Comparison between Natural and Accelerated Exposure," 2021, https://onepetro.org/NACECORR/proceedings/CORR21/8-CORR21/D081S029R008/464011.

[60] R. Wattanapornprom, P. Limtong, T. Ishida, P. Pheinsusom, and W. Pansuk, "Airborne chloride intensity and chloride ion penetration into mortar specimen in Thailand," *Engineering Journal*, vol. 24, no. 2, pp. 87–100, 2020.

[61] M. H. Nazir, A. Saeed, and Z. Khan, "A comprehensive predictive corrosion model incorporating varying environmental gas pollutants applied to wider steel applications," *Materials Chemistry and Physics*, vol. 193, pp. 19–34, 2017.

[62] G. Battista, "Analysis of the air pollution sources in the city of rome (Italy)," *Energy Procedia*, vol. 126, pp. 392–397, 2017.

Research Article

Research on the Anti-Leakage System for Reinforced Concrete Flat Roofs in Cold Areas

Li Lin [ID],[1,2] Xin Yuan [ID],[1] Pengxiao Tang,[1] Xun Wang,[1] and Tianli Xu[2]

[1]*College of Architecture Engineering, Harbin University of Science and Technology, Harbin 150080, China*
[2]*School of Civil Engineering, Harbin Institute of Technology, Harbin 150090, China*

Correspondence should be addressed to Li Lin; linli0119@163.com

To solve the persistent problem of roof leakage in cold areas, a reinforced concrete flat roof anti-leakage prevention system was proposed in this study, and the leakage prevention of this roof system in the cold areas was investigated by conducting a scaled-down model outdoor exposure test. In addition, the weather in the Harbin area during the freeze-thaw cycle season was predicted by the support vector machine (SVM) model in machine learning, based on which ABAQUS finite element analysis of the roof system was carried out to reveal the leakage prevention mechanism of the system. The research results show that improving the roof level temperature during the freeze-thaw cycle can reduce the influence of temperature stresses brought by the freeze-thaw cycle, slow down the development of cracks inside the roof, reduce the probability of roof leakage, and can provide a new idea for solving the roof leakage problem in a cold area.

1. Introduction

China is a vast country with a wide distribution of cold regions, and water seepage in cold roofs has been a persistent problem [1]. To solve the problem of roof leakage, civil engineering workers, experts, and scholars have put forward many constructive ideas and solutions. In addition to conventional measures such as filling the roof with waterproofing materials and reconstructing the aging waterproofing layer, measures such as adding waterproofing layers to parts prone to leakage and using new materials with better waterproofing performance and greater durability are also widely used in roofing construction [2]. In the 1990s, Wu et al. [3] proposed the structural design of a pull-avoidance inverted waterproof roof. Bao et al. [4] adopted a pull-avoidance inverted roof structure and used gas barriers with a high vapor permeability resistance and thermal insulation materials with poor water absorption. Xu et al. [5] introduced new materials and technologies for roof construction in cold areas. Zhou et al. [6] discussed the causes of roof leakage in cold areas and provided several preventive measures. Lin and Li [7] put forward the practice of an anti-leakage drainage system for roofs in cold areas, which effectively reduced the influence of temperature stress on the roof system and improved the durability of roofs. Dong [8] proposed several construction options for separating the rigid surface layer from the asphalt waterproofing layer. Qu [9] found that the causes of cracking in the waterproofing layer can be attributed mainly to the deformation of the indirect joints in the prefabricated roof panels and the improper handling of the roof expansion joints. Zhao [10] proposed the installation of electric heating devices in roof drainage systems for buildings in cold regions.

Freeze-thaw cycles are one of the main causes of leakage in concrete roofs in cold areas. It can result in reduced performance of reinforced concrete, such as concrete strength decreases internal structural changes and tracking [11]. Since 1940, many scholars have studied the mechanism of freeze-thaw damage to the concrete from multiple angles and in all directions, conducting a large number of tests and drawing many valuable conclusions. Shang [12] performed bidirectional compressive stress tests on plain concrete specimens after 0, 25, 50, and 75 freeze-thaw cycles. Hasan [13], Penttala [14], and other scholars such as Sicat [15]

studied the stress-strain relationship in concrete during freeze-thaw cycles. The destruction mechanism of concrete under repeated freeze-thaw cycle was summarized; typical research could be found in Zhang et al. [16] Tian and Zhang [17], Chen and Cui [18], and Liang et al. [19].

To sum up, existing research has mainly focused on adding a waterproofing layer to the parts prone to leakage or using new materials with better waterproofing properties; however, this method ignores the impact of freeze-thaw cycles on the roof leakage in cold regions and can only solve surface problems, making it difficult to completely eradicate the leakage phenomenon.

In this study, the anti-leakage system of reinforced concrete flat roofs in cold areas is proposed, which is different from the traditional leakage prevention structure, and it can resist the freeze-thaw cycle by raising the roof temperature, improving the durability of concrete, and solving the problem of roof leakage. In addition to outdoor exposure tested on the scaled-down model of reinforced concrete roof leakage prevention system in cold regions, the freeze-thaw cycle occurrence time and temperature were predicted by the support vector machine (SVM) [20–22], and ABAQUS finite element simulations were performed on the roof system based on the prediction results to study the roof leakage prevention performance.

2. Design of an Anti-Leakage System for Reinforced Concrete Flat Roofs

In actual engineering, a roof panel without measures against freeze-thaw cycles will produce cracks that continue to grow, causing a large-area leakage. The key to solving the problem of roof leakage in cold areas is to reduce the stress generated by the roof panels during the freeze-thaw cycle. Therefore, this study proposes an anti-leakage system for reinforced concrete flat roofs constructed in cold areas. The system comprises three parts: the main body of the roof system, a heating system, and a drainage system, as shown in Figure 1.

The design idea is to add a heating system to the main body of the roof system, utilize the heat radiation effect of the heating system to increase the overall temperature of the roof, prevent the roof from freezing, reduce the stress generated by the roof in the freeze-thaw cycle, and establish a drainage system to facilitate the rapid discharge of the roof snow after melting; the three parts of the system together can help resist freeze-thaw cycles. The main body of the roof system comprises a load-bearing roof slab, a pre-buried pipeline insulation layer, a slope layer, a leveling layer, a waterproof layer, and a protective layer, as shown in Figure 2. The main body of the roof system uses multiple water dividers to make the longitudinal section of the roof in the shape of a folded plate while maintaining a drainage slope ranging from 2% to 5%, and water outlets are evenly arranged between adjacent roof ridges to facilitate the rapid collection of water on the roof, thus completing the optimization of the drainage of the roof panels. The roof heating system comprises a circulating water supply system, a heating branch pipe pre-buried in the roof, a water supply main pipe, a water return main pipe, and a water stop valve. The roof drainage system is arranged horizontally
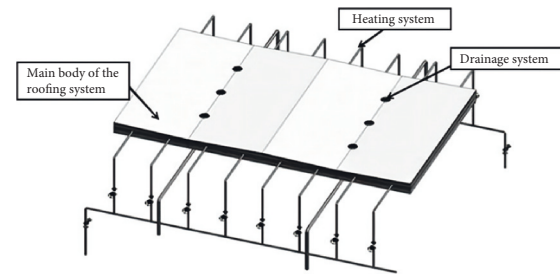
Figure 1: Overall diagram of the anti-leakage system of reinforced concrete flat roofs constructed in cold regions.
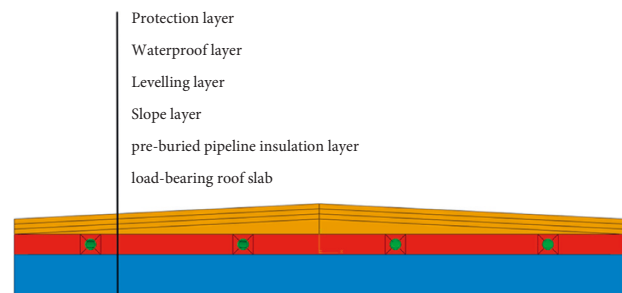
Figure 2: Schematic of the main roof system.

along the building using suspension pipes parallel to the ridgeline, and the suspension pipe branches are connected to the roof drop inlets.

When a freeze-thaw cycle occurs, the heating system is switched on, so that the thermal medium in the roof insulation layer carries out thermal radiation to raise the overall temperature of the roof system. The snow on the roof is heated and melted, and it flows into the roof dropout to be discharged through the drainage pipe to reduce the accumulation of water on the roof and prevent roof cracks when the solid-liquid conversion of water aggravates the roof. Thus, the problem of roof leakage in cold areas is solved.

3. Outdoor Exposure Test for Reinforced Concrete Flat Roof Scaled-Down Models

The most direct way to verify the ability of an anti-leakage system for reinforced concrete flat roofs to resist freeze-thaw cycles is to place the roof system in a freeze-thaw cycle environment and observe its insulation capacity and temperature field distribution in a natural low-temperature environment. By collecting the temperature information of the roof under the natural environment exposure, the performance of the roof system to resist freeze-thaw cycles in the natural environment is analyzed. The test is based on the provision of the national standard specification "Standard for testing methods of long-term performance and durability of ordinary concrete" (GB/T50082-2009) [23], concerning the slow freezing method test method.

3.1. Test Program. A scaled-down model of the reinforced concrete flat roof system was made and connected to the heating system. Four measurement points were arranged at

different locations on the scaled-down model from the heating pipes to measure the temperature changes. An ambient temperature group was added as a control group to study the influence of the heating system on the overall temperature of the roof system and to verify the insulation capacity of the roof system and its resistance to freeze-thaw cycles. Figure 3 shows the measurement point layout.

The scaled-down model was placed in an outdoor environment, and the test was started by energizing the CNC pump and electric heating rod to work the heating system. The test time was 12 h, and the test data were recorded using a THTE multiplex PID temperature controller.

3.2. Model Production and Test Preparation. The main materials used to prepare a scaled-down model of a reinforced concrete flat roof impermeability system were C30 concrete, 1 : 8 cement perlite material, 1 : 2.5 ordinary silicate cement mortar, 3 mm thick SBS-modified bitumen waterproofing membrane waterproofing layer, and cast iron pipes with an internal diameter of 19 mm and an external diameter of 22 mm. Among them, the size of the coarse concrete aggregate was in the range of 5–40 mm, and the cement, river sand, and coarse aggregate required in the preparation process were collected from Heilongjiang Province. The mixing water used was tap water.

After completing the material preparation for modeling, the structural floor slab formwork was first erected to ensure that the structural floor slab size was 1200 mm × 400 mm×80 mm. After the formwork was fixed, C30 concrete was poured and vibrated, and water was poured after 12 h for maintenance. After 14 days of maintenance, the formwork for the predetermined cast iron pipe holes was erected on the concrete slab, the cast iron pipe with an internal diameter of 19 mm and an external diameter of 22 mm was buried in the designed position, and the concrete was poured again to complete the construction of the insulation layer. Thereafter, a slope of 3% was laid on the insulation layer, 1 : 8 cement perlite material was laid from both sides of the roof towards the center, the slab was vibrated and paved, and the surface was scraped with a scraping bar and smoothed with a trowel. The slope layer on the paving material was 1 : 2.5 ordinary silicate cement mortar leveling layer, paving after maintenance for seven days. Finally, a 3mm thick self-adhesive SBS modified bitumen waterproofing roll-roofing membrane was laid, and and water storage test was carried out on the waterproof layer 24h after completion of laying, to confirm that there was no leakage on the roof, and then the protective layer was poured and maintained; the complete production of reinforced concrete flat roof antileakage system scaled-down model is shown in Figure 4.

Finally, the scaled model was connected to a water tank, CNC water pump, and water supply pipe; in turn, electric heating rods were placed in the water tank, Pt100 type RTDs were glued at the measurement points of the scaled model, and resistors were connected to the THTE multi-way PID temperature controller for temperature data recording. This completed the connection between the scaled model and the heating system and the arrangement of the data acquisition device. Figure 5 shows the overall layout of the outdoor exposure test of the scaled-down model of the reinforced concrete flat roof leakage prevention system.

3.3. Test Results. At the end of the test, the data recorded by the temperature controller were exported, and the time-temperature curve for each measurement point was obtained by processing the test data, as shown in Figure 6. The overall temperature increase in the roof system was significant; with the change in the ambient temperature, the overall temperature at the four measurement points increased to different degrees, but the overall temperature at the four measurement points of the roof still had a significant difference. The temperature was highest at measurement point 1, followed by measurement point 4, measurement point 3, and lastly measurement point 2. The temperature curves at the four measurement points also had different fluctuations. The curve for measurement point 1 was the smoothest, and fluctuations were the lowest; the fluctuations in the curve for measurement point 2 were the highest, and the fluctuations in the curves for measurement points 3 and 4 were in between. Furthermore, the initial temperature at measurement point 1 was −16°C, slightly above the initial ambient temperature of −18°C, while the other three measurement points were at the same temperature as the ambient temperature. The reason for the different temperature variations at each measurement point is that point 1 was located in the insulation layer, closest to the heating line. Therefore, it had a higher initial temperature than the ambient temperature and the highest overall temperature and was less susceptible to changes in the ambient temperature, with the lowest fluctuations in the temperature profile. Point 2 was located at the corner of the roof, the furthest from the heating line; it exhibited the lowest overall temperature, was most influenced by the ambient temperature, and had the most fluctuating curve. Point 3 was located on the ridge and had a lower overall temperature, but due to the heating lines on both sides, point 3 was less affected by the ambient temperature than point 2 and had a higher overall temperature than point 2. Point 4 was not in the insulation layer, but the distance from the heating pipeline was second only to point 1; therefore, the overall temperature was less than that at point 1 and higher than those at points 2 and 3.

Under the continuous application of the temperature field by the heating system, the overall temperature of the roof system increased more evidently, which effectively reduced the temperature stress due to the fluctuation of the roof system in practice and decreased the probability of leakage of the roof system under the freeze-thaw cycle. This proves the effectiveness of the proposed leakage prevention system for reinforced concrete flat roofs in cold areas.

4. Numerical Analysis

The numerical analysis of freeze-thaw cycles of reinforced concrete flat roof systems in cold regions requires the collection of corresponding weather data, which are entered
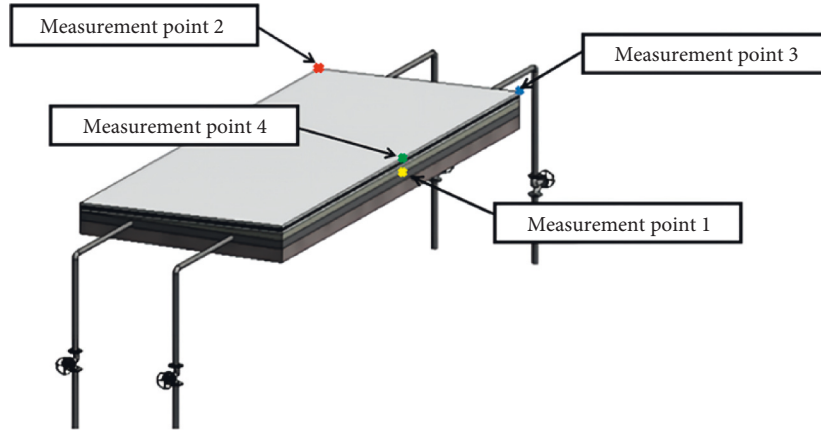
FIGURE 3: Temperature measurement point layout.

FIGURE 4: Scaled-down model of the anti-leakage system for reinforced concrete flat roofs.

FIGURE 5: Overall layout of an outdoor exposure test.

into the numerical analysis model as a temperature boundary condition; however, the outdoor collection has disadvantages such as long lead time and instability. Therefore, based on the weather information of Harbin during the freeze-thaw cycle-prone seasons of March and November, this study combines the SVM model of machine learning [24].

4.1. SVM Algorithm Prediction Model. SVM models have supervised learning models associated with relevant learning algorithms and are mainly used to analyze data, identify patterns, and perform classification and regression analysis studies. SVM maps the sample space to a high or even infinite-dimensional feature space through nonlinear mapping, in which a linear learning machine approach is applied to solve problems such as the highly nonlinear classification and regression in the sample space. In the SVM model, the generalized error is determined by three parameters, namely the cost parameter (E), the tolerance parameter (ε), and the kernel parameter (γ), and the values of these three parameters are not unique. Referring to Cherkassky and Ma [25], the SVM model parameters are

determined according to equations (1)–(5); Table 1 presents the model parameters. The correlation coefficient R indicates the degree of correlation between the estimated and true values, and the higher the correlation coefficient R, the better the correlation.

$$E = \max\left(\left|\overline{y} + 3\sigma_y\right|, \left|\overline{y} - 3\sigma_y\right|\right), \tag{1}$$

where $\overline{y}$ and σ_y are the mean and standard deviation of the training data Y values, respectively, expressed as follows:

$$\gamma = \frac{1}{2\rho^2}, \tag{2}$$

$$\rho = m\sqrt[k]{0.3}, \tag{3}$$

$$\varepsilon = 3\sigma\sqrt{\frac{\ln n}{n}}, \tag{4}$$

$$\delta = y_i - f(x_i), \tag{5}$$
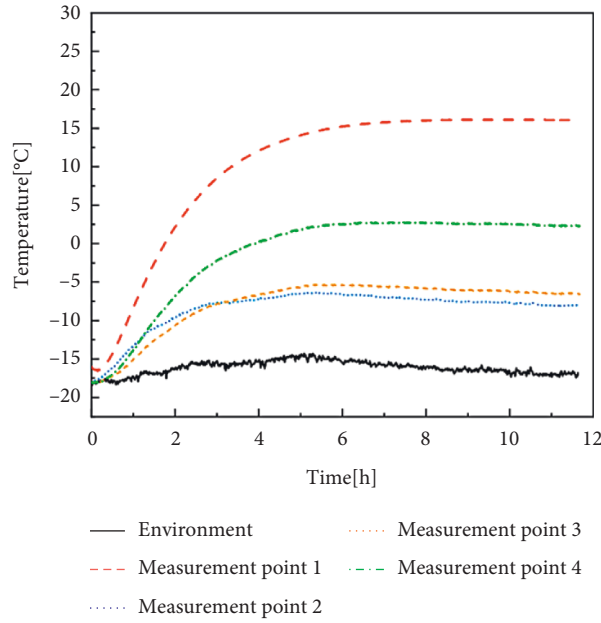
FIGURE 6: Time-temperature curves of each measurement point in the outdoor exposure test.

TABLE 1: Parameters of the SVM model.

Object	E	ε	γ	Mean absolute error	Mean squared error	R
Minimum air temperature	5.4796	0.1499	0.1174	0.5754	0.5133	0.7786
Maximum air temperature	6.7112	0.1378	0.1184	0.4478	0.4208	0.8432

where k is the number of output variables, m is the range of input values, σ is the difference between the true and predicted values, n is the number of values y, and δ is the standard deviation of the residuals.

Figure 7 shows the predicted maximum and minimum temperatures for the freeze-thaw cycle season in the Harbin area, where the serial number represents the weather number for the freeze-thaw cycle season, and the maximum and minimum temperatures represent the predicted values for the maximum and minimum temperatures for the day. The square set of dots in the graph is the simulated maximum temperature of the day in Harbin. The magnitude of the value increases with the serial number and then decreases, and the rate of increase is small at first, gradually increases with the serial number, increases rapidly after the serial number reaches 10, reaching the highest value at serial number 37, and then gradually decreases. The set of circles in the graph is the predicted minimum temperature for the day. The trend in the minimum temperature for the day is similar to that for the maximum temperature, both increasing and then decreasing. At the same time, between serial numbers 16–24 and 38–56, the highest temperature of the day is greater than 0°C, and the lowest temperature of the day is less than 0°C; therefore, the time interval in which the freeze-thaw cycling effect should occur must be between the two intervals of serial numbers 16–24 and 38–56. The temperature data within this time interval are extracted to obtain the SVM prediction of the temperature amplitude in which the freeze-thaw cycling effect may occur, as shown in Figure 8.
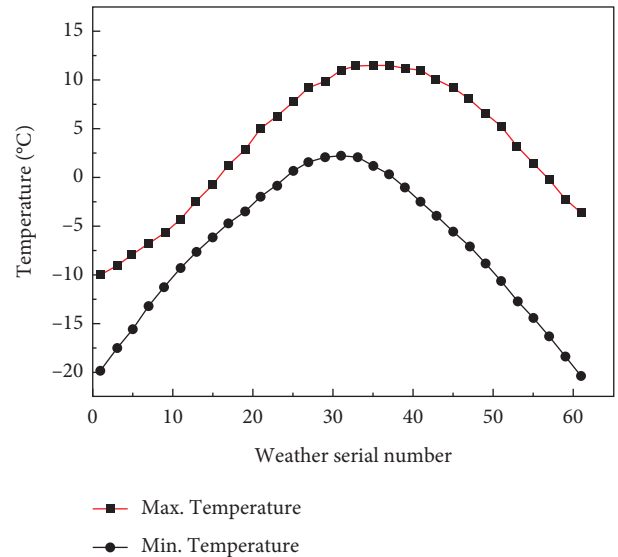
FIGURE 7: SVM predicts the daily maximum and minimum temperatures.

4.2. Establishment of the Numerical Analysis Model. The finite element analysis software ABAQUS was used to establish a numerical analysis model of the flat roof leakage prevention system for reinforced concrete in cold zones. The finite element model components include a structural floor slab, an insulation layer, pre-buried pipelines, and an upper maintenance structure, assembling each component to form
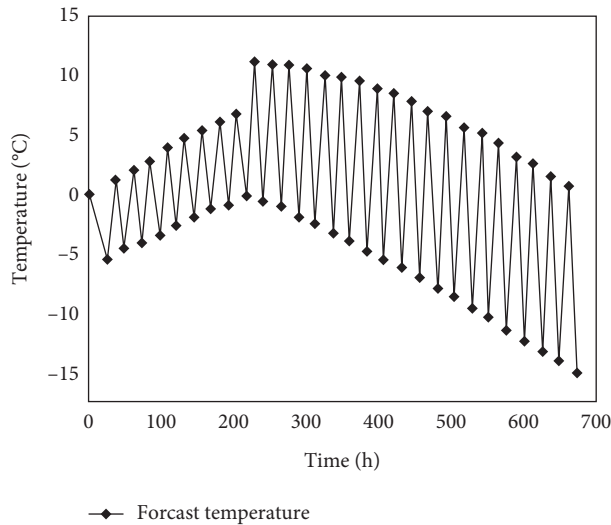
FIGURE 8: SVM predicts the temperature amplitude at which freeze-thaw cycles may occur.

a complete roof body model. Figure 9 shows the analytical model.

The numerical simulation was divided into two parts: a heat transfer analysis and static analysis. A given temperature amplitude was inputted into the analysis model for the heat transfer analysis, and the temperature field obtained from the heat transfer analysis was then imported into the experience analysis as a prestress field, resulting in the temperature stress distribution. The C3D8R and C3D20R units were used for the heat transfer and static analyses of the main roof components, respectively. The concrete material parameters were defined in terms of the density, thermal conductivity, and specific heat capacity for the heat transfer analysis and in terms of the modulus of elasticity, coefficient of linear expansion, and concrete damage for the static analysis. During the static analysis, only three parameters, namely the density, thermal conductivity, and specific heat capacity, were defined for the upper maintenance structure materials, namely the cement perlite, cement mortar, waterproof membrane, and cast iron, as the stress changes in the upper envelope had a small impact on the crack development condition of the roof body. Tables 2 and 3 present the model material parameters. In the actual project, the roof body parts work together. Therefore, the model components are bound to each other and considered as a whole. A hinge restraint is applied to the bottom of the roof body to ensure that the bottom slab of the roof body is not displaced.

*4.3. Numerical Analysis in the SVM Prediction.* Four test points were arranged in the model, corresponding to the outdoor exposure test points of the scaled model, as shown in Figure 10.

The SVM-predicted temperature amplitude of the possible freeze-thaw cycles as a boundary condition was inputted into the model for the heat transfer analysis, and the temperature change curves at each measurement point under the SVM-predicted environment were obtained, as

shown in Figure 11. The temperature at all the measurement points on the roof under the freeze-thaw cycle first increases and then decreases, while the temperature change law at each measurement point is consistent with the temperature change law at each measurement point in the outdoor exposure test. The overall temperature at measurement point 1 is the highest, and the temperature fluctuation is the smallest; the overall temperature at measurement point 2 is the lowest, and the temperature fluctuation is the highest; the temperature at measurement points 3 and 4 is between those at measurement points 1 and 2; however, the overall temperature at measurement point 4 is higher than that at the measurement point 3. In addition, the temperatures at all the four measurement points were above 0°C by 576 h. Among these, all the parts of the temperature, including the temperature of the low-temperature zone, which is widely distributed on the roof, were always above 0°C, except at measurement point 2, which is at the edge of the roof system, where the temperature decreased below 0°C. This proves the insulation capacity of the reinforced concrete flat roof leakage prevention system in cold regions in a freeze-thaw cycle environment.

The temperature field obtained from the heat transfer analysis was introduced into the static analysis step as a prestress field. Three measurement points were arranged, and the temperature stress distribution of the roof system was analyzed to obtain a temperature stress cloud for the main body of the roof, as shown in Figure 12. There is significant temperature stress in the main body of the roof concrete under the effect of freeze-thaw cycles. The deformation of the main body of the roof is influenced by the hinge restraint at the bottom surface, which is in the shape of a narrow prism at the bottom and a wide prism at the top, with a significant stress concentration at the bottom corners, reaching a maximum of approximately 24.54 MPa. The temperature stress distribution in the main concrete of the roof is generally decreasing from bottom to top, and there is a certain stress concentration in the pre-buried heating pipes.

The stress variation curves at the three measurement points of the roof are extracted and shown in Figure 13. After experiencing sequential temperature stress coupling, the temperature stresses at measurement points 2 and 3 tend to fluctuate, with the maximum values reaching 6.53 and 4.85 MPa, respectively. The stress at measurement point 1 tends to rise and then level off, with a small variation and a maximum value of approximately 0.53 MPa. Due to the large temperature variations at measurement points 2 and 3, greater temperature stress is generated in the static analysis relative to that at measurement point 1, while measurement point 1 has a smaller temperature variation, and its temperature stress grows more gradually during the freeze-thaw cycle. After a predicted freeze-thaw cycle, the overall temperature stress on the roof system is low, and the concrete in the roof system is in the elastic strain phase except for the hinged position. The reinforced concrete flat roof leakage prevention system in the cold zone can control the temperature stress at a low level and improve the leakage resistance of the concrete.
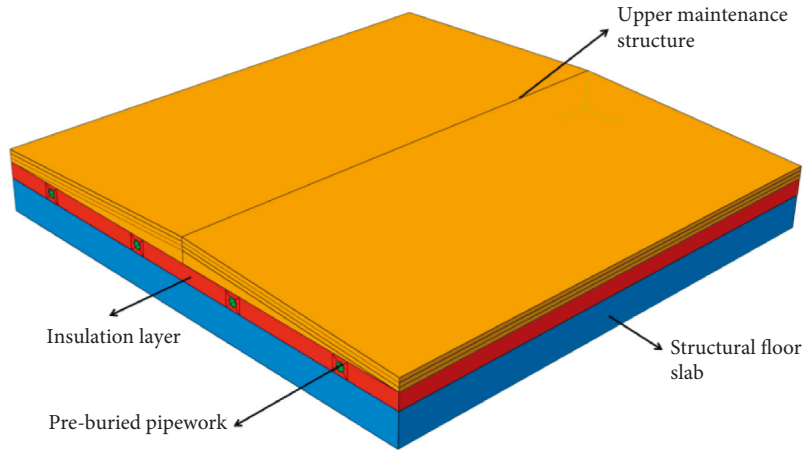
Figure 9: Analysis model.

Table 2: Material thermodynamic parameters.

Material	Thermal conductivity/(W/(m·K))	Specific heat capacity/(J/(kg°C))	Density/(kg/m^3)	Modulus of elasticity/(MPa)	Linear expansion coefficient/(m/°C)
C30 concrete	1.74	0.92	2500	30000	8×10^{-6}
Cement pearl rock	0.21	1.17	600	—	—
Cement mortar	0.93	1.05	1800	—	—
Waterproofing roll roofing	0.17	1.47	600	—	—
Iron casting	49.9	0.48	7250	—	—

Table 3: Concrete plastic damage parameter.

Material	Expansion angle	Poisson's ratio	Coefficient of viscosity	Eccentricity	K	f_{c0}/f_{b0}
C30 concrete	30	0.2	0.005	0.1	0.667	1.16
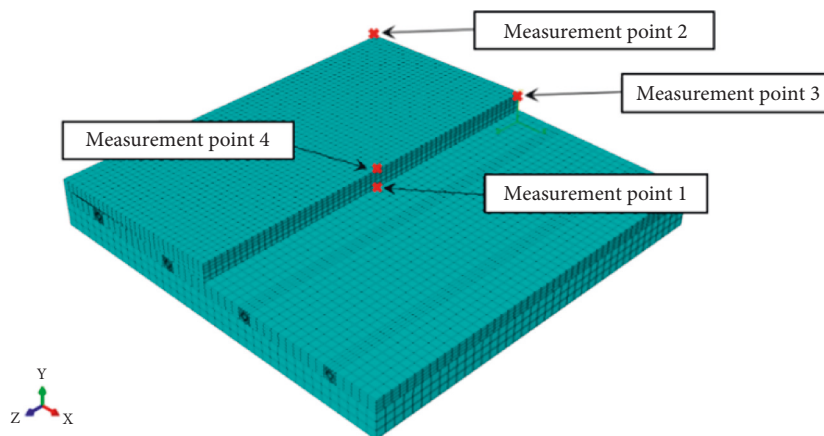
Figure 10: Layout of temperature measuring points in the numerical model.
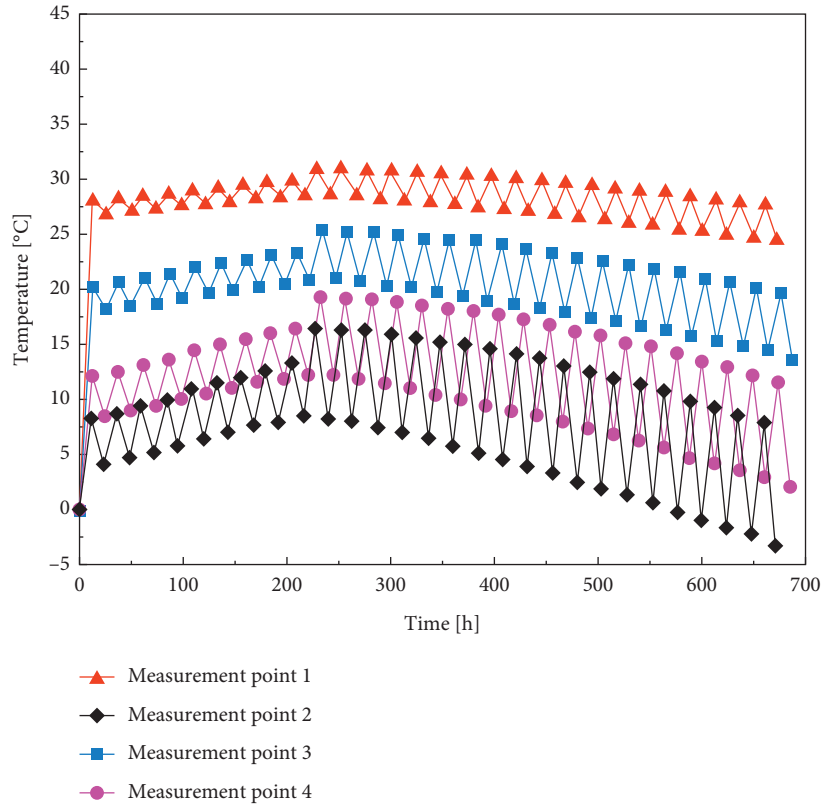
FIGURE 11: SVM predicts the temperature at each measuring point in the SVM-predicted environment.
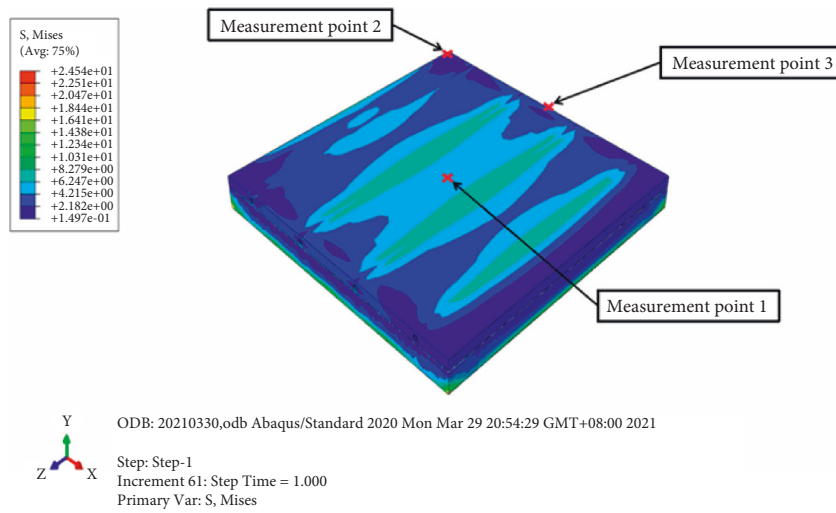
FIGURE 12: Temperature stress cloud.
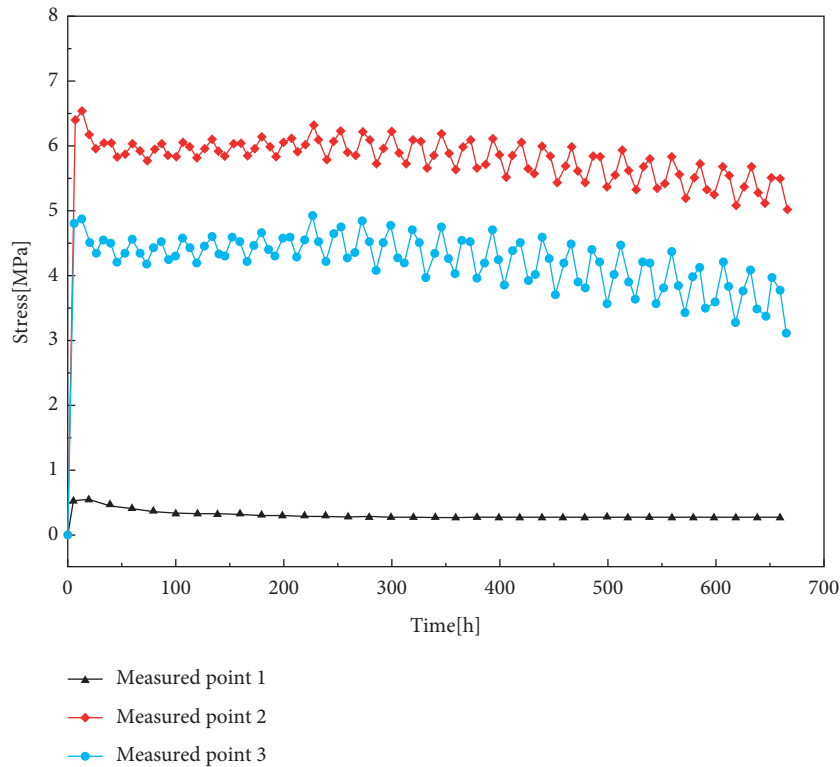
FIGURE 13: Time-temperature stress curve.

5. Conclusions

This study developed an anti-leakage system for reinforced concrete flat roofs constructed in cold regions and prepared a scaled-down model for outdoor exposure tests to verify the resistance of the system to freeze-thaw cycles. A weather prediction model based on the machine learning SVM algorithm was established, and a numerical analysis model of the freeze-thaw cycle of a flat roof leakage prevention system for reinforced concrete in cold zones was built on this basis. The response of the proposed leakage prevention system under the effect of the freeze-thaw cycle was numerically analyzed to reveal the leakage prevention mechanism of the system. The main results and conclusions are as follows:

(1) The working principle of leakage prevention system for reinforced concrete flat roofs in cold areas is to add a heating system to the main roof system, utilize the heat radiation effect of the heating system to increase the overall temperature of the roof, prevent the freezing of rainwater on the roof, and reduce the stress generated by the freeze-thaw cycle. The drainage system is also installed to facilitate the rapid discharge of snow water after melting.

(2) The roof system has good thermal insulation performance after adding the heating system; the temperature at all locations on the roof increased under the continuous application of the temperature field of the heating system, effectively resisting the freeze-thaw cycle, proving that the system designed has good resistance to freeze-thaw cycles.

(3) The SVM model predicted that freeze-thaw cycles are likely to occur on 26 days during the freeze-thaw cycle-prone season in Harbin, and the maximum temperature amplitude of the freeze-thaw cycle during this period is 18°C.

(4) The ABAQUS finite element simulation of the roof system based on the prediction of the SVM model found that the roof heating system could effectively reduce the effect of temperature stress caused by the freeze-thaw cycle, delay the development of internal cracks in the roof, and reduce the occurrence of roof leakage. It verified the impermeability of the roof system under the effect of the freeze-thaw cycle.

Data Availability

The data used to support the findings of this study are included within the article.

Conflicts of Interest

The authors declare that they have no conflicts of interest.

Acknowledgments

References

[1] Z. Wen, "Analysis of the causes of building roof leakage and research on anti-seepage disposal measures," *Green Environmental Protection Building Materials*, vol. 11, pp. 141-142, 2020, in Chinese.

[2] J. Gui, J. Gu, and X. Zhou, "Roof anti-seepage control technique of new waterproof and heat insulation material," *Architectural Technology*, vol. 46, no. 07, pp. 629–632, 2015, in Chinese.

[3] P. Wu and G. Zhang, "Pull-avoidance inverted roof is used in cold areas," *Low Temperature Architecture Technology"*, vol. 3, pp. 24-25, 1995, in Chinese.

[4] P. Bao and X. Bai, "Problems and countermeasures in the existing roofing structure in cold areas," *Anhui Architecture*, vol. 3, pp. 55-56, 1998, in Chinese.

[5] A. Xu and Y. Chen, "Application of thermal insulation and energy saving technology for building roof in cold area," *Heilongjiang Hydraulic Science and Technology*, vol. 1, pp. 118-119, 2004, in Chinese.

[6] Q. Zhou, "Discussion on the causes and control measures of roof leakage in cold areas," *Heilongjiang Science and Technology Information*, vol. 4204 pages, 2007, in Chinese.

[7] J. Li, *Some Problems about Transfer Story Buildings in Cold Regions Based on BIM*, Harbin University of Science and Technology, Harbin, China, 2018, in Chinese.

[8] C. Dong and S. Cui, "Exploring the design of upstander roofing structures in cold areas," *Architectural Technology*, vol. 10, pp. 611-612, 1993, in Chinese.

[9] F. Qu, B. Zhang, and S. Xu, "Exploration of crack leakage in roof waterproofing projects in cold areas," *Low Temperature Architecture Technology*, vol. 041999, in Chinese.

[10] S. Zhao and W. Wang, "Research on frost protection technology for large roof drainage systems in cold regions," *Construction Science and Technology*, vol. 23, pp. 94-95, 2014, in Chinese.

[11] R. Guo and H. Shang, "Bond behaviour of reinforced recycled concrete after rapid freezing thawing cycles," *Cold Regions Science and Technology*, vol. 157, pp. 133–138, 2018.

[12] H. S. Shang and Y. P. Song, "Experimental study of strength and deformation of plain concrete under biaxial compression after freezing and thawing cycles," *Cement and Concrete Research*, vol. 36, no. 10, pp. 1857–1864, 2006.

[13] M. Hasan, T. Ueda, and Y. Sato, "Stress-strain relationship of frost-damaged concrete subjected to fatigue loading," *Journal of Materials in Civil Engineering*, vol. 20, no. 1, pp. 37–45, 2008.

[14] V. Penttala and F. A. Neshawy, "Stress and strain state of concrete during freezing and thawing cycles," *Cement and Concrete Research*, vol. 32, no. 9, pp. 1407–1420, 2002.

[15] E. Sicat, F. Gong, T. Ueda, and D. Zhang, "Experimental investigation of the deformational behavior of the interfacial transition zone (ITZ) in concrete during freezing and thawing cycles," *Construction and Building Materials*, vol. 65, pp. 122–131, 2014.

[16] S. Zhang, M. Deng, and M. Tang, "Research progress of freeze and thaw cycle destruction of concrete," *Journal of Materials Science and Engineering*, vol. 26, no. 6, pp. 990–994, 2008, in Chinese.

[17] W. Tian and P. Zhang, "Frozen-thaw damage test of concrete pore structure based on CT technology," *Journal of Central South University*, vol. 11, pp. 3069–3075, 2017, in Chinese.

[18] R. Chen and Y. Chen, "Study on mechanical properties after concrete freeze-thaw cycle," *Construction Safety*, vol. 04, pp. 70–73, 2018, in Chinese.

[19] S. Liang, "Study on the compressive strength of the concrete under the freeze-thaw cycle," *Science and Technology & Innovation*, vol. 13, pp. 139-140, 2019, in Chinese.

[20] V. N. Vapnik, *Estimation of Dependence Based on Empirical Data*, Springer-Verlag, Berlin, Germany, 1982.

[21] V. N. Vapnik, "An overview of statistical learning theory," *IEEE Transactions on Neural Networks*, vol. 10, no. 5, pp. 988–999, 1999.

[22] S. S. Keerthi and C. J. Lin, "Asymptotic behaviors of support vector machines with Gaussian kernel," *Neural Computation*, vol. 15, no. 7, pp. 1667–1689, 2003.

[23] National Standard of the People's Republic of China, *GB/T50082-2009 Standard For Test Methods of Long-Term Performance and Durability of Ordinary concrete*, China Architecture and Building Press, Beijing, China, 2009, in Chinese.

[24] X. Liu, *Research on SVM-Based Structural Damage Identification Method"*, Harbin Institute of Technology, Harbin, China, 2008, in Chinese.

[25] V. Cherkassky and Y. Ma, "Practical selection of SVM parameters and noise estimation for SVM regression," *Neural Networks*, vol. 17, no. 1, pp. 113–126, 2004.

Research Article

Dynamic Property Analysis of Orthotropic Bridge Deck with Local Fatigue Crack

Zhao Li ⓘ,[1,2] **Jiarui Zhang** ⓘ,[1,2] **Yaoyang Zhu** ⓘ,[1,2] **and Jianwei Tu** ⓘ[1,2]

[1]*State Key Laboratory of Silicate Materials for Architecture, Wuhan University of Technology, Wuhan 430070, China*
[2]*Hubei Key Laboratory of Roadway Bridge and Structure Engineering, Wuhan University of Technology, Wuhan 430070, China*

Correspondence should be addressed to Jiarui Zhang; zjr1207916099@whut.edu.cn and Jianwei Tu; tujianwei@whut.edu.cn

With the increase in traffic volume and overweight vehicles, fatigue problems are highlighted. Especially for the orthotropic steel deck, the premature cracks seriously affect the service performance, operation, and service quality of the bridge. In this paper, the steel box-girder segment model and deck substructure model considering several typical fatigue cracks were established to reveal the variation law of fatigue cracks on vibration frequency and deflection under vehicle traveling load. A natural frequency analysis was performed to evaluate the change in the vibration characteristics due to localized damage, together with a dynamic analysis that considered a vehicle traveling on the bridge. The results show that the initiation and propagation of several typical cracks have little influence on the lower modes of the overall structure and great influence on the high-order modes of the substructure. The dynamic deflection response of the bridge changed under vehicle load as damage progressed. Therefore, it was possible to identify cracks of the orthotropic steel bridge deck and to provide guidance for fatigue crack detection and repair.

1. Introduction

Orthotropic steel decks (OSDs) have been widely used in bridges with various structural forms and spans due to the advantages of lightweight, favorable mechanical behavior, and convenient construction [1–4], as well as for deck replacement in existing bridges [5, 6]. However, the welding defects and residual stress are easily introduced into the manufacture and construction because of the complex geometric structure forms and structural discontinuity, which may be quite susceptible to traffic-induced fatigue damage [7–10]. An increasing number of investigations indicate that the failures of most steel bridges are caused by fatigue damage [11, 12]. In addition, the crack of the Bronx-Whitestone bridge [13] after 2 years in service and the collapse of the I-35 W bridge over the Mississippi River [14] have aroused attention to the fatigue and fracture of the existing bridge. The emergence of fatigue cracks seriously affects the operation and durability and even endangers the safety of bridges.

The fatigue damage of OSD is still a prominent problem because the cyclic vehicle load directly acts on the deck, especially accidental overloaded trucks [15–17]. Another adverse effect concerning the fatigue behavior of OSD is that the local stress near the crack caused by residual stress and live load stress ranges is concentrated to a high level, which is generally considered to be the main cause of the fatigue and fracture under cyclic vehicle load [18–20]. The typical fatigue cracks of OSD generally observed are illustrated in Figure 1 [21–23]: (1) the longitudinal rib-to-diaphragm welded joint and the cutout of the diaphragm plate; (2) the longitudinal rib-to-deck welded joint; (3) the longitudinal ribs splice joint; (4) the deck-to-vertical stiffener welded joint. During the past decades of engineering practice, many improvements have been achieved, such as structural design and manufacture, crack monitoring, and maintenance. Obviously, the fatigue cracks at the deck-to-vertical stiffener welded joint have been gradually replaced due to the change of the welded joint. Nevertheless, since the first fatigue crack of OSD was reported, the fatigue problem has restricted the development of this type of bridge.
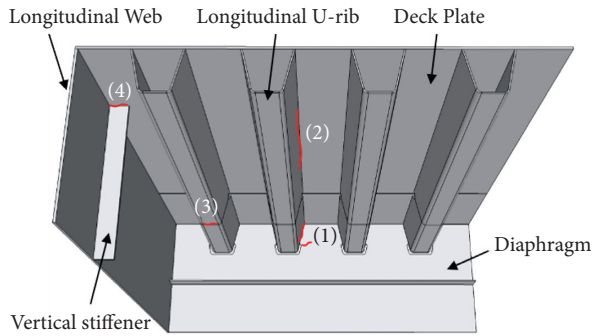
FIGURE 1: Sketch of typical fatigue cracks of OSD.

Many research studies on fatigue resistance have been devoted to the typical fatigue crack of OSDs in test and analysis. From the achieved research, the longitudinal rib-to-deck welded joint is the most common connection and the most sensitive position for fatigue in OSDs, due to direct wheel loading. A considerable amount of research has a focus on this topic [24–26]. Zhang et al. [27] established a local finite element model of OSDs to study the stress distribution of the deck in the longitudinal rib-to-deck welded joint and estimate the fatigue life using the principle of linear elastic fracture mechanics. The results indicate that the high-stress range under the local overloaded wheel is the main reason for the cracks in the longitudinal rib-to-deck welded joint. The principle of linear elastic fracture mechanics can be used to estimate the residual life of the longitudinal rib-to-deck welded joint. Kainuma et al. [28, 29] carried out the fatigue tests and FE analysis to study the structural response, local stress, and the mechanism of crack initiation and propagation near the longitudinal rib-to-deck welded joint. The results show that both the tensile stress and the stress range have an effect on crack initiation, but tensile stress is the important factor for crack propagation. In addition, the root gap shape and the penetration rate have an impact on fatigue durability. Sim et al. [30] investigated the effects of weld melt-through and distortion control measures on the fatigue behavior of the longitudinal rib-to-deck welded joint through six full-scale OSD fatigue tests. The results show that the effective precambering was beneficial to the fatigue resistance of the longitudinal rib-to-deck welded joint. Most cracks are initiated from the weld toe outside the rib. In the orthotropic steel deck, the longitudinal rib-to-diaphragm welded joint is another place prone to fatigue cracks [31]. The investigations of this weld detail indicated that the fatigue crack is mainly caused by the local stress at the weld root or toe generated by in-plane and out-of-plane bending moments [32]. In addition, the stress gradients were so notable that it was not feasible to evaluate fatigue resistance for this weld joint using the simple nominal stress approach. The proposal of notch stress and hot spot stress effectively solves the problem that it is very difficult to evaluate the fatigue assessment of the longitudinal rib-to-diaphragm welded joint [33–37]. The longitudinal rib is the main stress component of the orthotropic steel deck, which plays an extremely important role in increasing the stability and stiffness of the bridge. However, longitudinal rib splice

joints generally adopt overhead welding with incomplete penetration and undercut. The crack is most likely to initiate at the stress concentration point and even propagate to a larger size [38, 39]. A related study on the fatigue resistance of the longitudinal rib splice joints indicated that the fatigue cracks are mainly observed at the transverse weld of longitudinal rib bottom plate because of incomplete penetration.

The above research results of typical fatigue cracks with different details effectively improve the fatigue resistance and deepen the understanding of the fatigue damage mechanism of OSD. However, with the increasing traffic volume and accidental overload, fatigue cracks still seriously affect the durability of bridges. In order to explore the influence of several typical fatigue cracks on the mechanical properties of OSD, the steel box-girder segment model and deck substructure model are established. And, a natural frequency analysis was performed to evaluate the change in the vibration characteristics due to localized damage, together with a dynamic analysis that considered a vehicle traveling on the bridge. According to the research results of this paper, it is possible to predict the location of several typical fatigue cracks in the orthotropic steel deck and to provide a reference for crack maintenance.

2. Analysis Method

2.1. Main Analysis Contents. The natural frequency analysis and dynamic analysis were carried out using the finite element analysis software [40] Ansys15.0 with a steel box-girder segment model and a substructure model. The following were studied:

(1) Global vibration modes analysis for the steel box-girder segment model including crack damage at low frequency

(2) Local vibration modes analysis for the steel substructure model including crack damage at high frequency

(3) Dynamic analysis considering a vehicle traveling on the bridge

2.2. Finite Element Model. The steel box-girder model was based on the in-service cable-stayed bridge including 4 fast lanes and 2 slow lanes. The cable-stayed bridge has a total length of 684 m and a main span of 336 m. The steel deck support is composed of 4 concrete auxiliary piers, 2 concrete towers 106 m higher than the bridge deck, and 104 cables with different pretension. Relevant research shows that there is a high probability of cracks in the red U-rib area. More than 50% of fatigue cracks were located in the third lane, which is mainly used for low-speed truck driving, and few cracks were detected in the first lane [41]. The half cross-sectional view of the steel box girder of the bridge is shown in Figure 2. The 24 m segment model has 3 vertical suspenders on each side with a spacing of 12 m. The steel box girder has a width of 32.8 m and a depth of 3.2 m. The bridge is designed with a 16 mm orthotropic deck, 12 mm bottom plate, 8 mm
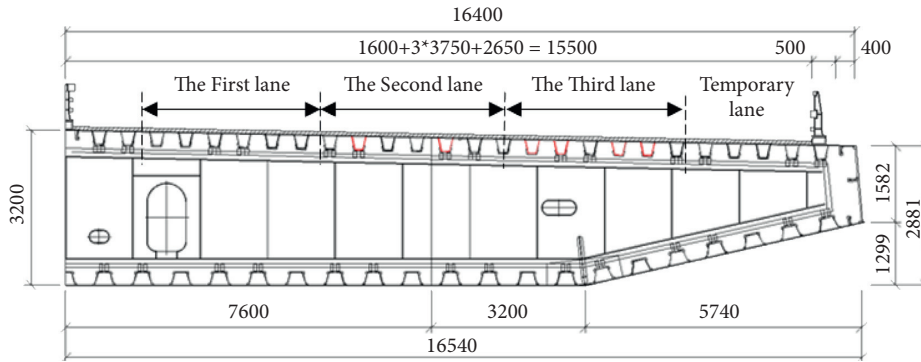
FIGURE 2: The half cross-sectional view of the steel box girder.

longitudinal U-ribs at the top, and 6 mm longitudinal U-ribs at the bottom. The longitudinal U-ribs are 280 mm high and placed at 600 mm centers. The width of the longitudinal U-ribs at the top and bottom are 300 and 400 mm, respectively. The orthotropic deck is supported on 10 mm transverse diaphragms every 3 m. In order to avoid stress concentration, the diaphragm under the longitudinal U-ribs is designed as an arc-shaped notch, and the details of the notch are shown in Figure 3.

The steel box-girder segment model and the substructure model of the orthotropic steel deck were established to accurately simulate the mechanical properties of a steel bridge. All plate members of the bridge are simulated by the 4-node shell63 element. The elastic modulus, Poisson ratio, and density of the selected steel were 206 GPa, 0.3, and 7850 kg/m^3, respectively. The contact of the connecting part of the members is to couple all the degrees of freedom of the node. Considering the vertical constraint of the suspender on the steel box girder, the suspender is simulated by the combine14 element. This element only considers the vertical constraints to simulate the tension provided by the cable to the bridge deck. According to the parameters such as the area, length, and elastic modulus of the cable, the stiffness required to simulate the cable by the combine14 element is 1.089e7 N/m. The following boundary conditions are applied to the model: constrain all degrees of freedom of the upper node of the suspender spring element; constrain the translation of S in longitudinal and transverse directions and the translation of N in longitudinal direction. For the substructure model of OSD, the area with a length of 6 m and width of 2.1 m (4 U-ribs) in the middle of the third lane span is selected, because of the highest probability of crack in the third lane. The segment model and substructure model of OSD are shown in Figure 4.

2.3. Local Damage Model. The stress due to fatigue of the orthotropic steel bridge deck is caused by the cyclic vehicle load directly acting on the deck. The local stress near the crack caused by residual stress and live load stress ranges is concentrated to a high level. The damage models of three typical fatigue cracks of OSD are shown in Figure 5. And, different damage types are described as follows.
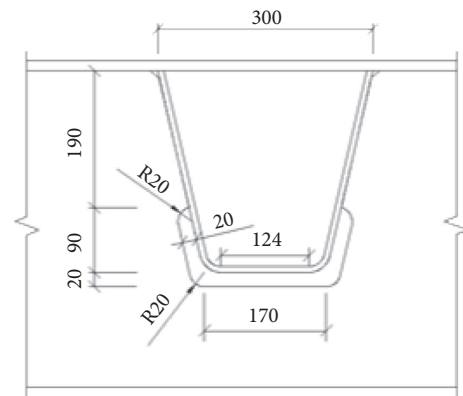

FIGURE 3: The arc-shaped notch.

The first damage type is a crack at the longitudinal rib-to-diaphragm welded joint.

The weld joint between longitudinal U-rib and diaphragm is one of the most complex geometric details in OSD. Under the local wheel load, the flexural deformation of longitudinal U-rib causes repeated out-of-plane deformation of the diaphragm. With the increase in deformation, the stress range will increase because of the welded defects and residual stress. In addition, the fatigue crack may be found on the rib wall or diaphragm at the longitudinal rib-to-diaphragm welded joint by the difference of stiffness between the longitudinal rib and the diaphragm and may expand along the weld to the deck and diaphragm. This connection is one of the most weld details prone to fatigue. In the substructure model, the crack was modeled at the connection between longitudinal rib and diaphragm:

Case 1: the crack appears at the connection between longitudinal U-rib 3R and diaphragm 2# and propagates about 200 mm along the weld.

Case 2: one-side weld between longitudinal U-rib and diaphragm is broken. And, the crack propagates forward and backward for 250 mm along the weld between the U-rib and the deck.

Case 3: one-side weld between longitudinal U-rib and diaphragm is broken, and the crack propagates 300 mm along the weld between the diaphragm and the deck.
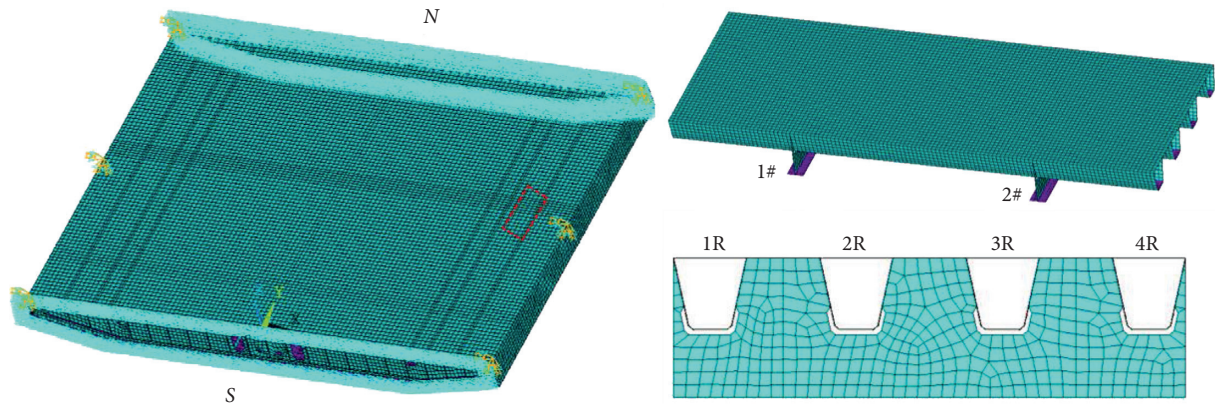
FIGURE 4: The steel box-girder segment model and the substructure model of OSD.
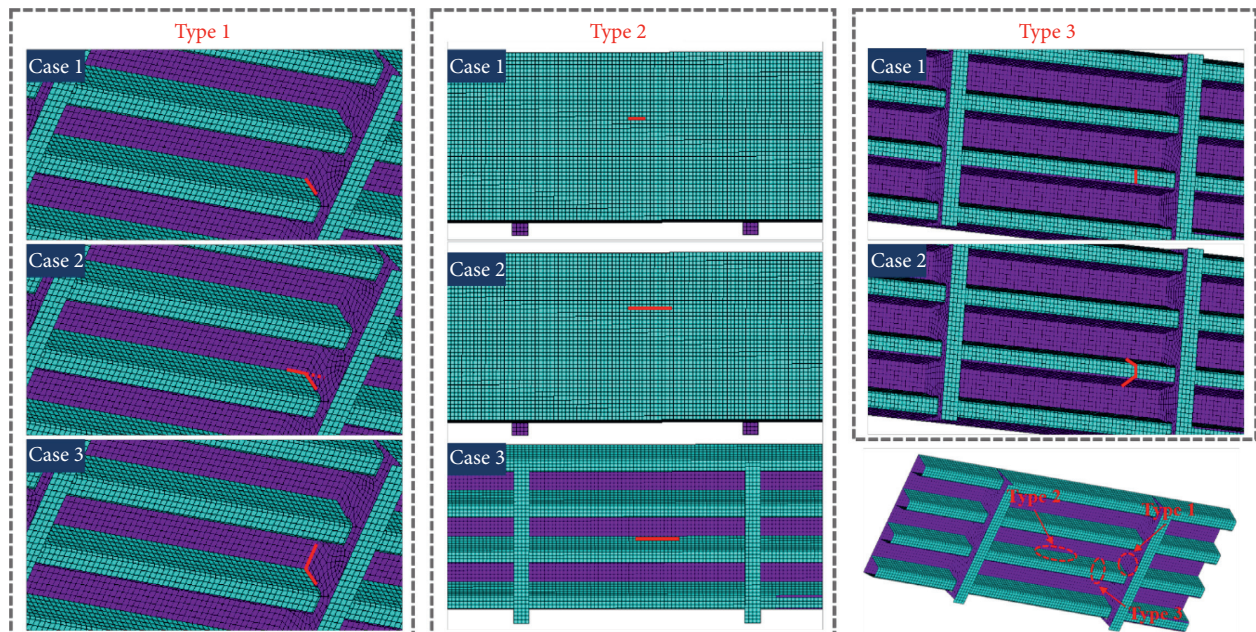

FIGURE 5: Typical crack distribution diagram.

The second damage type is a crack at the longitudinal rib-to-deck welded joint.

The longitudinal rib-to-deck welded joint is one of the most serious positions for fatigue in OSDs with direct local wheel loading. In addition, due to the difference of stiffness between the longitudinal rib and the deck, the stress ranges will be concentrated to a high level at the weld detail, which intensifies the initiation and propagation of fatigue cracks. Unfortunately, this type of fatigue crack monitoring is very difficult. Cracks can only be observed when they penetrate the deck and propagate along the weld, resulting in obvious damage to the bridge deck pavement. Moreover, the maintenance of fatigue cracks needs to interrupt the traffic. In the substructure model, the crack was modeled at the weld of the deck and the longitudinal U-rib 3R, which is located between the diaphragms:

Case 1: the crack appears on the weld root or weld toe of the deck at the longitudinal rib-to-deck welded joint and propagates about 200 mm along the weld

Case 2: the crack continues to propagate, resulting in a crack with a length of 850 mm at the deck between the two diaphragms

Case 3: the crack appears on the weld toe of the longitudinal rib at the longitudinal rib-to-deck welded joint and propagates into a crack with a length of 850 mm along the weld between the two diaphragms

The third damage type is a crack at the longitudinal rib splice joint.

The steel box girder is usually installed by single side overhead welding on-site. This welding process can only be carried out from the outside of the rib with incomplete penetration, resulting in cracks that are easy to initiate on the

weld root at the bottom of the longitudinal rib welded joint. Moreover, the welding of the longitudinal ribs splice joint accounts for about 40% of the total on-site welding of OSD, indicating that fatigue resistance of this weld has a very important influence on the safety of the bridge. In order to reduce the stress of the longitudinal U-rib splice joint, the splicing position is generally located at 1/4 of the space between the two diaphragms. Therefore, in the substructure model, the crack was modeled at 1/4 of the longitudinal U-rib 3R between the diaphragm:

Case 1: the crack appeared at the bottom of the weld at 1/4 of the longitudinal U-rib, with a length of 124 mm

Case 2: the crack continues to propagate, resulting in the complete failure of the butt weld of longitudinal U-rib 3R under the deck

3. Natural Vibration Frequency Analysis

The typical cracks described above were modeled at the corresponding positions of the orthotropic steel deck. For the global segment model and deck substructure model, a comparison of natural vibration frequencies and mode shapes has been studied with damaged and undamaged structures.

3.1. Global Vibration of the Steel Box-Girder Segment Model.
Figure 6 shows the first 5 global natural vibration modes of the steel box-girder segment model with undamaged structure, and Table 1 describes the effects of different damage scenarios on global natural vibration frequency.

From the global vibration mode shapes of the steel box-girder segment model, it can be seen that the first 5 vibration modes include the vertical translational mode (the first vibration shape), bending mode (the second, fourth, and fifth vibration shapes), and torsional mode (the third vibration shape). Due to the different vibration mode shapes, the influence of different damage types on the natural vibration frequency of the global model is slightly different.

For the first vertical translational mode, the vertical vibration is only constrained by the vertical suspender. The vertical vibration is mainly related to the stiffness of the vertical suspender and the self-weight of the segment model, which are less affected by the different damages. According to the calculation results, the first natural frequency of the global model with damages is only 0.00099% lower than that of the healthy model. For the third torsional mode, the torsional vibration at the location of the damages is not dominant, so the influence of various types of damage on the torsional vibration frequency also is not obvious. The third natural frequency of the global model with damages is only 0.00165% lower than that of the complete model. For bending vibration mode, it can be clearly observed that the higher the bending vibration mode order, the greater the influence of damage on natural frequency. However, types and locations of the crack will affect the natural frequency of the structure. Since the crack locations are close to the amplitude of the fourth bending mode, most of the above damaged models have a greater decrease in amplitude in the

fourth bending frequency than that in the second and fifth bending mode. Compared with the healthy model, the bending vibration frequency of the damaged model is reduced by 0.00249% (the second vibration mode shape), 0.01430% (the fourth vibration mode shape), and 0.01278% (the fifth vibration mode shape), respectively.

To summarize the above results for the different damages of the steel box girder, the cracks propagated on the deck have little effect on the vibration mode shapes and natural frequency of the global steel box girder. However, we also found that for similar types of vibration mode shapes, the higher the natural vibration frequency, the greater the impact of the damage. Therefore, we can guess whether the crack propagation will have a great impact on the local higher vibration mode and natural frequency of the steel box girder.

3.2. Local Vibration Model of OSD.
The substructure model selected the area shown in Figure 4 for local vibration modes of OSDs. Modes 1–5 in Figure 7 show the local vibration modes of OSDs. In order to clearly observe the vibration of each part in the substructure model with no damage, a quarter of the grid of the model is treated perspectively. The higher modes mainly involved the local vibration of the deck, longitudinal U-rib, diaphragm, and the combined vibration of components, which should be a focus on the influence of damage on local modes.

Figure 8 shows local vibration modes with Type 1 damage of OSD. The changes of local natural frequency are given in Table 2. For this damage type, when the crack is in the initiation or only confined in the diaphragm (Case 1), the vibration mode shapes of the substructure with damage or no damage is consistent and the frequency changes slightly. The crack may propagate along the deck-longitudinal rib weld (Case 2) or the deck-diaphragm weld (Case 3), which will cause modal shapes of the substructure to change; for example, from Case 2 mode 1 and Case 3 mode 2 in Figure 8, the vibration mode shapes change obviously due to the existence of cracks and the frequency decreases greatly compared with the undamaged structure. In addition, from Case 3 mode 1 in Figure 8, the diaphragm near the damage has obvious out-of-plane deformation, which produces a new vibration mode shape. The reason may be that the damage weakens the restraint effect of the deck and U-rib on the diaphragm, which makes the vibration in the quiet area of the original mode shapes intense.

Figure 9 shows local vibration modes with Type 2 damage of OSD. The changes of local natural frequency are given in Table 3. For this damage type, the cracks may initiate at the weld root and rib-side weld toe of the longitudinal rib-to-deck weld in the span between two diaphragms. The above cracks with little propagation (Case 1) have no obvious impact on the local vibration mode shapes and natural frequencies. After that, the vibration mode shapes and natural frequencies will change greatly. For the crack propagation at the weld root (Case 2), the constrained boundary condition of the deck forms a free boundary near the damage, resulting in the amplitude of substructure
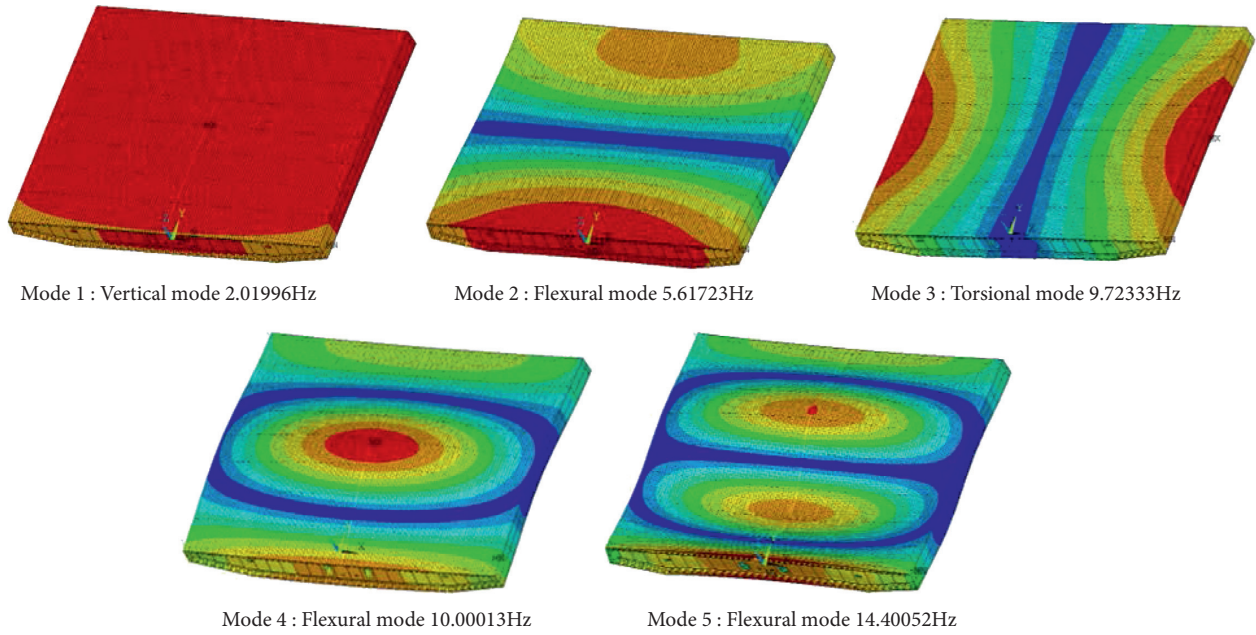
Mode 1 : Vertical mode 2.01996Hz

Mode 2 : Flexural mode 5.61723Hz

Mode 3 : Torsional mode 9.72333Hz

Mode 4 : Flexural mode 10.00013Hz

Mode 5 : Flexural mode 14.40052Hz

FIGURE 6: Global natural vibration mode shapes.

TABLE 1: Global natural vibration frequency.

Global mode	Frequency (Hz)								
	Healthy	Type 1			Type 2			Type 3	
		Case 1	Case 2	Case 3	Case 1	Case 2	Case 3	Case 1	Case 2
Mode 1	2.01996	2.01996	2.01995	2.01996	2.01996	2.01994	2.01996	2.01996	2.01996
Mode 2	5.61723	5.61723	5.61721	5.61723	5.61722	5.61717	5.61722	5.61723	5.61709
Mode 3	9.72333	9.72333	9.72317	9.72328	9.72332	9.72308	9.72333	9.72333	9.72330
Mode 4	10.00013	10.00012	9.99951	9.99998	10.00008	9.99870	10.00012	10.00011	9.99927
Mode 5	14.40052	14.40052	14.40014	14.40049	14.40049	14.39960	14.40052	14.40049	14.39868

Mode 1 : 126.2175Hz

Mode 2 : 142.82004Hz

Mode 3 : 148.12576Hz

Mode 4 : 159.98489Hz

Mode 5 : 162.14186Hz
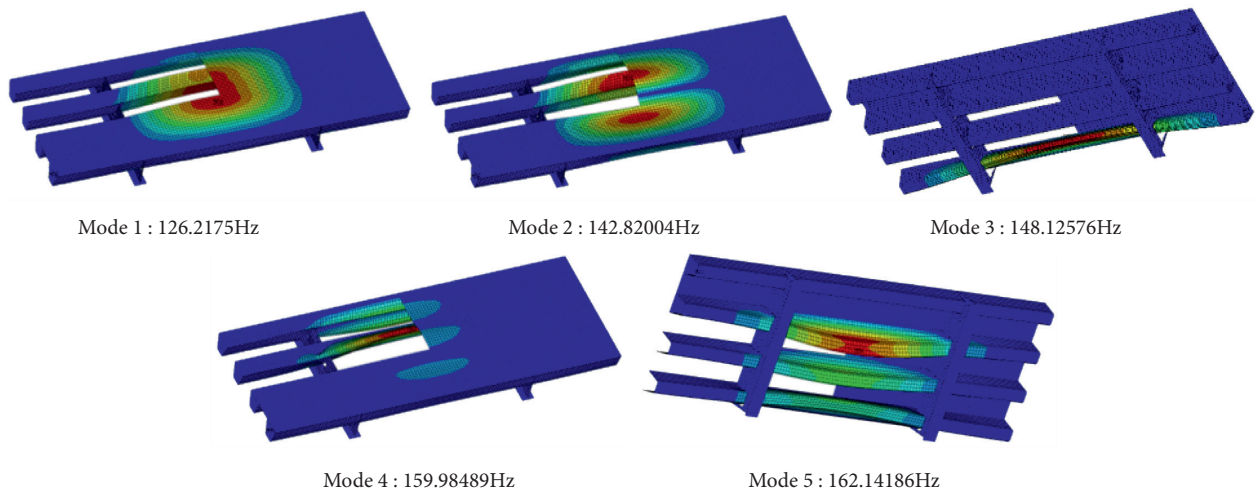
FIGURE 7: Local vibration mode shapes.

vibration shapes appearing at the damage, such as Case 2 mode 1 and mode 4 in Figure 9. The crack propagation at the rib-side weld toe (Case 3) weakens the constraint of the deck on the U-rib. The vibration mode shapes of the U-rib become a horizontal out-of-plane vibration. It is a new vibration mode shape, which greatly reduces the local natural frequency. It can be found that the crack of this damage type will greatly reduce the stiffness of the deck,

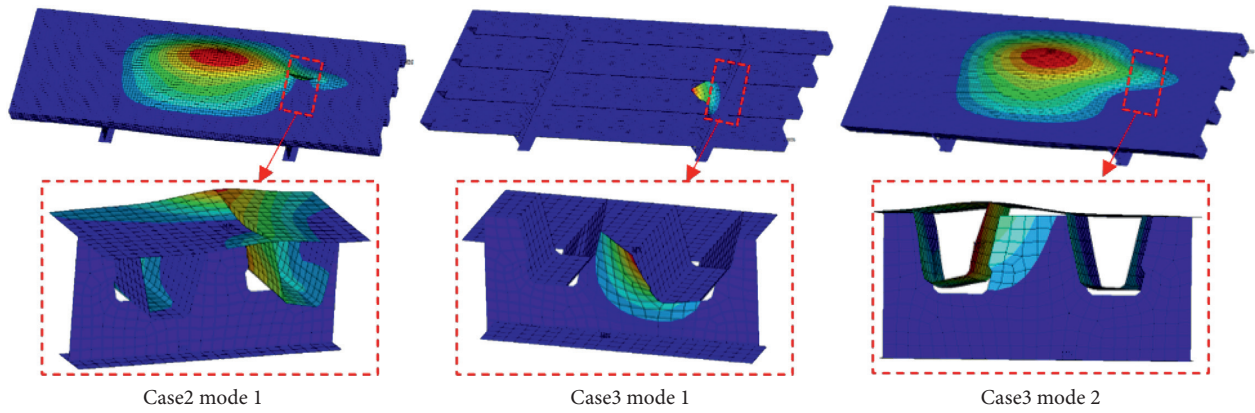FIGURE 8: Local vibration mode shapes with Type 1 damage.

TABLE 2: Frequency of local vibration mode (Type 1 damage).

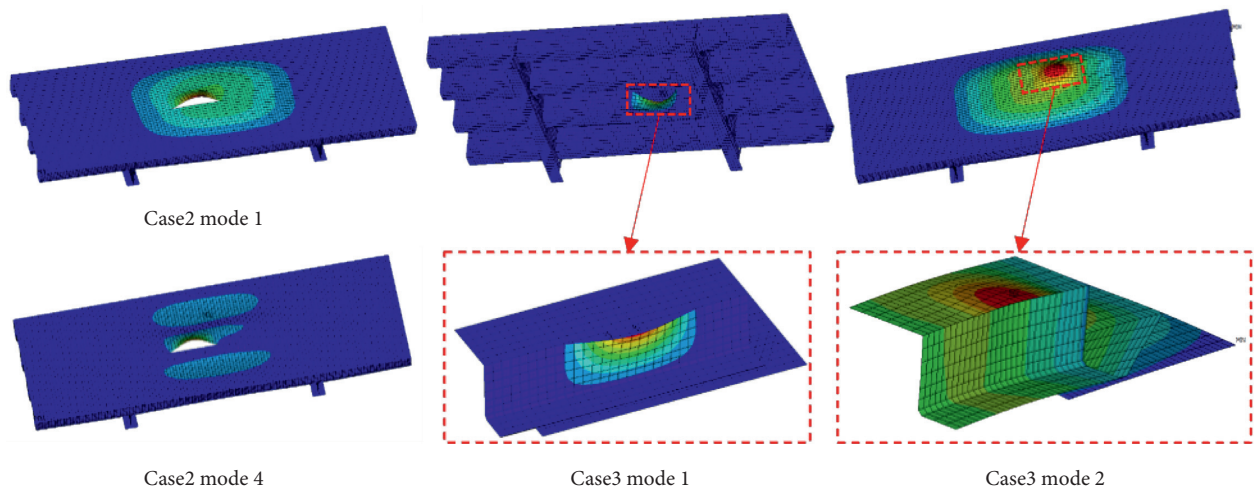| Local mode	Frequency (Hz)						
	Heathy	Case 1	Error (%)	Case 2	Error (%)	Case 3	Error (%)
1	126.21751	125.45765	−0.602	118.20422	−6.349	109.56704	−13.192
2	142.82004	142.54165	−0.195	140.18200	−1.847	117.87555	−17.466
3	148.12576	148.12061	−0.003	148.10308	−0.015	140.18688	−5.360
4	159.98489	158.16308	−1.139	158.07246	−1.195	148.10629	−7.425
5	162.14186	160.91106	−0.759	160.86859	−0.785	158.13833	−2.469

FIGURE 9: Local vibration mode shapes with Type 2 damage.

TABLE 3: Frequency of local vibration mode (Type 2 damage).

Local mode	Frequency (Hz)						
	Heathy	Case 1	Error (%)	Case 2	Error (%)	Case 3	Error (%)
1	126.21751	126.20012	−0.014	124.09384	−1.683	94.26651	−25.314
2	142.82004	142.72666	−0.065	141.71643	−0.773	123.3421	−13.638
3	148.12576	148.12542	−0.000	148.11960	−0.004	141.74663	−4.307
4	159.98489	159.98089	−0.0025	159.07485	−0.569	148.12468	−7.413
5	162.14186	162.11066	−0.019	161.87736	−0.163	159.93448	−1.361

Case2 mode 1   Case2 mode 4
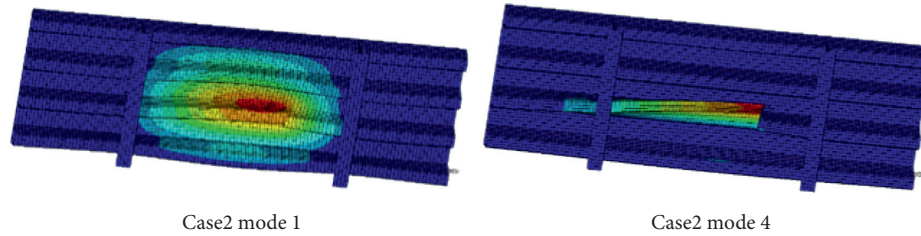
FIGURE 10: Local vibration mode shapes with Type 3 damage.

causing great harm to the bridge deck pavement, and even endanger traffic safety.

Figure 10 shows local vibration modes with Type 3 damage of OSD. The changes of local natural frequency are given in Table 4. For this damage type, crack initiation and propagation at the bottom of U-rib (Case 1) have no obvious impact on the local vibration mode and the frequency is almost unchanged. Then, the crack will propagate along the butt weld of the U-rib. The stiffness of longitudinal U-rib near the damage decreases greatly, resulting in the transfer of the vertical vibration mode in the middle of the span to the weld of 1/4 of the U-rib, such as Case 2 mode 1 in Figure 10. In addition, the existence of cracks weakens the constraints between U-ribs and also causes the horizontal distortion of U-ribs. Although this damage mode did not cause new vibration modes, it greatly weakens the stiffness of the longitudinal rib and reduces the natural frequency.

To summarize, for the local higher vibration modes of the substructure model, the initiation of fatigue cracks has no obvious effect on the vibration mode shapes and the natural frequencies. With the crack propagation, the local vibration modes and frequencies of the orthotropic steel bridge deck change greatly and even new vibration modes appear. Therefore, if it is possible to identify the local vibration mode of the structure, the fatigue crack type of the bridge deck can be predicted.

4. Dynamic Response of the Traveling Vehicle

4.1. Traveling Vehicle Load.
According to Chinese Code JTJ 021–89 [42], the vehicle traveling load is as shown in Figure 11. The vehicle was a five-axle vehicle with a total weight of 550 kN. The spacing and weight distribution of each axle are shown in Figure 11, respectively. Because the orthotropic steel deck is very sensitive to local load, the obvious local effect can be found only when the wheel load is close to the relevant details [43]. The spacing of the diaphragms (3 m) is significantly less than the spacing between the front and middle axles (3.7 m), and the axle weight of the front axle is small, far less than the middle and rear axles. Therefore, only the double axles of the rear axle (including two axles, the spacing is 1.4 m) were selected for vehicle load. Considering the influence of road roughness and other factors, an impact coefficient of 15% was added.

The loading procedure simulates the traveling of the vehicle on the deck. The calculation results of the wheel at 16 m in the middle of the bridge deck were selected to weaken the influence of boundary conditions. The moving

TABLE 4: Frequency of local vibration mode (Type 3 damage).

Local mode	Frequency (Hz)				
	Heathy	Case 1	Error (%)	Case 2	Error (%)
1	126.21751	126.07544	−0.113	119.06372	−5.668
2	142.82004	142.70092	−0.083	138.47059	−3.045
3	148.12576	148.12547	−0.000	147.37262	−0.508
4	159.98489	159.96930	−0.010	148.14346	−7.402
5	162.14186	162.10340	−0.024	160.46715	−1.033

Driving direction
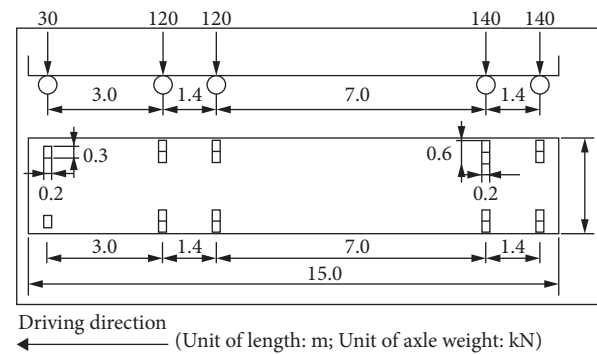(Unit of length: m; Unit of axle weight: kN)

FIGURE 11: The vehicle traveling load.

route of the vehicle is shown in Figure 12. The vehicle load moved along the longitudinal direction of the bridge deck, with a uniform step of 0.2 m.

4.2. Change of the Dynamic Displacement Response.
The variation of measured displacement is widely used to evaluate the loss of stiffness caused by damages to the bridge. Because different damage types have different contributions to the displacement response, we focused on the displacement of three parts: the welded joint between the longitudinal U-rib and the diaphragm, the midpoint of the longitudinal rib-to-deck welded joint between two diaphragms, and 1/4 of the longitudinal ribs splice joint, as shown in Figure 13.

Figure 14 shows the displacement with Type 1 damage change of three observation points under the traveling vehicle load (Z represents the distance between the center of double axle and the starting point). For Case 1, when the crack only existed at the connection between the diaphragm and the U-rib, the displacement of the three observation points was basically unchanged. However, when the crack
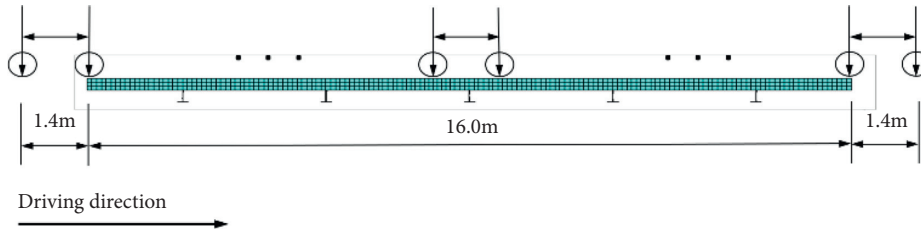
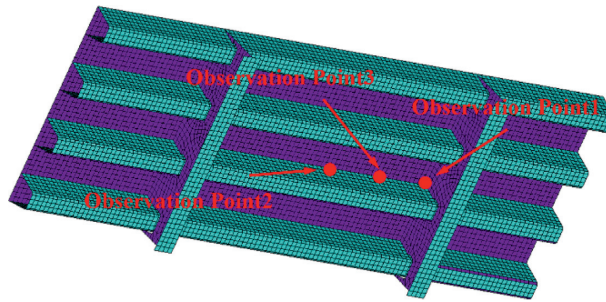FIGURE 12: Distribution of the local wheel load.

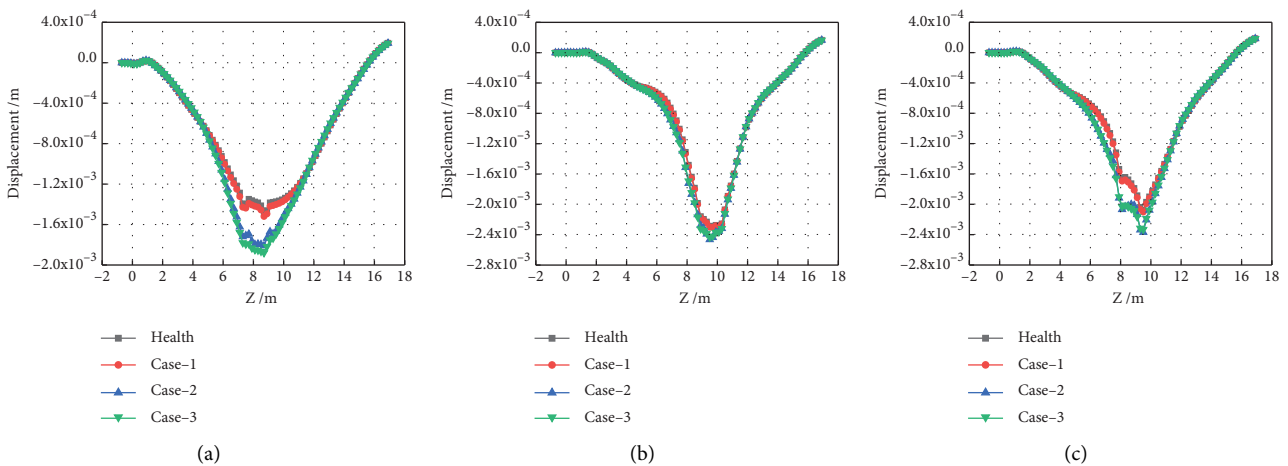
FIGURE 13: Location of the observation point.

FIGURE 14: Displacement of observation point (Type 1 damage). (a) Observation point 1. (b) Observation point 2. (c) Observation point 3.

continued to propagate (such as Case 2 and Case 3), the displacement increased greatly. The displacement change recorded in Case 3 at observation point 1 was the largest, with an increase of 0.398 mm. The reason for this phenomenon may be that the crack of damage Type 1 reduced the constraint of the diaphragm and U-rib on the deck, resulting in a significant reduction in the stiffness near observation point 1. When the local wheel load travels above the deck, the corresponding displacement will also increase. Therefore, it is possible to identify crack damage Type 1 according to the displacement change recorded at observation point 1.

Figure 15 shows the displacement with Type 2 damage change of three observation points under the traveling vehicle load. For Case 1 and Case 2, with the crack propagation on the deck-side toe, the displacements of observation point 2 and observation point 3 changed slightly and the

displacement of observation point 1 is basically unchanged. For Case 3, the crack propagation on the rib-side toe had obvious changes in the displacement recorded at observation point 2 with an increase of 0.370 mm. The reason for this phenomenon was that the crack invalidated the weld at the longitudinal rib-to-deck and the stiffness decreases greatly near observation point 2. When the local wheel load traveled above observation point 2, the displacement increased sharply. Therefore, it is possible to identify crack damage Type 2 according to the displacement changes recorded at observation point 2.

Figure 16 shows the displacement with Type 3 damage change of three observation points under the traveling vehicle load. For Case 1, the crack at the U-rib butt weld hardly affected the displacement of the three observation points. However, once the crack propagated along the butt weld (Case 2), the displacement will increase greatly. The
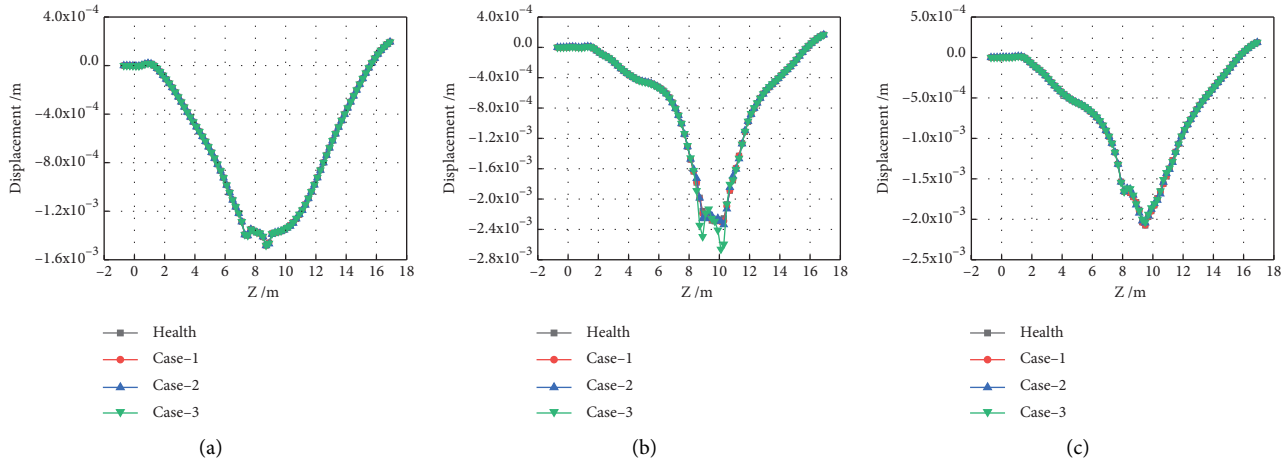
FIGURE 15: Displacement of observation point (Type 2 damage). (a) Observation point 1. (b) Observation point 2. (c) Observation point 3.
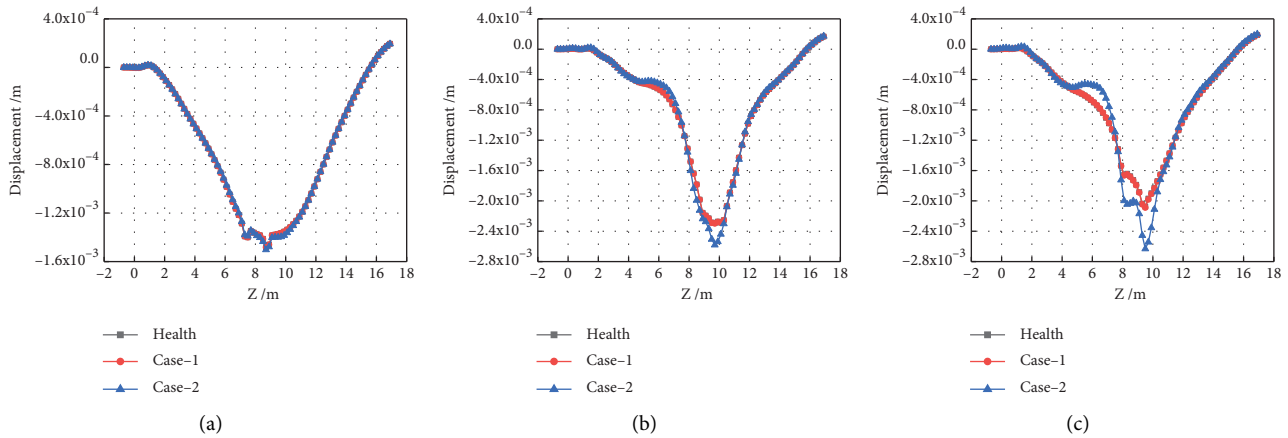

FIGURE 16: Displacement of the observation point (Type 3 damage). (a) Observation point 1. (b) Observation point 2. (c) Observation point 3.

displacement change recorded at observation point 3 was the largest, with an increase of 0.555 mm. The reason for this phenomenon was the sudden change of the stiffness at the weld due to the failure of the U-rib butt weld. When the center of the double axle just reached the weld failure position, the displacement increased obviously. Therefore, it is possible to identify crack damage Type 3 according to the displacement changes recorded at observation point 3.

5. Conclusion

In order to reveal the variation law of fatigue cracks on vibration frequency and deflection under vehicle load, global and local models of orthotropic steel decks with different types of damages caused by several cracks were established. The following conclusions could be obtained:

(1) Different damages slightly affect the vibration mode shapes and natural frequencies of the global steel box girder. For similar vibration mode shapes, the higher the frequency, the greater the impact of the damage.

(2) The cracks initiated on the local substructural mode of OSD have no obvious effect on the vibration mode shapes and natural frequencies. However, the damages caused by the propagated cracks will aggravate the vibration of the local model and even produce new vibration mode shapes.

(3) The different damages have different contributions to the dynamic displacement response of the bridge under vehicle load. Damage Type 1 will aggravate the displacement of the rib-to-diaphragm welded joint. Damage Types 2 and 3 will aggravate the displacement at the middle and 1/4 of the U-rib, respectively. Therefore, if the local mode of the orthotropic steel bridge deck and the displacement of key details under vehicle load can be obtained, it is possible to identify the damage type and predict the crack growth trend. This research can be used to provide

guiding significance for fatigue crack detection and maintenance.

Data Availability

The data used to support the findings of this study are included within the article.

Conflicts of Interest

The authors declare that they have no conflicts of interest.

Acknowledgments

References

[1] D. Li, C. Zhang, and P. Lu, "Fatigue property and improvement of a rounded welding region between the diaphragm plate and closed rib of an orthotropic steel bridge deck," *Metals*, vol. 10, no. 2, p. 161, 2020.

[2] C. Cui, Y.-L. Xu, and Q.-H. Zhang, "Multiscale fatigue damage evolution in orthotropic steel deck of cable-stayed bridges," *Engineering Structures*, vol. 237, no. 3, Article ID 112144, 2021.

[3] Z. Fu, B. Ji, C. Zhang, and D. Li, "Experimental study on the fatigue performance of roof and U-rib welds of orthotropic steel bridge decks," *KSCE Journal of Civil Engineering*, vol. 22, no. 1, pp. 270–278, 2017.

[4] X. Jiang, Y. Yuan, C. Wu, and C. W. Luo, "Fatigue life assessment of orthotropic steel deck with UHPC pavement," *Journal of Engineering*, vol. 2017, Article ID 8413607, 2017.

[5] P. A. Tsakopoulos and J. W. Fisher, "Full-scale fatigue tests of steel orthotropic decks for the williamsburg bridge," *Journal of Bridge Engineering*, vol. 8, no. 5, pp. 323–333, 2003.

[6] S. Mustafa, H. Sekiya, M. Hayama, and C. Miki, "Effects of redecking from RC deck to orthotropic steel deck on seismic resistance of elevated girder bridges," *International Journal of Steel Structures*, vol. 20, no. 4, pp. 1393–1404, 2020.

[7] M. S. Pfeil, R. C. Battista, and A. J. R. Mergulhão, "Stress concentration in steel bridge orthotropic decks," *Journal of Constructional Steel Research*, vol. 61, no. 8, pp. 1172–1184, 2005.

[8] H.-T. Nguyen, Q.-T. Chu, and S.-E. Kim, "Fatigue analysis of a pre-fabricated orthotropic steel deck for light-weight vehicles," *Journal of Constructional Steel Research*, vol. 67, no. 4, pp. 647–655, 2011.

[9] N. Van den Berg, H. Xin, and M. Veljkovic, "Effects of residual stresses on fatigue crack propagation of an orthotropic steel bridge deck," *Materials & Design*, vol. 198, Article ID 109294, 2021.

[10] W. Nagy, E. Van Puymbroeck, K. Schotte, P. Van Bogaert, and H. De Backer, "Measuring residual stresses in orthotropic steel decks using the incremental hole-drilling technique," *Experimental Techniques*, vol. 41, no. 3, pp. 215–226, 2017.

[11] N. Lu, M. Noori, and Y. Liu, "Fatigue reliability assessment of welded steel bridge decks under stochastic truck loads via machine learning," *Journal of Bridge Engineering*, vol. 22, no. 1, Article ID 04016105, 2017.

[12] A. Duchaczek and Z. Mańko, "Influence of fatigue crack on strains state within assembly holes in a web of steel bridge girder," *International Journal of Civil Engineering*, vol. 15, no. 4, pp. 627–640, 2017.

[13] G.-N. Fanjiang, Q. Ye, O. N. Fernandez, and L. R. Taylor, "Fatigue analysis and design of steel orthotropic deck for bronx-whitestone bridge, New York city," *Transportation Research Record: Journal of the Transportation Research Board*, vol. 1892, no. 1, pp. 69–77, 2004.

[14] H. M. Salem and H. M. Helmy, "Numerical investigation of collapse of the Minnesota I-35W bridge," *Engineering Structures*, vol. 59, pp. 635–645, 2014.

[15] N. Ma and R. Wang, "Effects of impact loads on local dynamic behavior of orthotropic steel bridge decks," *International Journal of Steel Structures*, vol. 21, no. 1, pp. 132–141, 2020.

[16] B. Cheng, X. Ye, X. Cao, D. D. Mbako, and Y. Cao, "Experimental study on fatigue failure of rib-to-deck welded connections in orthotropic steel bridge decks," *International Journal of Fatigue*, vol. 103, pp. 157–167, 2017.

[17] Y. Liu, X. H. Xiao, N. W. Lu, and Y. Deng, "Fatigue reliability assessment of orthotropic bridge decks under stochastic truck loading," *Shock and Vibration*, vol. 2016, Article ID 4712593, 2016.

[18] F. Jiang, Z. Fu, B. Ji, and L. Wan, "Fatigue life evaluation of deck to U-rib welds in orthotropic steel deck integrating weldment size effects on welding residual stress," *Engineering Failure Analysis*, vol. 124, Article ID 105359, 2021.

[19] S. Kainuma, Y.-S. Jeong, M. Yang, and S. Inokuchi, "Welding residual stress in roots between deck plate and U-rib in orthotropic steel decks," *Measurement*, vol. 92, pp. 475–482, 2016.

[20] Y. Xiong, C. Li, Z. Chen, J. He, and H. Xin, "The evolution of residual stress in rib-diaphragm joints of orthotropic steel decks subjected to thermal cutting and welding," *Materials*, vol. 13, no. 17, p. 3804, 2020.

[21] S. Chen, Y. Huang, P. Gu, and J.-Y. Wang, "Experimental study on fatigue performance of UHPC-orthotropic steel composite deck," *Thin-Walled Structures*, vol. 142, pp. 1–18, 2019.

[22] R. Walter, J. F. Olesen, H. Stang, and T. Vejrum, "Analysis of an orthotropic deck stiffened with a cement-based overlay," *Journal of Bridge Engineering*, vol. 12, no. 3, pp. 350–363, 2007.

[23] M. Yang, B. Ji, Z. YuanZhou, and Z. Fu, "Fatigue behavior and strength evaluation of vertical stiffener welded joint in orthotropic steel decks," *Engineering Failure Analysis*, vol. 70, pp. 222–236, 2016.

[24] J.-H. Xu, G.-D. Zhou, and T.-Y. Zhu, "Fatigue reliability assessment for orthotropic steel bridge decks considering load sequence effects," *Frontiers in Materials*, vol. 8, Article ID 678855, 2021.

[25] M. Li, Y. Suzuki, K. Hashimoto, and K. Sugiura, "Experimental study on fatigue resistance of rib-to-deck joint in orthotropic steel bridge deck," *Journal of Bridge Engineering*, vol. 23, no. 2, Article ID 04017128, 2018.

[26] Y. Liu, F. Chen, D. Wang, and N. Lu, "Fatigue crack growth behavior of rib-to-deck double-sided welded joints of orthotropic steel decks," *Advances in Structural Engineering*, vol. 24, no. 3, pp. 556–569, 2020.

[27] Y. L. Zhang, Y. S. Li, and D. Y. Zhang, "Fatigue life estimation of rib-to-deck joints in orthotropic steel decks," *Advanced Materials Research*, vol. 163-167, pp. 410–416, 2010.

[28] S. Kainuma, M. Yang, Y.-S. Jeong, S. Inokuchi, A. Kawabata, and D. Uchida, "Experiment on fatigue behavior of rib-to-deck weld root in orthotropic steel decks," *Journal of Constructional Steel Research*, vol. 119, pp. 113–122, 2016.

[29] S. Kainuma, M. Yang, Y.-S. Jeong, S. Inokuchi, A. Kawabata, and D. Uchida, "Fatigue behavior investigation and stress analysis for rib-to-deck welded joints in orthotropic steel decks," *International Journal of Steel Structures*, vol. 18, no. 2, pp. 512–527, 2018.

[30] H.-B. Sim, C.-M. Uang, and C. Sikorsky, "Effects of fabrication procedures on fatigue resistance of welded joints in steel orthotropic decks," *Journal of Bridge Engineering*, vol. 14, no. 5, pp. 366–373, 2009.

[31] Q.-H. Zhang, C. Cui, Y.-Z. Bu, Y.-M. Liu, and H.-W. Ye, "Fatigue tests and fatigue assessment approaches for rib-to-diaphragm in steel orthotropic decks," *Journal of Constructional Steel Research*, vol. 114, pp. 110–118, 2015.

[32] J.-H. Choi and D.-H. Kim, "Stress characteristics and fatigue crack behaviour of the longitudinal rib-to-cross beam joints in an orthotropic steel deck," *Advances in Structural Engineering*, vol. 11, no. 2, pp. 189–198, 2008.

[33] B. Wang, "Fatigue assessment of the diaphragm-to-rib welded connection in orthotropic steel deck using effective notch stress approach," *Journal of Failure Analysis and Prevention*, vol. 15, no. 1, pp. 65–73, 2014.

[34] M Aygül, M Al-Emrani, and S Urushadze, "Modelling and fatigue life assessment of orthotropic bridge deck details using FEM," *International Journal of Fatigue*, vol. 40, pp. 129–142, 2012.

[35] K. Yokozeki and C. Miki, "Fatigue evaluation for longitudinal-to-transverse rib connection of orthotropic steel deck by using structural hot spot stress," *Welding in the World*, vol. 60, no. 1, pp. 83–92, 2015.

[36] Z. Fu, B. Ji, Z. Ye, and Y. Wang, "Fatigue evaluation of cable-stayed bridge steel deck based on predicted traffic flow growth," *KSCE Journal of Civil Engineering*, vol. 21, no. 4, pp. 1400–1409, 2016.

[37] J. Di, X. Z. Ruan, X. H. Zhou, J. Wang, and X. Peng, "Fatigue assessment of orthotropic steel bridge decks based on strain monitoring data," *Engineering Structures*, vol. 228, no. 1, p. 111437, 2020.

[38] M. Yang, S. Kainuma, and Y.-S. Jeong, "Structural behavior of orthotropic steel decks with artificial cracks in longitudinal ribs," *Journal of Constructional Steel Research*, vol. 141, pp. 132–144, 2018.

[39] Z. Xiao, K. Yamada, J. Inoue, and K. Yamaguchi, "Fatigue cracks in longitudinal ribs of steel orthotropic deck," *International Journal of Fatigue*, vol. 28, no. 4, pp. 409–416, 2006.

[40] Y. Nakasone, S. Yoshimoto, and T. A. Stolarski, *Engineering Analysis with ANSYS Software*, Elsevier Butterworth-Heinemann, 1st edition, 2006.

[41] Q. Wang, B. Ji, X. Chen, and Z. Ye, "Dynamic response analysis-based fatigue evaluation of rib-to-deck welds considering welding residual stress," *International Journal of Fatigue*, vol. 129, no. 9, Article ID 105249, 2019.

[42] Z. Y. Bao and Ministry of Communications of the People's Republic of China (Mcprc), *General Code for Design of Highway Bridges and Culverts*, JTJ 021-89, Beijing, 1989.

[43] Z. Zhu, T. Yuan, Z. Xiang, Y. Huang, Y. E. Zhou, and X. Shao, "Behavior and fatigue performance of details in an orthotropic steel bridge with UHPC-deck plate composite system under in-service traffic flows," *Journal of Bridge Engineering*, vol. 23, no. 3, Article ID 04017142, 2018.